Development and Characterisation of New Exfoliated Graphite Substrates for the Study of Adsorbed Helium Films

Kristian Kent

Royal Holloway College
University of London

A thesis submitted to the University of London
for the degree of Doctor of Philosophy

September 2014

Declaration of Authorship

I, Kristian Kent, hereby declare that this thesis and the work presented in it is entirely my own. Where I have consulted the work of others, this is always clearly stated.

Signed: _____

Date: _____

Abstract

This thesis describes the development and characterisation of a new exfoliated graphitic substrate for low temperature studies on thin helium films. The most commonly used graphite substrates for helium film experiments have been the commercially available Papyex, Grafoil and ZYX. These can be characterised by their specific surface areas and surface coherence lengths, the typical step-free size of their basal-plane adsorbing facets. The surface coherence length for Grafoil is 10-20 nm, whilst for ZYX it is of the order of 200 nm. The ultimate goal of this work was to produce a substrate with larger coherence lengths than previous substrates, to enable the observation and study of novel new phases in helium films which exhibit long range order.

The new substrate uses natural Madagascan flake graphite as the starting material. This flake is then intercalated with Potassium and Ammonia and then exfoliated at relatively low temperatures via thermal decomposition. The resulting exfoliated material is then compressed into foils. A comparative study of this new material has been performed, characterising them against existing substrates using a wide range of techniques. The bulk properties have been studied using: X-ray diffraction to compare the mosaic spread and the in-plane crystallite sizes; Glow discharge mass spectrometry to measure the impurity levels; Surface characterisation has been by: Vapour pressure isotherms to measure the specific surface area and surface quality; Various microscopy techniques to image surfaces.

The final stage of this work was to perform a preliminary experiment on a prototype substrate to demonstrate its viability for low temperature SQUID NMR measurements. This involved measuring the NMR properties of ^{3}He as the coverage was swept through monolayer completion to observe the characteristic T_2^* minimum.

This work took place in the context of efforts to reduce the time between the NMR tipping pulse and measurement, which is especially important around the T_2^* minimum.

Acknowledgements

First of all I would like to thank John Saunders for taking me on as his PhD student and giving me the opportunity to work in science. Furthermore, I would like to thank John for his patience during my write up; when he did receive thesis chapters, a response was never more than a few days away.

From the ULT group at RHUL I would like to thank Andrew Casey, Aya Shibahara, Lev Levitin and George Nichols. Special thanks is reserved for the W061 crew; Frank Arnold, Jan Nyeki and Ben Yager. It has been an absolute pleasure to work with everyone.

I very much enjoyed working in the labs at UCL, and that was due entirely to the people that work there. From the CMMP group at UCL I would like to thank Neal Skipper, David Buckley, Patrick Cullen and the constant optimist, Chris Howard. The karaoke nights were especially enjoyable.

I am deeply grateful to Francis Greenough, Massimo Venti, Andy Alway, Michele Piscitelli, Ian Murray and Harpal Sandhu, all of whom keep everything running smoothly, as well as making the department a very enjoyable and friendly place to work.

Further thanks is given to Dan Porter and David Voneshan for their scattering wisdom and for being reliable tea buddies. James Wells for showing me what a sazerac is and the many nights spent listening to crust, DnB and UK hip hop. Erwan Le Ber for his constant supply of cheese, wine and saucisson. Connor Shelly

for nearly getting me murdered in Norway.

Outside of science, I am thankful to have excellent friends who know and care nothing about my work. I am also thankful to have received unwavering love and support from my girlfriend Emma.

Finally, I would like to thank my parents. Everything I have have achieved is due to them.

Contents

List of Figures

List of Tables

Chapter 1

Introduction

Two dimensional physics has been of theoretical interest for many years. As early as 1935 Peierls [1] argued that a two-dimensional solid effectively does not exist above 0 K due to thermal fluctuations. Similarly, the Mermin and Wagner theorem [2] states that within the Heisenberg model of magnetism, ordered magnetic states cannot exist in a one- or -two-dimensional lattice of spins. Work by Berezinkskii [3] and Kosterlitz and Thouless [4] showed however, that ordered states could be preserved in the thermodynamic limit of an infinite 2D lattice ($L \to \infty$) through "topological ordering". Such ideas have proven vital to understanding crystalline, magnetic and superfluid ordering in lower dimensional systems.

Much of the experimental confirmation for these ideas has come from the study thin adsorbed films. For example, one of the earliest confirmations of Kosterlitz-Thouless (KT) theory came from the study by Bishop and Reppy [5] of a thin superfluid film of ^{4}He adsorbed on Mylar. Since then, thin adsorbed films of ^{3}He and ^{4}He have been recognised as an excellent experimental testing ground for many ideas concerning two-dimensional magnetism and superfluidity. Similarly, studies of two-dimensional solids composed of other rare gases have been been used to test theories of two-dimensional melting [6, 7].

These thin films can be adsorbed onto a wide variety of solids, however exfoliated graphite has emerged as one of the pre-eminent substrates for realising two-dimensional states of matter. Being composed of a large number microscopic crystallites with atomically flat adsorption surfaces, this material balances the requirements of sufficient adsorption area whilst still retaining significant two-dimensional character in its surfaces. That being said, the traditional exfoliated graphite substrates of Grafoil, Papyex and ZYX still display signatures of finite size effects in the films that they form, and is thought that the *surface coherence length* of these substrates plays a role in inhibiting the formation of certain exotic two-dimensional phases.

In this context, this thesis discusses the development and characterisation of a new exfoliated graphite substrate for studies of thin helium films in the hope that it will allow novel phases of two-dimensional helium to be observed and provide further insight into the role of surface disorder. The work has been divided into seven chapters including the current chapter.

The second chapter presents a summary of graphitic substrates. After the basic structure of graphite is discussed, the reader is introduced to the concepts of Graphite Intercalation Compounds (GICs) and their subsequent exfoliation. A discussion of the previous substrates Grafoil, Papyex and ZYX and their properties is then presented along with some information about characterisation methods that are described in the literature.

The third chapter describes all aspects of the substrate manufacturing procedure. This includes a discussion of the highly crystalline kish graphite as a potential source material, which was eventually discarded in favour of Madagascan flake graphite. The intercalation and exfoliation procedures are then described in detail.

The fourth chapter gives an account of the various techniques that were applied in an attempt to characterise the new material, and how the knowledge gained was used to modify the procedures described in chapter 4 to create an exfoliation

procedure for the final substrate.

The fifth chapter details a Nuclear Magnetic Resonance (NMR) experiment that was performed on an early prototype substrate to test its viability for further work at micro-kelvin temperatures. Specifically, we attempted to reproduce earlier results of Owers-Bradley [8] in which a minimum in T_2^* is seen at monolayer completion of ^{3}He on Grafoil.

The final chapter gives a brief summary of the results and a discussion of the potential avenues for future work.

The present chapter will continue with a description of physical adsorption, followed by a brief literature review of important results in adsorption studies, with particular emphasis on the adsorption of helium and other rare gases onto graphite.

1.1 Physical Adsorption: A Qualitative Overview

The phenomenon of physical adsorption, as is shown in figure 1.1, is the tendency for atoms and molecules of gas to adhere to the surfaces of solids as a result of the van der Waals forces between the gas molecules and the solid surface. When a gas becomes bound, or adsorbed, to a surface it is referred to as the *adsorbate* and is treated as distinct phase of matter existing in equilibrium with a vapour phase above it. It is also common to refer to the adsorbed phase as an adsorbed *film*. *Substrate* and *adsorbent* are standard terms for the adsorbing surface.

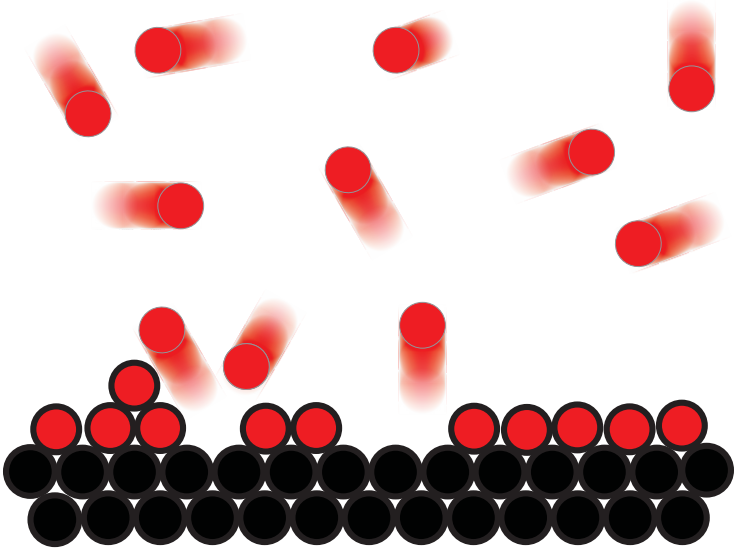

Figure 1.1: Simple diagram outlining the phenomenon of adsorption; the red circles with motion blur represent gaseous atoms/molecules, whilst the black circles represent the substrate. The red circles with black outline represent the adsorbate bound to the substrate. Other aspects shown by this picture are multilayer adsorption, incomplete coverage represented by gaps in the adsorbate.

The weak nature of Van der Waals forces means that adsorption is entirely reversible; lowering the temperature is favourable to film growth, whilst increasing the temperature means that molecules will leave the film phase, or *desorb*. In this regard, physisorption is distinct from *chemisorption*, which is a related phenomena whereby molecules are bound by the formation of chemical bonds between the gas and substrate. The weak binding in physisorption implies that an adsorbent can, in principle, be used indefinitely as its surface can be 'cleaned' by simple heating to remove adsorbed molecules, and pumping away the vapour. The temperatures required to do this will depend on the species of gas being adsorbed and the nature of the substrate, as this determines the strength of the Van der Waals interaction binding the gas onto the surface.

Perhaps the most important aspect of adsorption is the effect of substrate morphology; materials that are composed of very fine powders present more surface area for adsorption by simple geometry than a simple cube of the same material. Other materials like zeolites and activated carbons are riddled with a network of micro-pores that are nanometres in diameter which expose ever more surface area for adsorption. It is not uncommon for zeolites and activated carbons to have specific areas in excess of 1000 m^2 /g. More recently, new records are being set by the Metal Organic Framework (MOF) class of materials, which have been recorded as having specific areas as large as 7000 m^2 /g [9]. These materials are being investigated for their promise as a hydrogen storage medium.

A key consequence of substrate morphology is that the surface may differ from the idealized atomically flat surface represented in figure 1.1. Real surfaces are not perfectly homogeneous; they have defects or imperfections that lead to heterogeneity - variation in the binding potential. The search for a practical exfoliated graphite substrate which minimises this heterogeneity is the goal of this work.

A vital tool in the study of adsorption is the vapour pressure adsorption isotherm, which is explained in greater detail in section 4.2. Isotherms characterise the dependence of the number atoms in the adsorbed film as a function of the vapour pressure. Some example plots are shown in figure 1.2

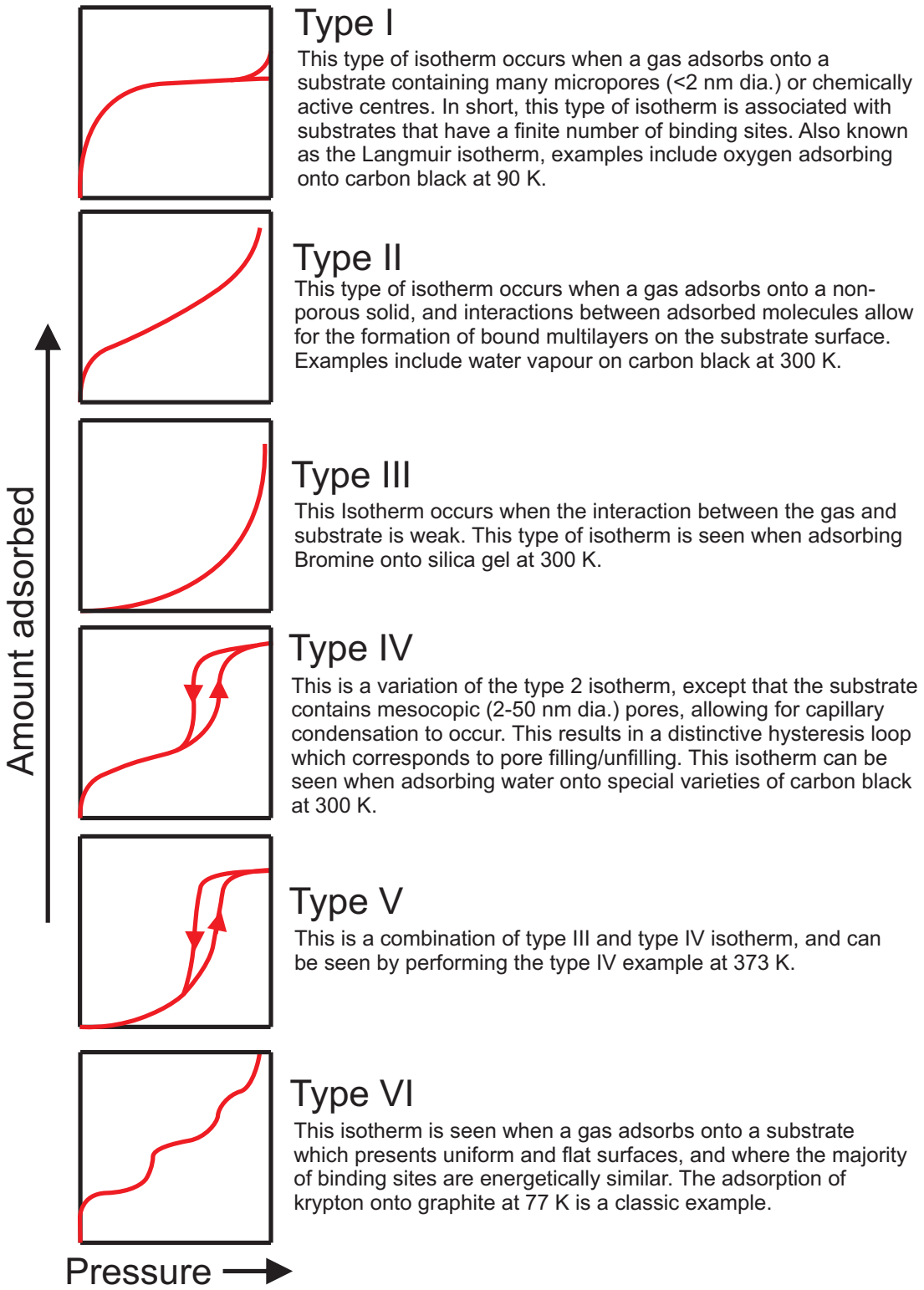

Figure 1.2: The six IUPAC [10] isotherm classifications. Such plots can be used to make inferences regarding substrate morphology.

1.2 Adsorption onto Graphite: Some History

The isotherm types I-V shown in figure 1.2 are characteristic of adsorption onto *heterogeneous* media i.e. solids that present a variety of surfaces and pores for adsorption with many different binding energies. Such isotherms can be interpreted readily within the framework of Brunauer, Deming, Deming and Teller [11].

The type VI isotherm is sometimes known as *stepwise* adsorption whereby thin films are grown sequentially layer by layer onto a flat and energetically homogeneous surface. Each 'step' in the isotherm can be interpreted as the completion of a distinct layer of adsorbate which is just one atom or molecule thick. Guggenheim and Fowler [12], Halsey [13] and Hill [14] were among the first to predict that stepwise film growth behaviour could be seen in an adsorption isotherm if the substrate was sufficiently homogeneous.

The first conclusive observations of such stepwise growth was seen by Polley [15] who adsorbed argon, oxygen and nitrogen onto a variety of graphitised carbon blacks. Polley was also the first to demonstrate the importance of graphitisation on the growth of these multilayer films; the carbon blacks were subjected to varying levels of heat treatments and analysed via X-rays. Samples that were treated at higher temperatures showed greater levels of graphite crystal growth along with increased sharpness in the isotherm steps that was correctly attributed to the increased lateral size of the exposed (001) faces onto which the adsorption was taking place.

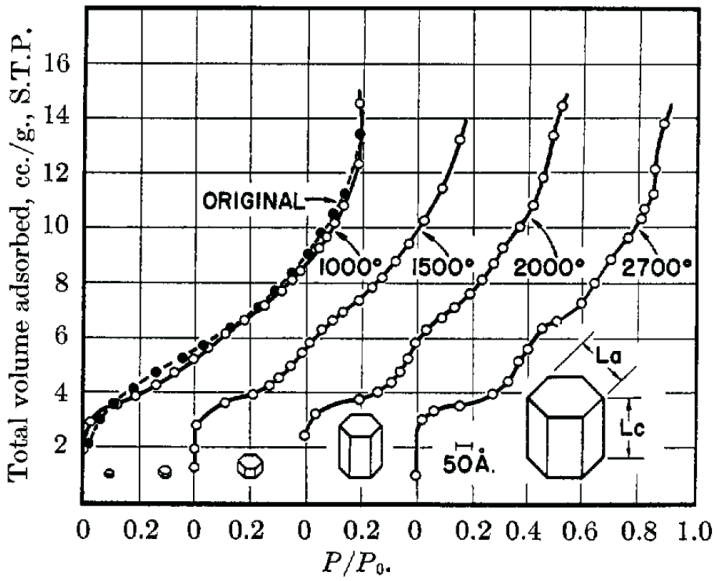

Figure 1.3: Argon isotherms at 78.15 K performed on carbon blacks subjected to different heat treatments [15]

Similar stepwise isotherms were subsequently observed on a variety of substrates, notably the alkali metal halides [16], and various layered compounds such as boron nitride [17] and $NiCl_2$ [18].

A major innovation came from Duval and Thomy [19] who had been using a new class of graphite substrate for studies of krypton and xenon films. The new substrate was created by subjecting graphite to a process called exfoliation which is explained in greater detail in sections 2.1 and 2.2. This new exfoliated graphite substrate showed a dramatic increase in the sharpness of steps of krypton and xenon vapour pressure isotherms. Additionally, highly detailed measurements revealed previously unseen structure in the first monolayers of xenon and krypton that were attributed to phase transitions within the film. Figure 1.4 shows some krypton isotherms, where analogy is made to the bulk phase diagram of krypton.

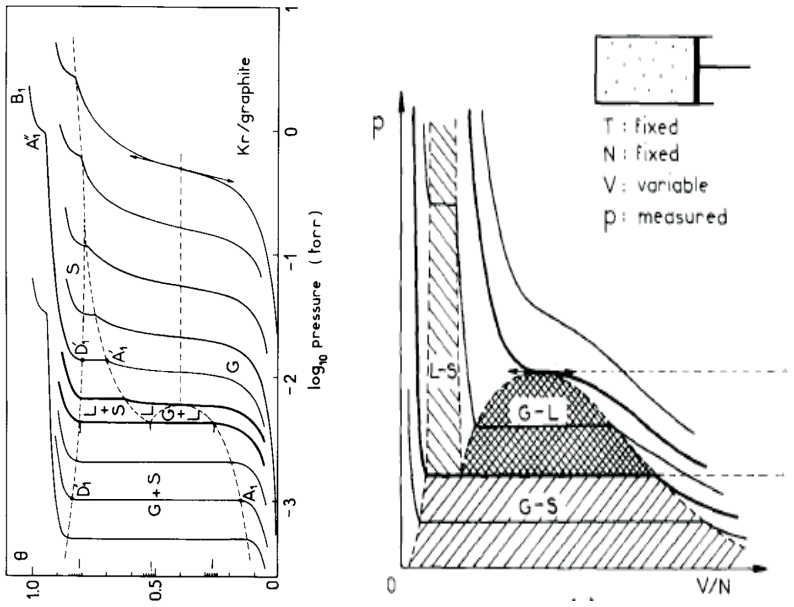

Figure 1.4: Figures taken from [20] showing the analogous phase behaviour of two dimensional and bulk matter. Left: isotherms of the first monolayer of krypton on graphite taken at temperatures 77.3, 79.8, 82.3, 84.8, 88.0, 91.8, 96.6, 102.6 and 109.5 K. A proposed phase diagram is drawn over the top of the data. Right: isotherms of pressure versus V/N as would be found in an isothermal piston compression.

With their work, Duval and Thomy were able to show that krypton and xenon on graphite was an example of two-dimensional matter, complete with phase transitions, critical points and perhaps most importantly, an ordered solid phase. This lead to the widespread adoption of exfoliated graphite by other researchers [21]. Commercially available exfoliated graphites such as Grafoil [22] and Papyex [23] were subsequently used for adsorption studies, and the sub-monolayer phases of many gas-graphite systems were explored with a variety of techniques. In particular, neutron scattering was first used by Kjems [24, 25] to dynamically probe the structure of a monolayer film of nitrogen as it adsorbed onto a Grafoil substrate. Others [26, 6, 27] were able to use the scattering formalism developed by Kjems

et al. to elucidate phase diagrams for a variety of other simple gases on graphite. A common feature in many of these studies is the formation of a commensurate $\sqrt{3} \times \sqrt{3}$ solid right at the point of monolayer completion. This commensurate solid, which is shown in figure 1.5, formed the basis of many studies testing theories of 2D melting first developed by Kosterlitz and Thouless. The articles by Dash [21], Birgeneau [7] and Nelson [28] give excellent overviews of the techniques and theory involved in early work on 2D solids formed onto graphite.

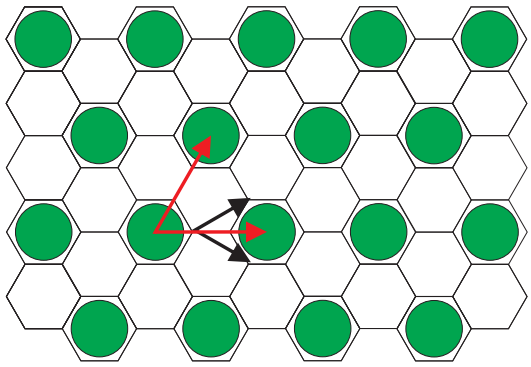

Figure 1.5: Simple schematic of the $(\sqrt{3} \times \sqrt{3})$ $R30°$ commensurate phase of a simple monotomic gas adsorbed onto the (001) face of graphite. The black arrows show the graphite lattice vectors, and the red arrows show the adsorbed superlattice vectors, which are $\sqrt{3}\times$ the length of the graphite vectors and rotated by 30 °. The $(\sqrt{3} \times \sqrt{3})$ $R30°$ is an example of a superlattice expressed in Woods' notation [29, 30]

1.3 Motivations: Monolayer Superfluidity

Of the many scientific discoveries made during the 20^{th} century, the observation of superfluidity in liquid ^{4}He is perhaps one of the most bizarre, and yet well-understood of natural phenomenon. Soon after its discovery, much work was dedicated to the study of thin films of adsorbed ^{4}He, particularly with regards to the effect of film thickness on superfluid behaviour. One of the first studies was performed by Frederikse [31] in 1949, who carefully recorded the λ-point [1] for adsorbed helium films of varying thickess. His results, shown in figure 1.6, show that as the film thickness was decreased, the λ-transition was seen to occur at lower temperatures, whilst simultaneously decreasing in height and sharpness. At a thickness of 3 atomic layers, no transition could be observed, suggesting that superfluidity is effectively suppressed in the two-dimensional limit.

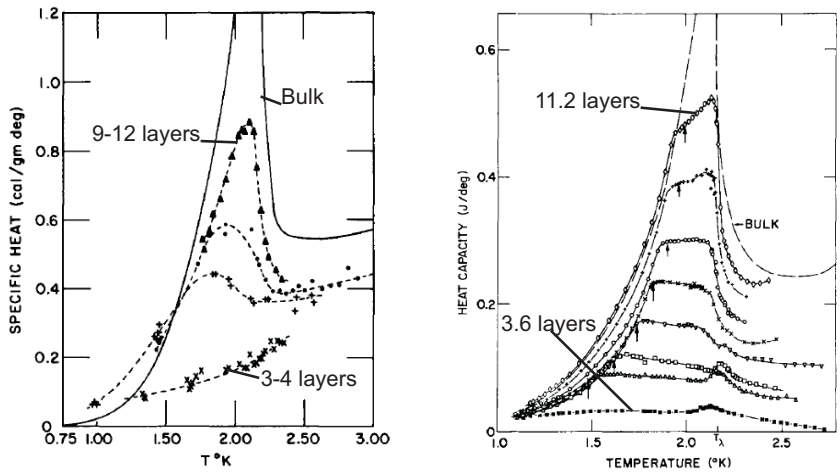

Figure 1.6: Graphs showing the suppression of the λ-transition in films with decreasing thickness. Left, data of Frederikse [31] obtained using Fe_2O_3 (jewellers rouge) as a substrate. Right; data obtained by Bretz [32], obtained using a Grafoil substrate.

[1] The heat capacity of liquid ^{4}He as a function of temperature displays a very distinctive discontinuity, which is shaped like the greek symbol λ. This so-called λ-point occurs at 2.172 K, 1 atm for bulk helium and signals the onset of superfluidity.

Subsequent work by Bretz [32] showed that similar behaviour could be seen in helium films adsorbed onto Grafoil. As can be seen from figure 1.6 however, there were qualitative differences; rather than rounding with decreased film thickness, the λ-transition becomes increasingly truncated, and hints of the transition can be seen in a film only 3 atomic layers thick. These differences were attributed to the increased homogeneity of the Grafoil substrate.

Using a torsional oscillator and mylar as a substrate, Bishop and Reppy [5] were able to show the superfluidity can exist in films as thin as 2.4 atomic layers, with the behaviour being consistent with the predictions of Kosterlitz and Thouless regarding superfluidity in two dimensions.

Further work by Crowell and Reppy [33] had shown that superfluidity could be observed in the second helium layer, with the first monolayer serving to screen the effects of a disordered substrate potential. This lead to the the question of whether a superfluid could be observed in sub-monolayer films of ^{4}He. The first such observation was made by Nyeki et al. [34], in a monolayer ^{4}He film adsorbed onto graphite that had been pre-plated with hydrogen and deuterium.

After the discovery of superfluidity in ^{3}He by Lee, Osheroff and Richardson [35], much theoretical and experimental work has been devoted to the study of ^{3}He films, with particular regards to what form, if any, a two-dimensional ^3He superfluid will take.

Much information has come from the study of ^{3}He films in confined geometries [36, 37], where the principle being that if the confinement length is similar in size to the *superfluid coherence length*, ξ then superfluidity is seen to be suppressed in that dimension. In superfluid ^{3}He at zero temperature, ξ_0 can be interpreted as the typical separation size of the Cooper pairs. To date, no superfluid, or superfluid-like phase has been observed in a monolayer ^{3}He film.

As is discussed in section 2.2.1, a graphitic substrate is modelled essentially as a

collection of plate shaped crystallites (otherwise known as *platelets*) with adsorption primarily occurring at the (001) faces of these platelets. The *surface coherence length* of the substrate, which is also discussed in greater detail in section 2.2.1, is the typical distance over which adsorbing surfaces of a substrate can be considered to be atomically flat. Estimates of surface coherence lengths of graphitic substrates obtained by scattering from adsorbed monolayers give the typical surface coherence lengths of 20 nm for Grafoil and 160 - 200 nm for ZYX [6].

To understand why superfluidity has not yet been seen in adsorbed ^{3}He monolayer films, it is best to explain via some numerical values; in bulk ^{3}He, ξ_0 is strongly dependent on pressure; at 0 bar $\xi_0 = 77$ nm, whilst at 35 bar this drops to $\xi_0 = 20$ nm [38]. Although no calculations exist regarding the theoretical value of ξ_0 in a 2D ^{3}He superfluid, it is known from measurements of ^{3}He in constrained geometries that the superfluid can be measurably suppressed by restricting the confinement geometry to as little as $10\xi_0$. By contrast, the superfluid coherence length in ^{4}He is found to be on the order of 0.1 nm [39], which explains why the superfluid phase has been observed in very thin ^{4}He films, even when using relatively heterogeneous substrates such as mylar. The current thinking is that the ^{3}He monolayer superfluid is suppressed because ξ_0 is comparable to the surface coherence lengths of even the most homogeneous of substrates; the surface heterogeneities serve to constrain and suppress the superfluid.

This forms one of the primary motivations for this project; the creation of a new graphitic substrate with exceptionally large surface coherence lengths (ideally on the order of several ξ_0 at least), which would allow for the formation and subsequent observation of a superfluid, or some other novel phase in monolayer ^{3}He.

Chapter 2

Graphitic Substrates

Whilst there are many possible substrates used in the study of adsorbed films, graphitic substrates are arguably the most common. A combination of characteristics make graphite an almost ideal substrate for the creation of two-dimensional matter via thin adsorbed films. In particular, the lamellar structure of graphite, as shown in figure 2.1, is highly anisotropic; the bonding between layers is much weaker than within the plane, which means that graphite will preferentially cleave basally. This means that graphite often forms in platelet shaped crystals which will overwhelmingly present (001) faces as surfaces for adsorption, which save for some corrugation in the binding potential due the graphite hexagons, is energetically homogeneous and almost perfectly flat on an atomic scale. These surfaces are also very easy to clean; due to graphite's refractory nature and its relative chemical inertness, heating to 1000 ° C under vacuum is sufficient to remove most contaminants from the graphite (001) faces [40]. Graphite also has a fairly high thermal conductivity in the planes, which makes it amenable for use in low temperature studies of thin helium films.

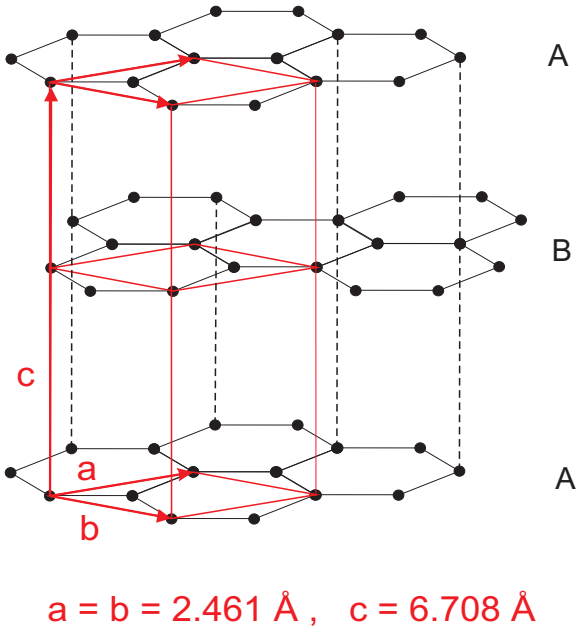

Figure 2.1: Diagram showing the basic structure of graphite, with the unit cell outlined in red. The spacing between graphite layers is 3.354 Å [41], with layers stacking in an ABAB... sequence. Within the plane, the interatomic distance is 1.421 Å.

Typically, a normal graphite crystal presents only a few (001) surfaces for adsorption meaning that in order to achieve an appreciable surface area the number of these faces must be increased greatly. There are two approaches; to use a fine graphite powder or to subject a graphite source material to an exfoliation process. Thomy and Duval [20] performed studies of krypton and xenon films adsorbed onto both powdered and exfoliated graphites, but it was found that the exfoliated graphites produced the sharpest and most detailed vapour pressure isotherms.

It should be noted that the production of graphene using the so-called 'scotch-tape' method [42], is an example of *mechanical exfoliation*. Exfoliated graphite in the context of this project is taken to mean the material that is produced when precursor graphite intercalation compounds are thermally decomposed. This *chemical exfoliation* is the method used to produce Grafoil, Papyex and ZYX.

2.1 Graphite Intercalation Compounds (GICs)

Graphite intercalation compounds (GICs) are materials where a foreign species has been inserted - intercalated - in between the layers of a host graphite material. During intercalation the newly formed GIC can display a range of structural ordering, the most striking of which is the phenomenon of staging. As shown in figure 2.2, staging is the tendency for intercalant layers to form at periodic intervals along the c-axis of the host graphite. The stage index, n, is used to classify a GIC and denotes the number of graphite layers between intercalant layers. This staging is coherent over long ranges, as such it is possible to measure via X-ray diffraction and stage indexes as high as 10 have been observed [43].

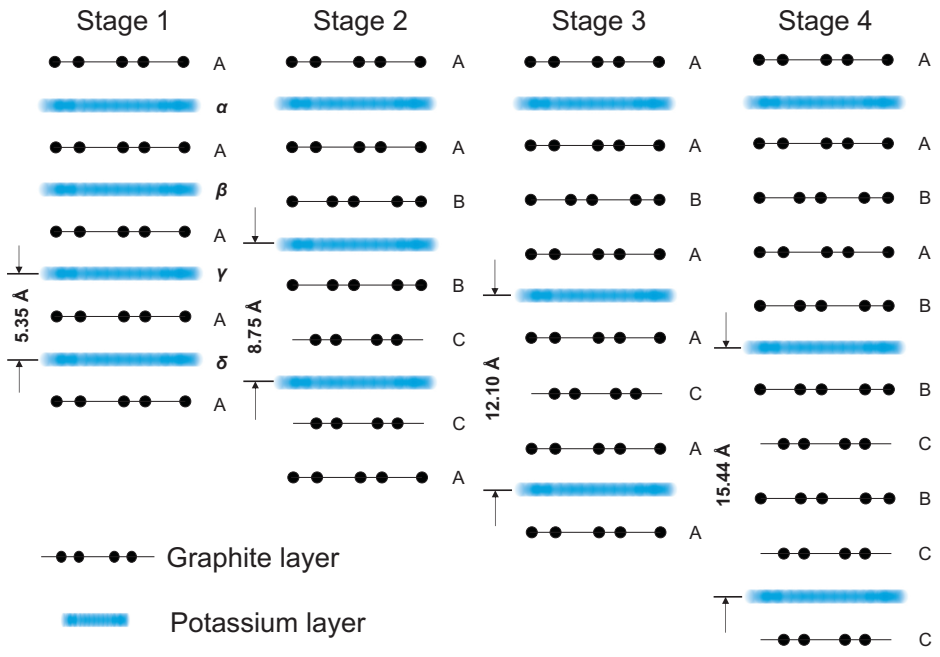

Figure 2.2: Schematic reproduced from the review by Dresselhaus [44] illustrating the staging phenomenon in potassium intercalated graphite for stages 1 to 4. Also shown is the stacking sequence of graphite and potassium layers where it is applicable.

In addition to stage ordering these intercalant layers can form 2D solid and liquid phases in analogy to the monolayer phases described in section 1.2, for example in stage-1 potassium-graphite, KC_8, the potassium forms a commensurate 2×2 structure which is also associated with a specific stacking sequence of the graphite and intercalant layers; AαBβAγAδ, where greek letters refer to the intercalant stacking and A refers to the graphite layers [45]. For higher stage potassium graphite compounds (KC_{12n}, $n > 1$) the intercalant layers are are liquid like and only solidify at low temperatures, but this solid structure has not yet been fully elucidated [46] . The graphite layers are known to retain the innate AB stacking sequence with the minor modification [47]:

KC_{24}	Stage 2	AB|BC|CA|A
KC_{36}	Stage 3	ABA|ACA|A
KC_{48}	Stage 4	ABAB|BCBC|CACA|A

Both GICs and intercalants can also be classified according to the charge transfer that takes place during intercalation; donor type intercalants will contribute electrons to the graphite and produce a donor GIC. Conversely, an acceptor type intercalant will take electrons from the graphite to produce an acceptor GIC. The classic examples of donor GICs are those formed from alkali and alkaline earth metals. Similarly, acceptor GICs are usually made with intercalants that are strong oxidising agents; Br_2, HNO_3 and $SbCl_5$ being common examples [44].

It is also possible to form composite GICs comprised of more than one intercalant. GICs with one species of intercalant are referred to as binary GICs, whilst those with two and three different species are referred to as ternary and quaternary compounds respectively. Ternary compounds based on hydrogen/alkali and hydrogen/alkali metals have recently been investigated as a potential hydrogen storage technology [48, 46], however most work on ternary compounds is based on organic solvents and alkali metals. Higher order compounds (quaternary, quinary etc.) are based on

solvent mixtures and alkali metals [49], however such compounds currently are of little interest, and so far they appear to hold no technological promise.

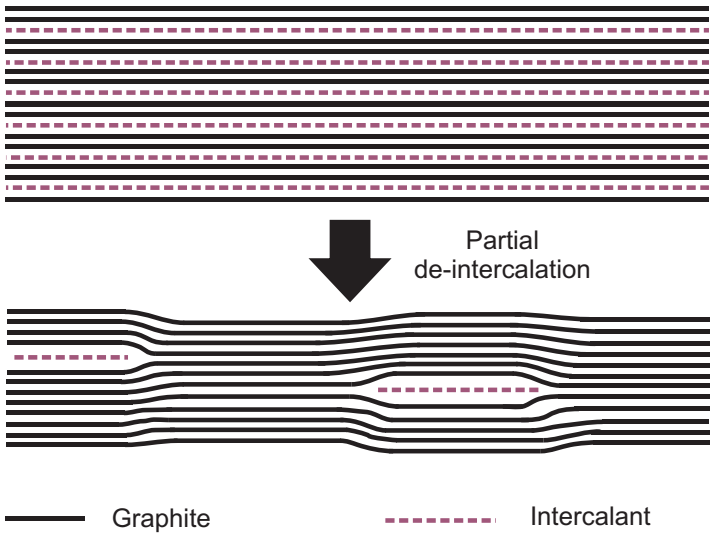

Figure 2.3: Schematic diagram showing the de-intercalation from a well layered intercalation compound (in this case stage-2) to a residue compound, where small intercalate island remain trapped between dislocation loops.

Many GICs will desorb their intercalants to form residue compounds when removed from the intercalating environment, whereby the well organised lamellar structure of the GIC is lost leaving a material with significantly reduced intercalant concentration. As is shown in figure 2.3, the intercalant layers become isolated intercalant islands, which tend to become trapped at defects such as dislocation loops [50]. A good example of this occurs in the bromine-graphite system; intercalating graphite with bromine to stage-2 gives the compound BrC_7 which will gradually desorb bromine, if left in air, to form a stable residue compound, BrC_{100} (approximate stoichiometry) at which point further desorption ceases. Similarly, in the Grafoil production process, the graphite-bisulphate compound is diluted down to a residue compound by rinsing in water. These residue compounds are then heated to produce

the desired exfoliation, however as shall be discussed in the next section, some of these residue compounds can display unusual exfoliation properties. It should also be noted that potassium GICs do not form residue compounds.

With all the possible intercalants and stagings that can be chosen, it is unsurprising that graphite intercalation compounds display a diverse array of physical properties; superconductivity has been observed below 1 K in stage-1 compounds of Potassium, Rubidium and Caesium [51] and more recently a stage-1 compound, CaC_6 was found to superconduct below a T_c of 11.5 K [52]. In a similar vein, GICs based on the metal-pentafluorides such as C_xAsF_5 produce compounds with room temperature conductivities that rival or even surpass [53] copper.

In recent years with the research explosion into graphene, there has been renewed interest in graphite intercalation compounds as a means of exfoliation. An active area of research is to produce GICs in such a way that when immersed in an appropriate solvent, charged bilayer or monolayer graphene sheets spontaneously dissolve to form a graphene solution which can be used as a form of graphene paint [54, 55]. The exfoliation of graphite intercalation compounds via thermal decomposition is the method that has been applied during this project. For a more complete review of GICs, the interested reader should consult the reviews by Dresselhaus [44] and Enoki [56].

2.2 Exfoliation of Graphite

Essentially, the exfoliation of graphite intercalation compounds by heating occurs due to the vaporisation of the intercalant, which is confirmed by various thermodynamic measurements[57]. This vapour then drives an expansion of the graphite along the c-axis that is consistent with ideal gas law behaviour as shown by *in-situ* force measurements exerted by the expanding graphite [58, 59]. Exfoliation results

in expanded worm like structures, as is shown in figure 2.4. This expanded graphite is still graphite chemically and crystallographically, except that the macroscopic crystal structure has been significantly disrupted. This new material has a lower density and significantly increased specific surface area compared to the original starting material.

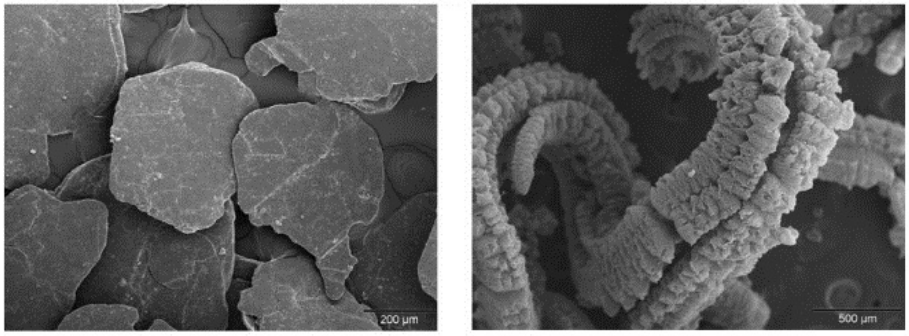

Figure 2.4: SEM images taken from [60] showing GIC flakes before (left) and after (right) exfoliation.

Exfoliation of graphite was described as early as 1916 [61], however measurements performed by Martin and Brocklehurst [62] and Anderson and Chung [63] showed that in special circumstances there can exist two types of exfoliation; reversible and irreversible. Reversible exfoliation is seen particularly in the residue compounds of bromine-graphite. These compounds, which typically displayed a stoichiometry of approximately BrC_{100}, expand along the c-axis if raised above a certain breakaway temperature, T_B. Once cooled, the compound collapses down returning to roughly its original size. Subsequent heating/cooling then produces remarkably repeatable expansion/collapse cycles, though it was shown by Anderson and Chung that each cycle is associated with a net loss of bromine, fundamentally limiting the total number cycles that can be performed. It was also demonstrated that different graphites have different breakaway temperatures; pyrolytic graphites show reversible expansions at lower temperatures than polycrystalline graphites. This lead to the idea

[62, 64] that the expansion is driven by defects; the increased temperature promotes mobility of the intercalant, which eventually collects at defects and grain boundaries forming disk shaped agglomerations which cause an initial small expansion. Further heating then causes intercalant vaporisation at these agglomerations forming bubbles, the pressure of which then drives the expansion along the c-axis. Anderson and Chung disagree with the notion that intercalants are trapped by defects and dislocations, rather they posit that the bubbles form at the overlaps between intercalant islands, which then serve as mobile nucleation points within the graphite structure.

The criterion for irreversible exfoliation then rests on the inability of the vaporised intercalant to escape from these gas bubbles. In the reversible scenario, the bubbles are generally leak tight, (though diffusive losses do occur) which means the intercalant is trapped inside the bubbles. Cooling then results in the atmospheric pressure collapsing the bubbles as the intercalant re-condenses or re-intercalates. If however the temperature is high enough to force a very large expansion, then the vapourised gas will readily escape through the large ruptures this creates, leaving the graphite permanently altered. In the case of graphite-bisulphate exfoliation, the expansion is driven by the rapid thermal decomposition of the H_2SO_4 intercalant into inert gaseous products (H_2O,SO_2, SO_3) which are unable to re-intercalate, thus this particular process is irreversible. It should also be noted that if the flake size is too small ($L_a < 75\mu$m or $L_c < 75$ nm [65])[1] then exfoliation is negligible as the intercalant is able to diffuse away before any bubbles can be formed.

The extent of exfoliation can be measured in a variety of ways, though the change in surface area and the expansion ratio along the c-axis are the main methods described in the literature. All these measures are influenced by the exfoliation temperature, with a sigmoid dependence as shown in figure 2.5.

[1]The parameters, L_a and L_c correspond to in-plane and c-axis dimensions of flakes and crystals, as illustrated by the diagram in figure 2.6.

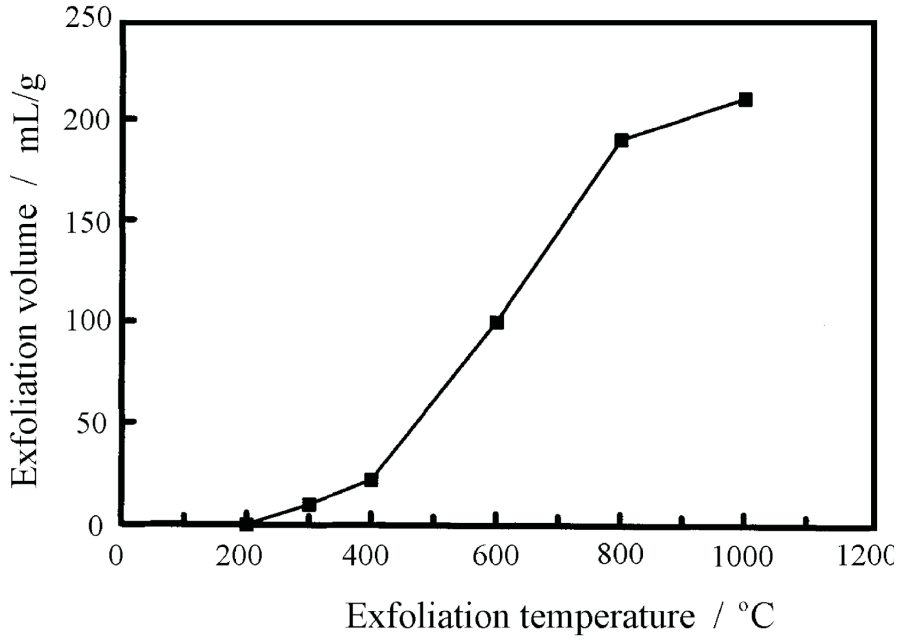

Figure 2.5: Graph reproduced from [66], showing the temperature dependence of graphite expansion

Exfoliated graphite is primarily used in gasket applications; by compressing the expanded material it is possible to form malleable and flexible graphite foils which are exceptionally heat resistant and chemically inert. Such materials are commercially available under the trade names of Grafoil and Papyex, whose physical properties are outlined in table 2.1. For a more complete account of exfoliated graphites, its properties and applications the interested reader should consult the reviews by Chung [65] and Inagaki [66].

2.2.1 Structure of Exfoliated Graphites

The common model of an exfoliated graphite is that of a loosely bound powder of irregularly shaped crystallites which are sometimes referred to in the literature as *platelets*. As can be seen from figure 2.6, these platelets can be characterised by

the dimensions, L_a and L_c which describe the typical in-plane width and the c-axis thickness respectively. Many important properties such as the specific area, the mosaic spread and the substrate homogeneity can be gleaned by consideration of the size, shape and orientation of these platelets. As will be discussed in section 4.1, the values of L_a and L_c can be estimated from the respective broadening of $(hk0)$ and $(00l)$ reflections obtained from X-ray powder diffraction measurements.

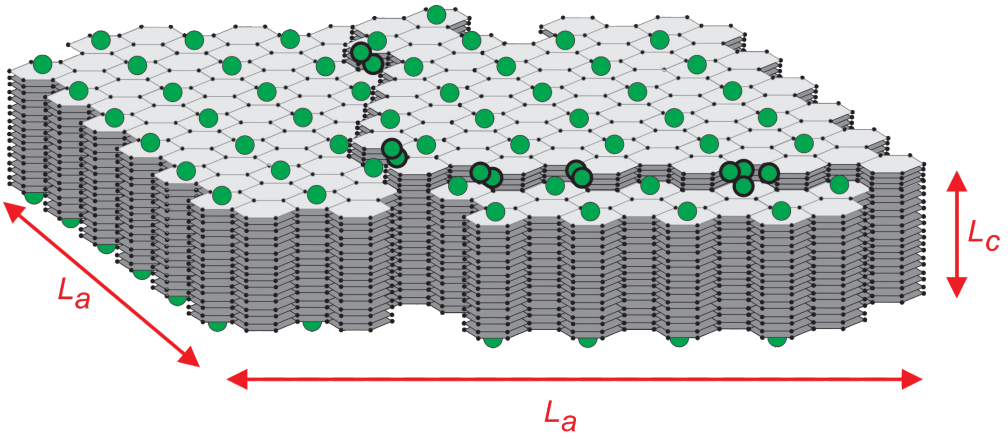

Figure 2.6: Basic model of a crystallite in an exfoliated graphite, including surface step edges and heterogeneities. The diagram also shows the formation of a commensurate solid adsorbed onto the surface, whilst binding at alternate sites created by heterogeneities in the adsorbing face is represented by the atoms with the emboldened black outline. The quantities L_a and L_c represent the in-plane and out of plane crystallite dimensions respectively. The surface coherence length, L_s can be interpreted as the lateral size of the adsorbed commensurate solid, and this is discussed in the text. More simply, L_s can be thought of as the typical distance between surface heterogeneities such as step edges and other (001) face imperfections.

As has been previously mentioned in section 1.1, large specific areas are characteristic of materials composed of small particles, and as such exfoliated graphites composed of small platelets present greater areas for adsorption than those composed of large platelets. This is confirmed by the data in table 2.1 which shows that ZYX with crystallites much larger than Grafoil, has a commensurably smaller specific area. Substrates with larger specific areas are able to adsorb more gas,

and produce correspondingly larger signals in scattering, NMR, torsional oscillator and heat capacity measurements. The standard method of measuring exfoliated graphite specific areas is by vapour pressure isotherm of nitrogen or krypton and this is described in section 4.2.

The schematic presented in figure 2.6 suggests that platelets in exfoliated graphite typically have some aspect ratio such that $L_a > L_c$. The consequence of this is that when an exfoliated graphite powder is compressed to make a foil such as Grafoil or Papyex, the randomly oriented platelets will then assume a preferred alignment whereby their c-axes line up with with the axis of compression. There is however no preferential alignment of the crystallites in-plane and the substrate can be considered as a 2D powder.

Naturally, this preferential alignment is not perfect and the c-axis of each crystallite will be at some angle, Θ relative to the compression axis. As is shown in figure 2.7, the whole ensemble of crystallites in the substrate can then be described by a distribution of angles, with some characteristic width, Θ_m called the mosaic spread. The mosaic spread is an important quantity in scattering, NMR and torsional oscillator measurements as the variation in substrate alignment represents an uncertainty factor that must be accounted for during analysis. Substrates with small mosaic spreads are preferred.

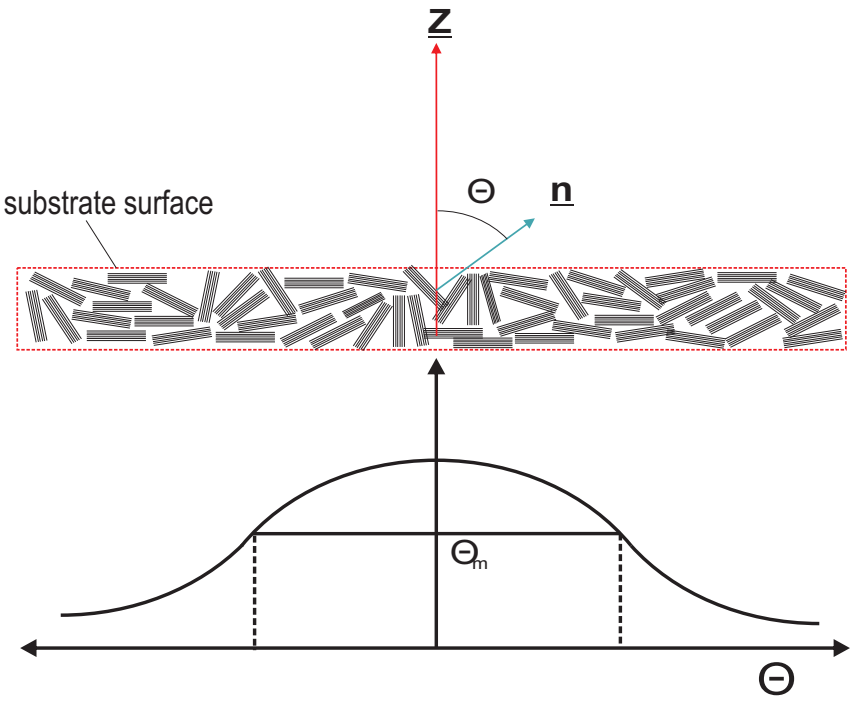

Figure 2.7: Schematic description of the mosaic spread of a graphite substrate.

There are two methods described in the literature for determining mosaic spreads. The first, and simpler method is by performing rocking curves on diffracted $(00l)$ reflections, and is described in more detail in section 4.4. The second, more complex measurement, involves the analysis of two-dimensional (hk) reflections of the kind that are obtained from monolayer scattering experiments. When certain gases adsorb onto graphite they will often form commensurate phases which can be considered as a 2D crystal. Collections of such 2D crystals produce distinctive "sawtooth" lineshapes which were first predicted by Warren [67]. These lineshapes, such as the one shown in figure 2.8, can be analysed using the formalism first developed by Kjems et al. [25] to determine various properties of the 2D crystals such as their typical size and mosaic spread.

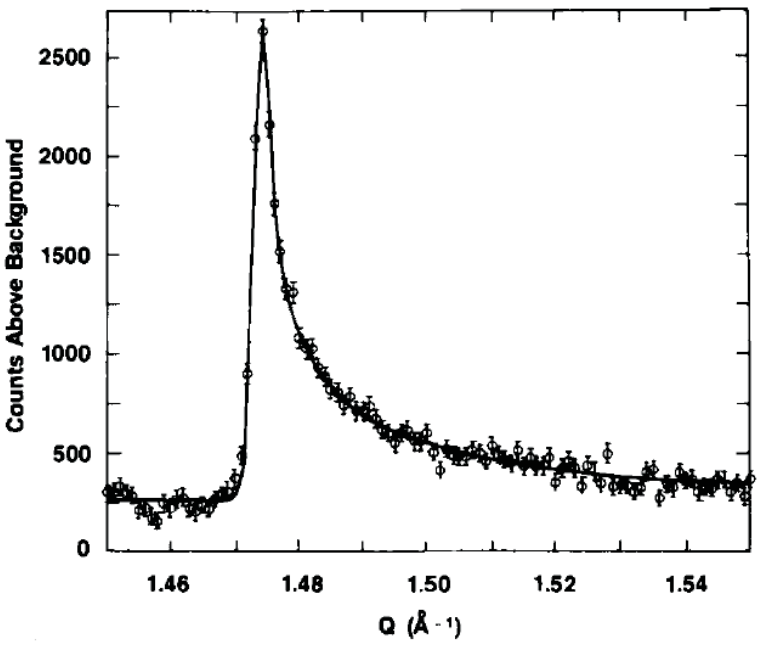

Figure 2.8: Example of a 2D diffraction peak obtained using synchrotron radiation. This (10) peak results from a commensurate 2×2 monolayer of CF_4 adsorbed onto ZYX [68]. The mosaic of the 2D crystallites can be obtained by modelling a profile to the long trailing edge of the peak. After the mosaic contribution has been deconvolved the 2D crystallite size can be estimated from the peak width.

It is also possible to use monolayer scattering techniques to estimate what proportion of a substrate adsorption surface can be considered to be atomically flat. The top face of the graphite crystallite in figure 2.6 has been divided by a step edge heterogeneity into approximately two homogeneous and flat regions. The surface coherence length, L_s denotes the typical lateral size of these regions. When commensurate solids form onto the surface of graphite, their lateral size is thought to be limited by heterogeneities in the graphite substrate, where a step-edge just one graphite layer high can disrupt the two-dimensional ordering. By analysing the diffracted (hk) peaks produced by a commensurate solid at monolayer completion, it is possible to estimate the typical size of the diffracting 2D crystallites, which by

extension can be used to infer a value for the surface coherence length. The (10) peak shown in figure 2.8 corresponds to a surface coherence length of 2200 Å [68].

Figure 2.6 is also used to justify one of the central assumption of this project: the lateral crystallite size, L_a must necessarily be larger than the surface coherence length. Further justification for this is given in the next section where the production process and physical properties of Grafoil, Papyex and ZYX will be summarised.

2.3 Grafoil, Papyex and ZYX

A review of the literature such as the one by Godfrin [69] will show that thin film researchers favour three main brands of exfoliated graphite; Papyex from Carbone Lorraine[23], and Grafoil and ZYX from Union Carbide (UCAR) [22]. Both Papyex and Grafoil are commercially available and are used primarily in gasketing and sealing applications. Grafoil and Papyex are fundamentally similar, both being manufactured in a process whereby finely ground particles of mined graphite are intercalated with a H_2SO_4/HNO_3 mixture, then rinsed with water to produce a residue compound. This compound is then subjected to intense heat (900-1200 °C) to initiate exfoliation [66]. The exfoliated graphite is then compressed via rollers into a flexible foil-like material which is able to hold together without the aid of binding agents. Further heating is applied to drive off impurities and any remnant intercalant. The similar providence of Grafoil and Papyex means that they have similar physical properties as can be seen from the values in table 2.1.

It should be noted that there are references in the literature to graphite substrates called UCAR-foam and Uncompressed Exfoliated Graphite (UEG) [6, 70]. These materials are the precursor exfoliated graphites which are then compressed to form Grafoil and Papyex respectively. These substrates are rarely used however, and the data concerning their physical properties is somewhat inconsistent, which is also

presented in table 2.1.

ZYX is a bespoke material made especially for adsorption studies [71], and was intended originally as an improvement on Grafoil and Papyex, on the premise that a substrate exfoliated from a highly crystalline graphite would produce very homogeneous adsorption surfaces. ZYX can be roughly divided into two types; UCAR-ZYX and lab-made ZYX. Both are manufactured using Highly Oriented Pyrolytic Graphite (HOPG) as a source material, though the original UCAR-ZYX is made from ZYA grade HOPG [71] which is considered to be superior to the ZYH grade which has been used in lab-based recipes reported elsewhere [72, 73]. HOPG is made by pyrolysing hydrocarbons at high temperatures ($> 3000\ ^\circ$ C) whilst simultaneously applying high uni-axial pressures. The higher grades of HOPG result from longer annealing times and display smaller mosaic spread and increased crystallinity. Both UCAR and lab-made ZYX are made by intercalating HOPG with HNO_3 and then heating at 600 °C to cause exfoliation [71, 73]. The expanded HOPG is then compressed as a single monolith.

Similar physical properties are reported for both UCAR- and lab-made ZYX [73], however it should be noted that the overwhelming majority of available physical data has been collected on the UCAR-ZYX substrate. For this reason, ZYX is then taken to mean UCAR-ZYX, and any references to lab-made ZYX will be indicated explicitly.

Substrate	Specific Area (m^2g^{-1})	Mosaic Spread (°)	L_c (Å)	L_a (Å)	L_s (Å)
UCAR-Foam	27	powder	640	1150	900
Grafoil	18 - 30	± 15 **	100	400	100-200
UEG	42	powder	330	800	850
Papyex	20	± 15 **	**300**[74]	**600**[74]	200-300
ZYX	2 - 4	± 5 , < ± **1.5** [71]	1000	>3000	1600 - 2200

Table 2.1: Typical substrate properties compiled from [6] and augmented with data from [74]and [71]
**Grafoil and Papyex have a significant (70%) powder fraction

2.4 Summary

This chapter has given a general overview of graphitic substrates. Starting from the basic structure of graphite, relevant background to graphite intercalation and exfoliation processes has been covered in detail. A brief description of the structure of exfoliated graphite has been given along with some of the techniques that are used in the literature to characterise the substrates Papyex, Grafoil and ZYX. Finally, the manufacturing process of these substrates is discussed and their various physical attributes are presented in table 2.1.

The greater surface coherence lengths that are reported for ZYX are thought to be a consequence of the high crystallinity of the HOPG source material. In principle, if a source graphite of exceptional crystalline character is exfoliated, it seems reasonable to assume that this would produce a substrate with even greater surface coherence lengths than ZYX. The data presented in table 2.1 supports this assertion; all substrates with larger L_a crystallite dimensions have larger surface

coherence lengths, and the value of L_a is always greater than L_s for a given substrate, which is consistent with the crystallite model presented in figure 2.6.

The next chapter describes measurements that were performed to find a suitable graphite source material that was more crystalline than HOPG, in the hope that this would produce a highly homogeneous substrate, along with details of the intercalation and exfoliation method that was adopted to further maximise the homogeneity of prototype substrates.

Chapter 3

Substrate Manufacture

The summary in section 2.4 put forth the idea that the large surface coherence lengths of ZYX is a consequence of the high crystallinity of the HOPG source material. HOPG is not the most crystalline form of graphite and investigations were made into other potential source materials, until finally choosing a Madagascan natural flake graphite. We have also decided to drive the exfoliation process using a ternary Graphite Intercalation Compound (GIC) which has potassium and ammonia as intercalants. Exfoliation of this $K(NH_3)_x\ C_y$ compound is relatively novel with only one other report being found in the literature [75]. This intercalation process is described in detail and compared to the work of York and Solin [76]. The resultant GICs are then heated under vacuum to cause exfoliation, and the expanded material then pressed into disks or 'foils'. The exfoliation procedure is discussed in some detail, further discussion of the exfoliation procedure is given in the next chapter alongside the techniques that were used to characterise the new substrate 'foils'.

3.1 Graphite Source Material

As a graphite, HOPG is highly crystalline, especially when compared to the usual standard of natural flake graphite that is mined from the ground. The primary advantage of HOPG arises from its exceptionally narrow mosaic spread and the fact that it can be grown in a variety of shapes meaning that it is well suited for monochromator applications. By carefully sifting through large quantities of natural graphite it is possible to find natural crystal specimens [77] that are *exceptionally* crystalline, however these are rare and prohibitively expensive for bulk applications. Another source which is known to produce very crystalline graphite samples, occurs as a by-product of steel production. Such graphite is called kish.

3.1.1 Kish Graphite

An early candidate as a starting material was the so called kish graphite, which is formed as a by-product of the smelting process. When iron is smelted, carbon that is in excess of the solubility limit is precipitated out and floats on the top of the smelt where it forms a kish graphite crust along with other slag components. Predictably, smelts that are cooled slowly produce superior crystals to those that are cooled quickly [78, 79]. Kish graphite has long been known to produce crystals of a quality equal to, or better than, selected samples of natural graphite. Such is the size of the kish crystals, that it is impossible to assess the characteristic crystallite dimension via the methods described in section 4.1. However measurements of bulk properties such as the Residual Resistivity Ratio (RRR) [80] and electron channelling studies [81] show that high quality kish is composed of significantly larger crystallites than HOPG. One of the primary reasons that HOPG finds use in more applications, like X-ray monochromators, is the simple fact that HOPG can be grown in a variety of shapes and thickness to suit the users needs. Kish on the other hand is rarely much

more than 0.1 mm thick precluding it from many applications.

Given that kish originates off the top of iron smelts, the potential for magnetic contamination was a real concern, as such impurities would disrupt a sensitive NMR experiment. At this early stage we were lacking a reliable method to quantitatively compare impurity levels between various forms of graphite, however some headway could be made using other techniques. In fact similar work had already been done by Morishita [82] on Grafoil whereby he had performed magnetisation, Scanning Electron Microscopy (SEM) and Energy Dispersive Spectroscopy (EDS) on samples of Grafoil. We decided to replicate this work, using an existing stock of Grafoil GTA grade as a baseline for comparison.

To begin, a sample of kish was procured courtesy of Prof. Neal Skipper, who had received a large batch from Corus Steel. This sample consisted predominantly of a fine graphite dust (< 0.1mm diameter), with a few 1 mm sized flakes and a very few > 5 mm flakes. Magnetisation measurements were performed in-house whilst the EDS and SEM was performed at the RHUL Electron Microscopy Unit. Three samples were characterised; Grafoil GTA grade, untreated large flake kish, and large flake kish subjected to a washing procedure. This washing procedure consisted of immersion in 0.1 Molar Hydrochloric (HCl) acid for several days, rinsing in deionised water then baking under vacuum ($<10^{-5}$ mBar) at 1000 $^\circ$ C for 24 hours. The Grafoil was also baked out under the same conditions.

3.1.2 Magnetisation Measurements

Graphite is strongly diamagnetic and anisotropic; the diamagnetism is particular pronounced if the magnetic field is normal to the graphite basal planes. Any magnetic impurities like iron will therefore manifest themselves as deviations from this diamagnetic character which is observable by measuring the magnetisation as a function of applied field. Such measurements were performed using a Direct Cur-

rent Magnetisation System (DCMS) which is part of a Quantum Design Physical Properties Measurement System (PPMS) at Royal Holloway. Figure 3.1 shows the basic geometry of this system.

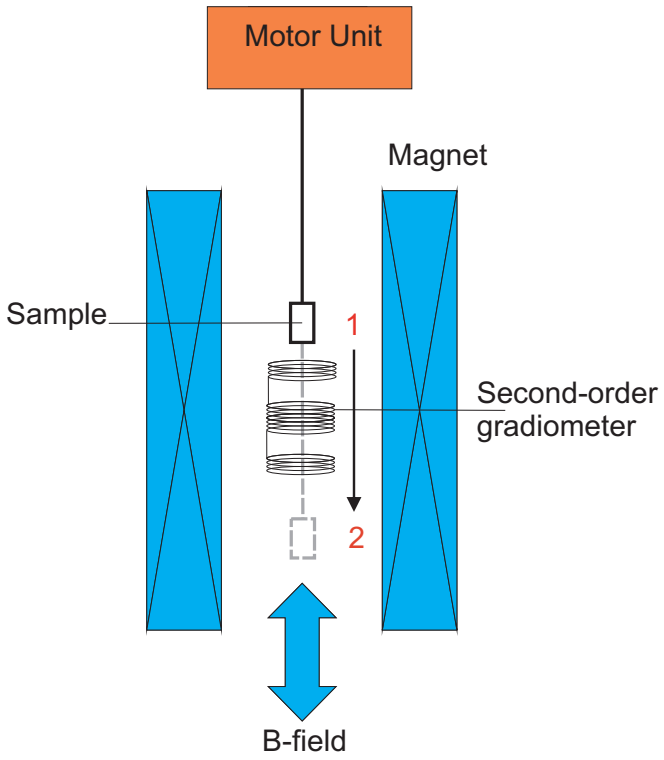

Figure 3.1: Basic outline of DCMS system; the sample is moved along a path from position 1 to position 2 and back again. During this transit, the sample is moved through a series of pick-up coils. These pickup coils record a voltage which can be used to calculate the sample magnetisation. The magnet is able to produce a field in either direction up to 9 Tesla.

To perform the measurement the sample is placed within a small container which is mounted on the end of a 90 cm rod. At the other end of this rod is a motor unit which is able to move the rod down by a few centimetres and then back up to its original position. During this trip the sample goes though a set of pickup coils. If a static **B** field is then applied, the sample will become magnetised. As the motor unit drives the sample through its range of motion, the pickup coils will experience

a change of flux $d\phi/dt$ which is measured as a voltage signal. The integral of this voltage signal is then proportional to the magnetisation of the sample, which coupled with knowledge of the polarity and strength of the magnetising field can be used to construct graphs of the sample magnetisation as a function of applied field. The sample is cooled by a helium gas flow drawn from the liquid helium bath in which the magnet is immersed.

This technique measures absolute magnetisation in Electromagnetic Units (EMU), it is therefore vital to know the masses of the samples. The data that is presented here has expressed the sample magnetisation in normalised units of EMU/g.

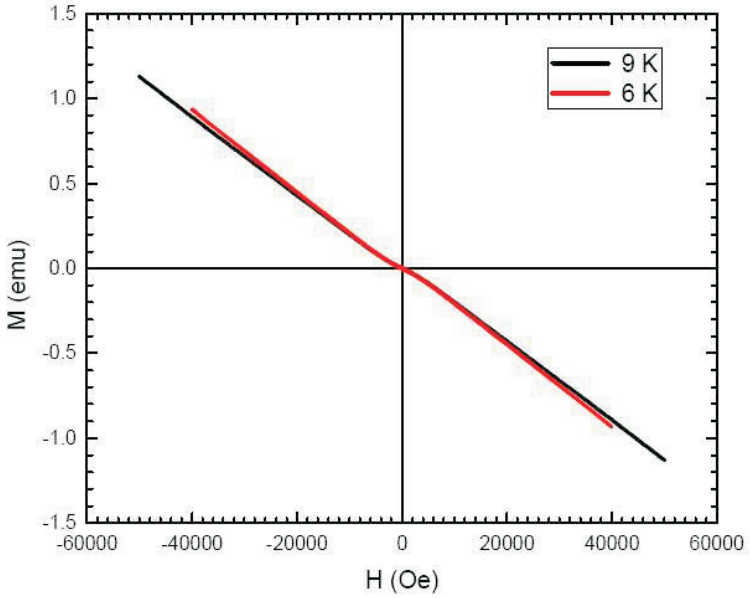

Figure 3.2: The magnetisation of a 0.0306g sample of GTA Grafoil at 6K and 9K: this graph shows the total magnetic moment in 'emu' (cgs) units of the sample as a function of applied field (Oe).

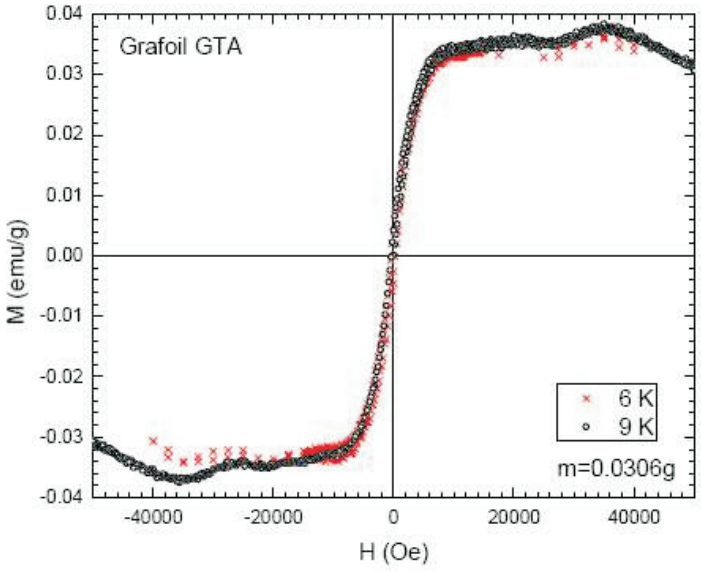

Figure 3.3: The magnetisation of Grafoil GTA with the linear diamagnetic contribution subtracted.

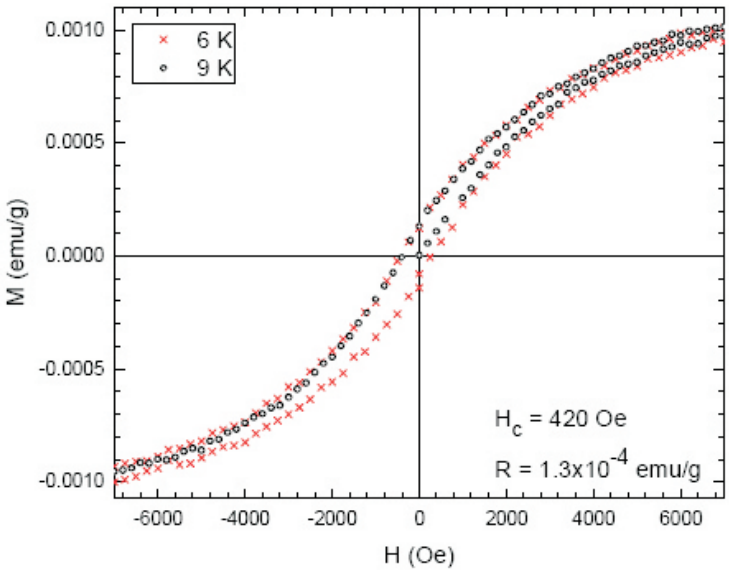

Figure 3.4: Closer inspection reveals that the residual magnetism is hysteretic. Values for the coercivity, $H_c = 420$ Oe and the remanence, R $= 1.3 \times 10^{-4}$ emu/g were calculated from the data. The saturation Magnetisation, $\mathbf{M}_{sat}$ was found to be 0.04 emu/g $= 4 \times 10^{-5}$ JT^{-1}.

The data is shown in figure 3.2; a straight inverse slope is characteristic of the diamagnetic response of graphite, where the magnetisation proportionally opposes any applied magnetic field. By fitting a straight line to the data, it is possible to remove the diamagnetic contribution of graphite. The result, which is shown in figures 3.3 and in 3.4 in greater detail, clearly shows that there is some ferromagnetic contribution to the magnetisation which saturates at low applied fields (8000 Oe). The saturation magnetisation, $\mathbf{M}_{sat}$ is 0.04 emu/g = 4×10^{-5} JT^{-1}/g.

The ferromagnetic behaviour observed here is consistent with the results of Morishita [82] and is attributed to impurities in the sample. In an attempt to quantify these impurities, a simple model was employed; if all impurities are assumed to be iron atoms then by taking the accepted value for the magnetic moment of iron [83] of 2.2 μ_b[1], $\mathbf{M}_{sat}$ can then be described as the result of 2×10^{18} iron magnetic moments. For a 0.0306 g sample of Grafoil this corresponds to 40 ppm of iron. This is consistent with other data [84, 22].

With the GTA measurements serving as a benchmark for comparison, the two samples of kish were then characterised via the same method. Figure 3.5 shows the dramatic effect washing has on the magnetism of the kish.

[1] $\mu_b = 9.274 \times 10^{-24}$ J T^{-1}

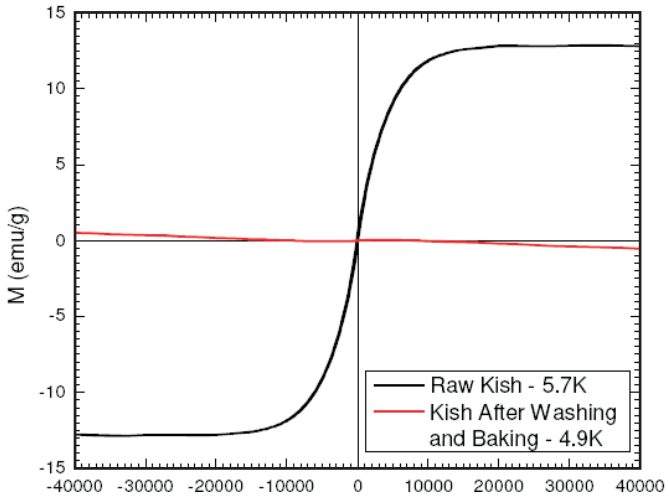

Figure 3.5: The effect of the impurities is apparent in the unwashed kish, as they completely dominate the intrinsic diamagnetism of the graphite. $\mathbf{M}_{sat}$ for the unwashed kish is 13 emu/g.

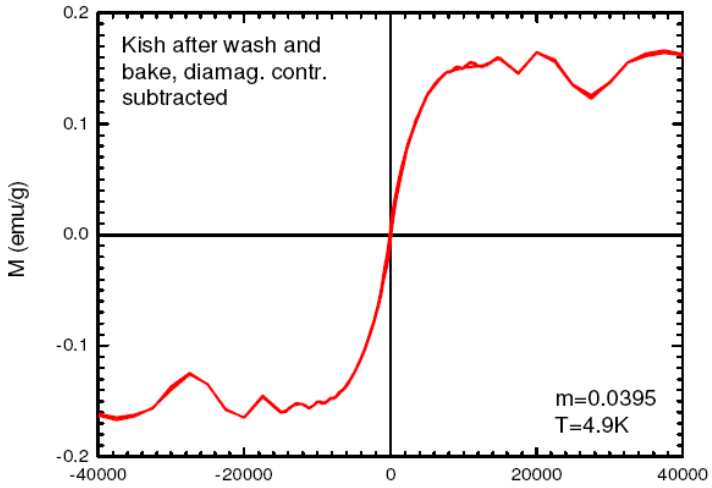

Figure 3.6: Removing the diamagnetic contribution from the washed kish signal reveals similar behaviour as seen in Grafoil, for a similar mass of sample, m = 0.0395 g. $\mathbf{M}_{sat}$ for the washed kish was 0.17 emu/g

The uncorrected magnetisation measurements shown in figure 3.5, clearly show that unwashed kish has a high level of impurities as evidenced by the fact that the ferromagnetic contribution from the impurities completely mask any diamagnetic contribution from the graphite. The $\mathbf{M}_{sat}$ values for the unwashed kish was 13 emu/g. The mass of the unwashed kish was 0.0196 g. Applying the same simple iron model to this data gives an estimate of *14000* ppm for the impurity concentration.

The data in figure 3.5 also shows that acid washing is able to remove a significant fraction of the kish impurities, allowing for the graphite diamagnetism to be recovered. Figure 3.6 shows the ferromagnetic contribution that can be seen once this diamagnetic contribution is then removed, which displays a saturation magnetisation of 0.17 emu/g. Applying the same simple iron impurity model as before results in an estimate of 170 ppm for the impurity concentration.

In line with the work done by Morishita [82], we decided to analyse the samples further using SEM and EDS at the electron microscopy unit at RHUL.

3.1.3 Microanalysis

The electron microscopy unit has a Hitachi S-3000 SEM with a Link ISIS series 300 microanalysis attachment which allows EDS to be performed. This is an excellent tool for sample analysis; with the SEM one can inspect the microscopic morphology of the sample, and by choosing to operate in backscattered mode, impurities stand out brightly against the darker graphite surroundings as a result of the backscattered intensity being proportional to atomic number, Z. This effect can be seen in figure 3.7. Alternatively, one can operate the EDS attachment which works by analysing the X-rays produced by the SEM electrons as they induce transitions in the sample. The spectra that are produced in this way can be compared against a database of characteristic transitions to build up a picture of the elemental composition of the sample. As it is essentially a field of view technique it is possible to

gather compositional information about the sample as a whole, or one can zoom in specifically on an impurity and analyse its make-up.

It should be noted that to obtain a quantitative composition estimate via EDS requires extensive calibration, however using a previous calibration a probable compound for the impurity shown in figure 3.7 was computed; SiO_2. Typically the main impurities in Grafoil are sulphur from the H_2SO_4 intercalant and residual impurities native to the source graphite. Quartz is a commonly found in graphite mined in Shandong, China which accounts for the majority of world graphite production. This same procedure was then applied to washed and unwashed samples of kish. These samples were then subsequently cleaved using scotch tape and then re-inspected.

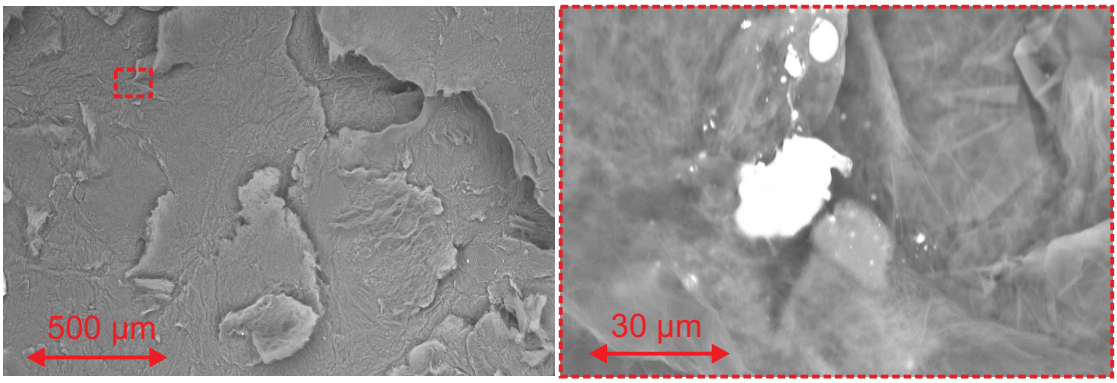

Figure 3.7: SEM micrograph of Grafoil GTA at two magnifications($\times$65 and $\times$1100). The left image shows a wide field overview of the Grafoil surface, whilst the right image is a close up of an impurity grain which contrasts brightly against the background

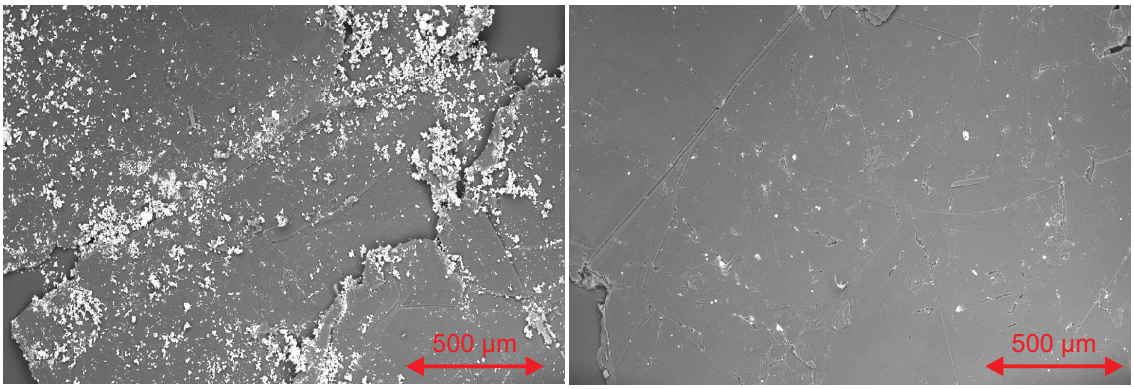

Figure 3.8: Wide-field SEM images of two kish samples. The left image is an image of unwashed kish that is abundant with impurities. The right image is how kish appears when it has been subjected to a washing and baking procedure.

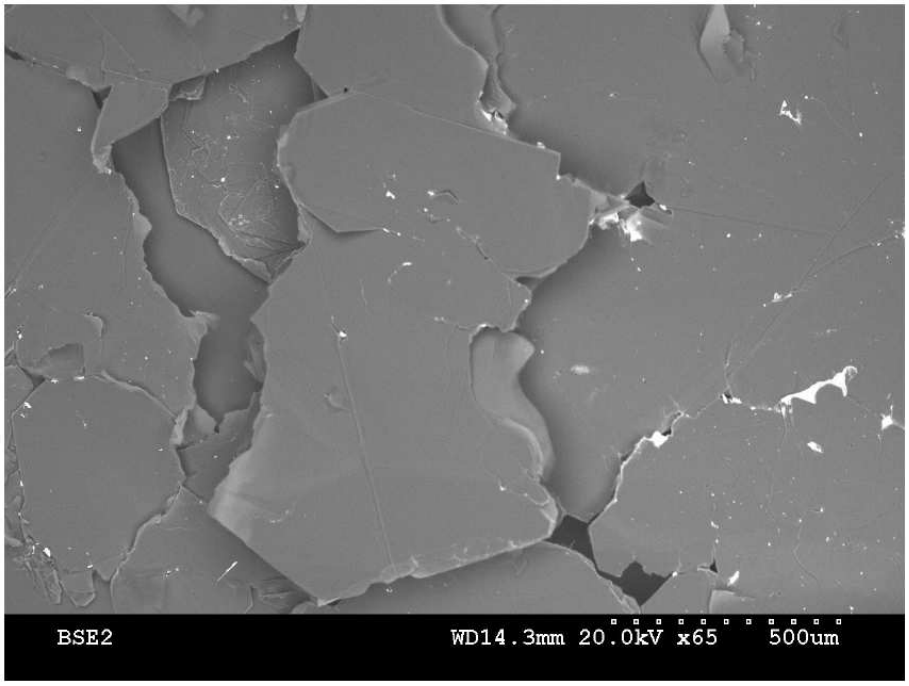

Figure 3.9: SEM of a piece of washed kish that had been cleaved to reveal the inner surface. A similar micrograph of cleaved unwashed kish showed strikingly similar results: large flat surfaces dotted with very small impurity grains about 5 μm in diamter which according to EDS were composed primarily of aluminium, oxygen, magnesium and iron.

Using the EDS attachment to inspect the impurities of the unwashed kish which can be seen in figure 3.8 reveals that they are composed primarily of calcium, magnesium and iron which are all common by-products of steel production. The same figure also demonstrates the effectiveness of the acid wash/heat treatment at removing these impurities from the kish although some grains are still visible dotted about the surface. EDS examination of these impurity grains shows that the acid wash has likely caused the formation of iron (II) chloride, which could have been removed by a higher bake-out temperature or by washing with tetrahydrofuran (THF) which solvates $FeCl_2$ readily.

Cleaving both the kish and unwashed kish with scotch tape produces images such as the one shown in figure 3.9, where the large flat faces are indicative of the crystalline character of kish. Impurities are still clearly visible however, which EDS reveals are mostly aluminium, oxygen, magnesium and iron. The fact that the EDS could not detect a chlorine signature in figure 3.9 suggests that the acid wash is unable to penetrate into the graphite to remove impurities, and this likely contributes to the greater ferro-magnetism seen in the magnetisation measurements.

The SEM images presented here do not give any firm quantitative estimates on mean crystallite size, it does however give strong qualitative evidence of the high crystalline character of kish graphite, in particular the cleaving which reveal large flat planes devoid of many features. Unfortunately, magnetisation and EDS measurements raised questions about the purity of the kish as a starting material. This issue of purity has precluded the use of kish in many research and industrial applications, although some researchers [85] have managed to obtain high purity kish by treatment at high temperatures (>2400 ° C) in a halogen gas flow. Such a procedure is considered to be exceedingly difficult and specialised.

Following these measurements, another potential starting material was sourced; a high quality natural flake from Madagascar courtesy of Dr. Chris Howard, who

had received a sample from Graphit Kropfmehl AG. The kish graphite was not completely ruled out at this point, but as discussed in section 3.2.5 the kish would eventually be dismissed completely based on its apparent reluctance to exfoliate from $K(NH_3)_x\ C_y$ compounds.

3.1.4 Madagascan Flake Graphite

The new Madagascan flake material, as shown in figure 3.10 was composed of flakes with a very uniform size distribution; the flakes are rarely larger than 3 mm or smaller than 0.5 mm, with the majority being 1 - 2 mm in diameter. Using a micrometer we measured the thickness to typically be 40 - 50 μm.

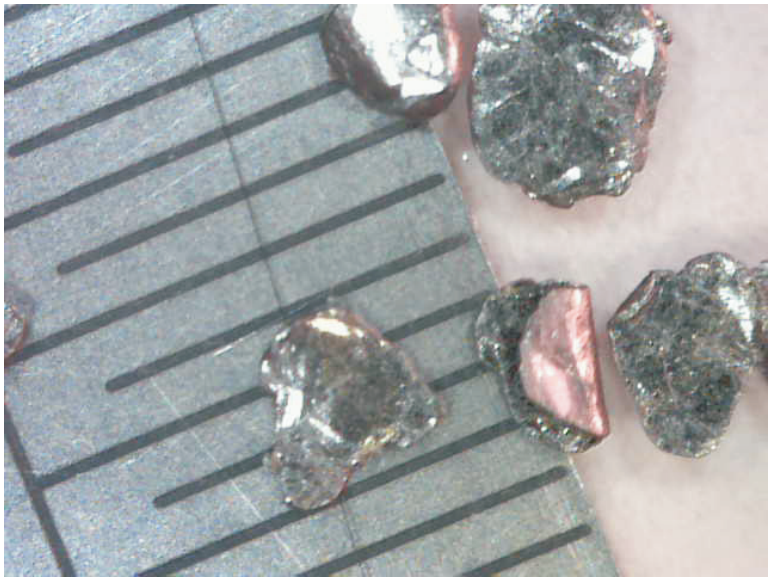

Figure 3.10: Photograph taken with a USB microscope showing a small collection of Madagascan flake graphite. The ruler divisions are 0.5 mm for scale

As was the case with the kish graphite, gaining a quantitative estimate of the crystallite size in the highly crystalline Madagascan samples is not possible using the powder X-ray characterisation methods discussed in section 4.1. In the case

of Madagascan flake we were simply unable to obtain any sort of $(hk0)$ reflection to perform analysis upon. The fact that a (110) peak was obtained in a sample of HOPG gives indirect evidence that it is composed of a myriad of smaller crystallites, such that the powder condition can be satisfied. In the case of the Madagascan flake however, it is presumably composed of much larger crystals so it does not satisfy this powder condition. Further indirect evidence of this was obtained when a sample of the Madagascan flake was placed onto a single crystal diffractometer with the resulting patterns shown in figure 3.11. Given that the beam diameter is 0.5 mm, the fact that the $(hk0)$ scan results in a pattern where only one single crystal is visible suggests that laterally, the crystal size is comparable to the beam size. The $(h0l)$ and $(0kl)$ scans, suggest that the flake is made up of an agglomeration of crystals with a few different orientations, which can be seen in the mosaic smearing of the peaks.

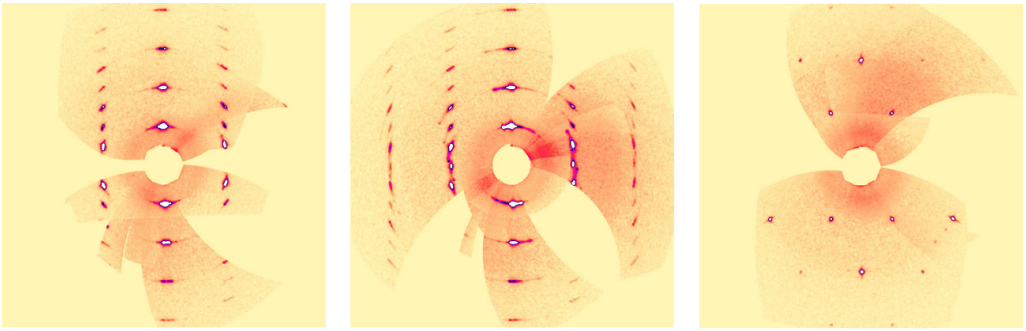

Figure 3.11: $(h0l)$, $(0kl)$ and $(hk0)$ single crystal diffractograms of the Madagascan flake. There are hints of other smaller crystallites in the beam however. Scans were performed by Dr. Dan Porter.

Further characterisations were done using optical microscopy. Comparing the micrographs of HOPG and Madagascan flake that are shown in figures 3.12 and 3.13 suggests that the Madagascan flake is the more crystalline material. HOPG displays a geater density of lined structures and features which are assumed to be defects and grain boundaries. The large, flat, mirror-like facets of the Madagascan

flake are thus taken as qualitative evidence of its crystallinity.

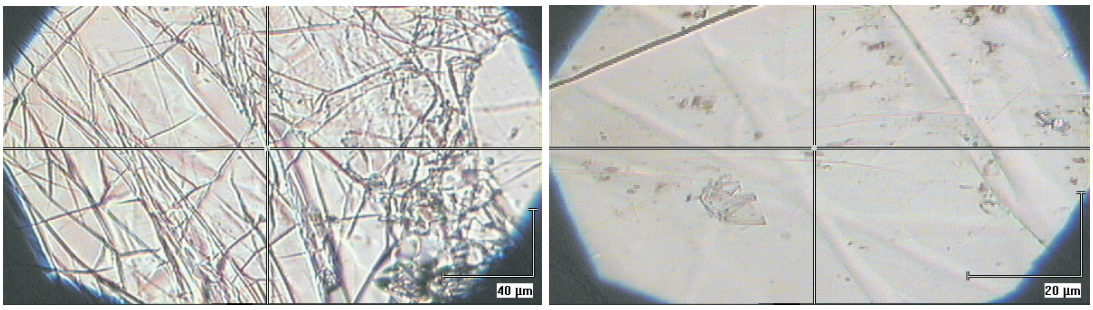

Figure 3.12: Optical micrographs of cleaved HOPG at ×25 (left) and ×50 (right) magnification.

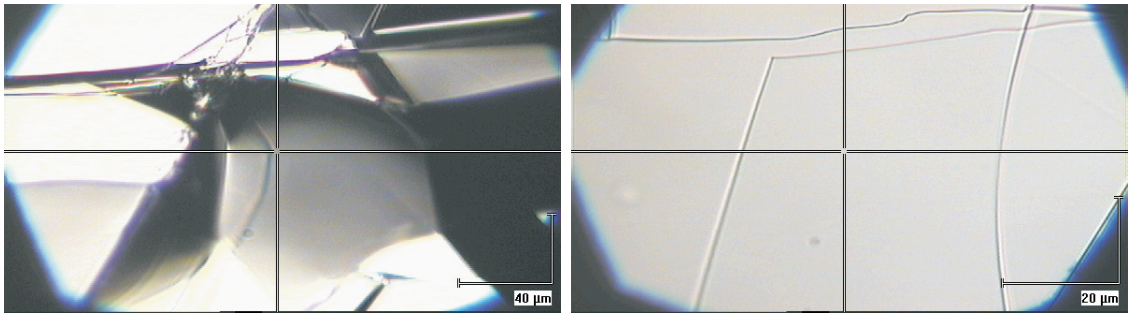

Figure 3.13: Optical micrographs of cleaved Madagascan flake at ×25 (left) and ×50 (right) magnification.

Finally, direct quantitative measurement of the Madagasscan flake purity was performed. Contact was made with Dr. Nathalie Grassineau of RHUL Earth Sciences who agreed to perform elemental analyses on some of our samples, including the Madagascan flake. The results of these measurements are discussed in greater detail in section 4.3 along with the elemental analyses of other samples. To summarise however, it was found that Madagascan flake contained impurities at a comparable level to Grafoil. Convinced of its crystallinity and purity, we decided to proceed with Madagascan flake as a source material.

3.2 Sample Intercalation

With the source graphite selected, the next stage was to begin intercalating and exfoliating samples. This stage of the project made use of the facilities in the CMMP lab at UCL [86]. The Argon glove boxes, fume hoods, furnaces and ammonia gas handling systems were all vital to this project.

3.2.1 Choice of Intercalant

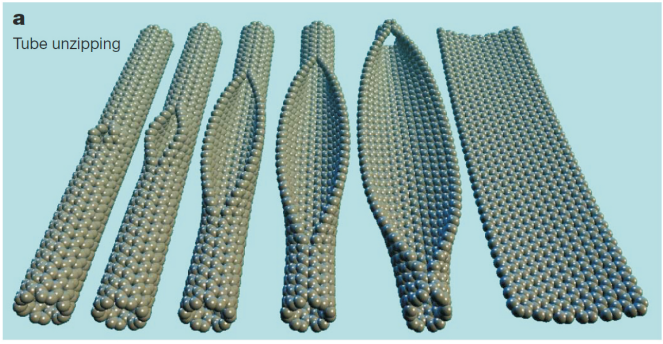

Figure 3.14: Figure taken from [87] showing the unzipping of a carbon nanotube to form a graphene nanoribbon. Note how the process is able to start at the centre of the nanotube and not at the edges. The process is general to graphitic materials, and strong oxidising agents are known to cause cracks and defect formation in the basal planes of graphite [88]

In order to produce a substrate, an intercalant is needed to drive the exfoliation process. Dr. Mark Ellerby and Prof. Neal Skipper made the suggestion to use reagents other than the HNO_3 or H_2SO_4 that are typically used in the production of Grafoil and ZYX. The reason for this is that strong acids can cause undesired functionalisation of the graphite host. Indeed, strong oxidising agents like HNO_3 are known to be able to directly attack the usually inert basal planes of a graphitic material in a process called "unzipping" [87, 89] which is shown in figure 3.14. Such reactions could feasibly introduce unnecessary inhomogeneities in the finished

substrate as even graphite monolayer step edges are considered undesirable. As an alternative they suggested using a potassium-ammonia compound for exfoliation.

The potassium-ammonia graphite compound, $K(NH_3)_x\ C_y$ is made in two steps as ammonia will not spontaneously intercalate. First a potassium compound, KC_y is made. This is then exposed to liquid or gaseous ammonia. With the aid of the already intercalated potassium, the ammonia can enter the intercalant layer to form complexes with the potassium as shown in figure 3.15.

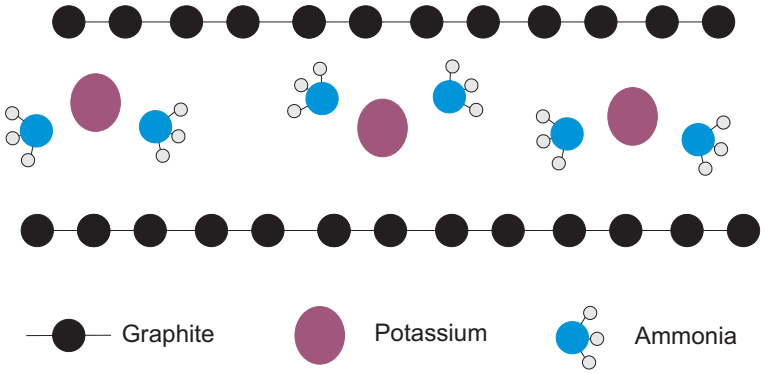

Figure 3.15: Simple schematic showing the ammonia forming complexes around the potassium ions in the intercalant layer of $K(NH_3)_x\ C_y$. This intercalant layer behaves as a 2D metal-ammonia solution [90],[91].

Interestingly, if a K-GIC such as KC_{24} is ammoniated using gaseous ammonia, the number, x, of NH_3 molecules to every potassium in the intercalant layer does not depend linearly on the intercalating ammonia pressure, P_{NH_3}. As can be seen from figure 3.16, x increases in a stepped manner up to a pressure of 1 atm. When the ammonia pressure has reached 9 atm, the amount of ammonia in the intercalant layer saturates with approximately 4.5 NH_3 molecules to every potassium ion. Furthermore, if the gaseous ammonia is removed, the GIC never fully de-intercalates; at least one NH_3 molecule per potassium will remain in the intercalant layer even at zero pressure.

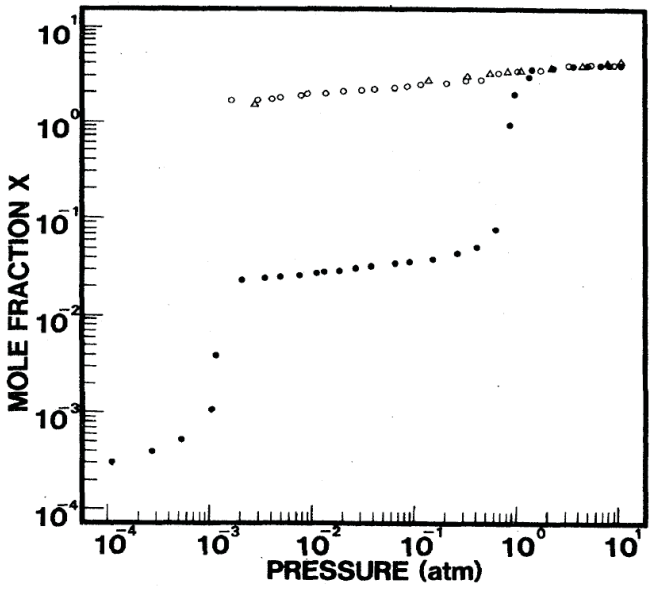

Figure 3.16: The mole fraction, x of $K(NH_3)_x\ C_y$ as a function of applied ammonia pressure. The solid points indicate intercalation, whilst open points are obtained through de-intercalation. Figure taken from [76].

It is interesting to note that KC_y does not exfoliate when heated. Instead it simply de-intercalates, going through progressively higher staging and decreasing in relative potassium concentration until no potassium remains [45]. It is therefore thought that just as the $K(NH_3)_x\ C_y$ intercalates in two steps, so it de-intercalates in two steps, with the ammonia de-intercalation being the driving force of the exfoliation process. This is supported by our observations that small amounts of exfoliation of $K(NH_3)_x\ C_y$ can be seen at temperatures as low as 180° C, but indicators[2] that the potassium has been released do not occur until higher temperatures. By using $K(NH_3)_x\ C_y$ we have hopefully circumvented the issue of undesired functionalisation as neither potassium nor ammonia are capable of unzipping the graphite lattice in the same manner that HNO_3 is able to.

[2]There are a couple of signs that indicate that potassium has left the graphite; the graphite flakes lose their blueish tinge and also there is the tell-tale formation of a potassium ring towards the flange of the reaction vessel such as the one shown in figure 3.26.

3.2.2 Argon Glove Boxes

Problematically, $K(NH_3)_xC_y$ and its intermediary KC_y are air sensitive, requiring the inert working environment of an argon glove box, such as the one shown in figure 3.17.

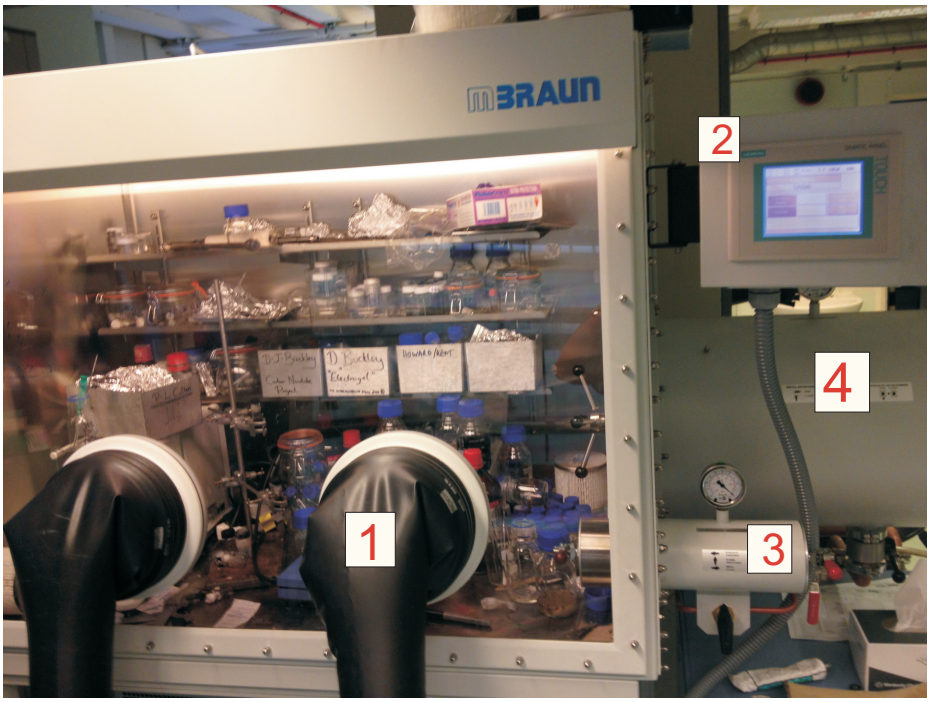

Figure 3.17: Photograph of one the MBraun glovebox that were used in this project. Various components are numbered; 1.) The 2 mm thick Viton® gloves for handling 2.) Glovebox monitoring system 3.) Small port 4) Large port.

The MBraun glove box [92] maintains an inert atmosphere by providing a constant argon overpressure of approximately 10 mbar using a standard gas cylinder. This atmosphere is constantly recycled through a series of scrubbers that remove moisture and oxygen. The status of these scrubbers and the levels of the contamination are monitored through an interactive display. The oxygen and moisture in the glovebox is monitored to 0.1 ppm resolution using a dedicated sensor for each. Sample handling is done via two thick Viton® rubber gloves. Fine manipulation is

difficult but achievable.

To bring items into the glovebox there are two ports (large and small) located on the right hand side. Each port has an airlock with an inner and outer door. A three-way valve is attached to each port to enable evacuation by rotary pump, to flush the port with argon, or to completely seal it. When bringing items in and out of the glove box, a strict protocol is followed; any time the inner port door is to be opened the port must first undergo a minimum of three evacuation-flush cycles to minimise contamination from the outside. It is also important not to transit sealed bottles and containers into the glove box unless it is known they do not contain any reactive gases.

Despite the fact that the glove box typically operates at < 1 ppm of oxygen, it is still possible to observe in real time the formation of an oxide layer on a freshly exposed potassium surface. To counteract this, samples are kept in cleaned Schott® [93] sample bottles in case of a gross breach of glove box integrity. Remnant potassium is often left out in the open to soak up any stray contamination helping to maintain the inert atmosphere. This procedure has allowed GIC samples to be kept for up to two years after manufacture.

3.2.3 $K(NH_3)_x\ C_y$ Intercalation

References [94], [91] and [90] all describe the manufacture and structural characterisation of $K(NH_3)_x\ C_y$ type compounds, however the work of York and Solin [76] in particular has been invaluable in guiding the synthesis and characterisation our own $K(NH_3)_x\ C_y$ compounds. They first discuss the manufacture of a stage-2 KC_{24} compound using the two zone method developed by Herold [95]. *In situ* mass uptake measurements and $(00l)$ X-ray scans were then performed to elucidate how the structure and composition of $K(NH_3)_x\ C_{24}$ changed as a function of applied ammonia pressure. These characterisations are discussed in greater detail in section 3.2.4

in the context of interpreting our own compounds, whilst their synthesis is the basis for our own procedure and is described here.

The usual approach to intercalate potassium is to use the Herold [95] two zone vapour transport method, whereby the graphite host is held fixed at some higher temperature, T_g in one zone and the potassium is held at a lower temperature, T_i in the other zone, with the two zones connected via some tube. The temperature difference, T_g -T_i then determines the stage of the sample. During the course of this project we found that we can manufacture various stages of KC_y using a modified 'hot single zone' method in which the desired stage can be achieved by simple stoichiometry calculation and subsequent annealing. Using this method, which is shown in figure 3.18 stage 2, 3 and 4 compounds have been manufactured and confirmed via x-rays.

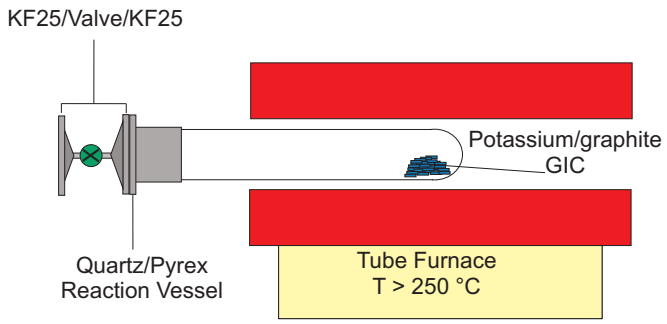

Figure 3.18: Schematic of the 'hot single zone' method that was used to intercalate potassium. As will be discussed in section 3.2.5, the quartz/pyrex tube sealed with a valve would eventually be replaced by torch-sealed pyrex ampoules.

To begin our intercalation process, a quantity of the Madagascan flake graphite is taken and out-gassed for at least 12 hours at 500 °C under vacuum (10^{-5} mbar) to remove moisture and other common contaminants. Typically this is done in large

batches to provide for many GIC productions and then kept in a bottle in the argon glove box until use. Typically intercalations were performed in 'batches' and each comprised approximately 1 - 2 g of graphite. The mass of each batch of graphite was weighed to a precision of ± 1 mg inside the glove box and then placed in the reaction vessel. Potassium intercalations were performed in pyrex or quartz tubes with stainless KF fittings, though we eventually upgraded to sealable pyrex ampoules as shall be discussed. The required potassium is then weighed in accordance with table 3.1 and placed into the reaction vessel along with the graphite.

Table 3.1: Staging formula

Desired Stage	Stoichiometric Formula	Relative mass of K required
1	KC_8	0.4115
2	KC_{24}	0.1372
3	KC_{36}	0.0914
4	KC_{48}	0.0686
5	KC_{60}	0.0549
6	KC_{72}	0.0457
7	KC_{84}	0.0392
8	KC_{96}	0.0343

Thus, to make a stage-2 compound all that is required is to place 0.1372 g of potassium with 1 g of graphite. Due to the high reactivity of potassium it is necessary to perform all handling within a glove box, however the potassium still tarnishes visibly even within the inert argon atmosphere. To compensate for these oxidative losses a 10 % excess of potassium is then added to the calculated amounts of table 3.1, so for KC_{24} the relative potassium mass that is weighed out is actually 0.151 g. The reaction vessel is then sealed with a valved top as shown in figure 3.18, taken out of the glove box and attached to a turbo-pump which is used to slowly evacuate the argon from the reaction vessel to 10^{-5} mbar. Once a sufficient vacuum is achieved, the valve is closed and the reaction vessel is inserted into a tube furnace

preset to 250 °C to start the intercalation process. The vessel is routinely removed and the contents inspected and agitated to promote uniformity before being placed back into the furnace. Inspection by eye is a good indicator of homogenisation as stage-1 KC_8 compounds have a characteristic gold colour whilst stage-2 KC_{24} is a brilliant blue. Higher stages are harder to infer by eye, but they tend to appear as darker blue and dull greys. Figure 3.19 presents pictures that were taken at various times during an intercalation, showing how the sample gradually homogenises in stage. Once the flakes display a uniform colour they are subjected to a 24 hour anneal, and slowly cooled. The vessel is then removed to the glove box where the contents are then stored in cleaned Schott DURAN® [93] sample bottles. At this point we would often confirm the stage fidelity of our samples using X-rays, and this is discussed in the next section. Following this, the newly manufactured KC_y compounds are now ready to be ammoniated.

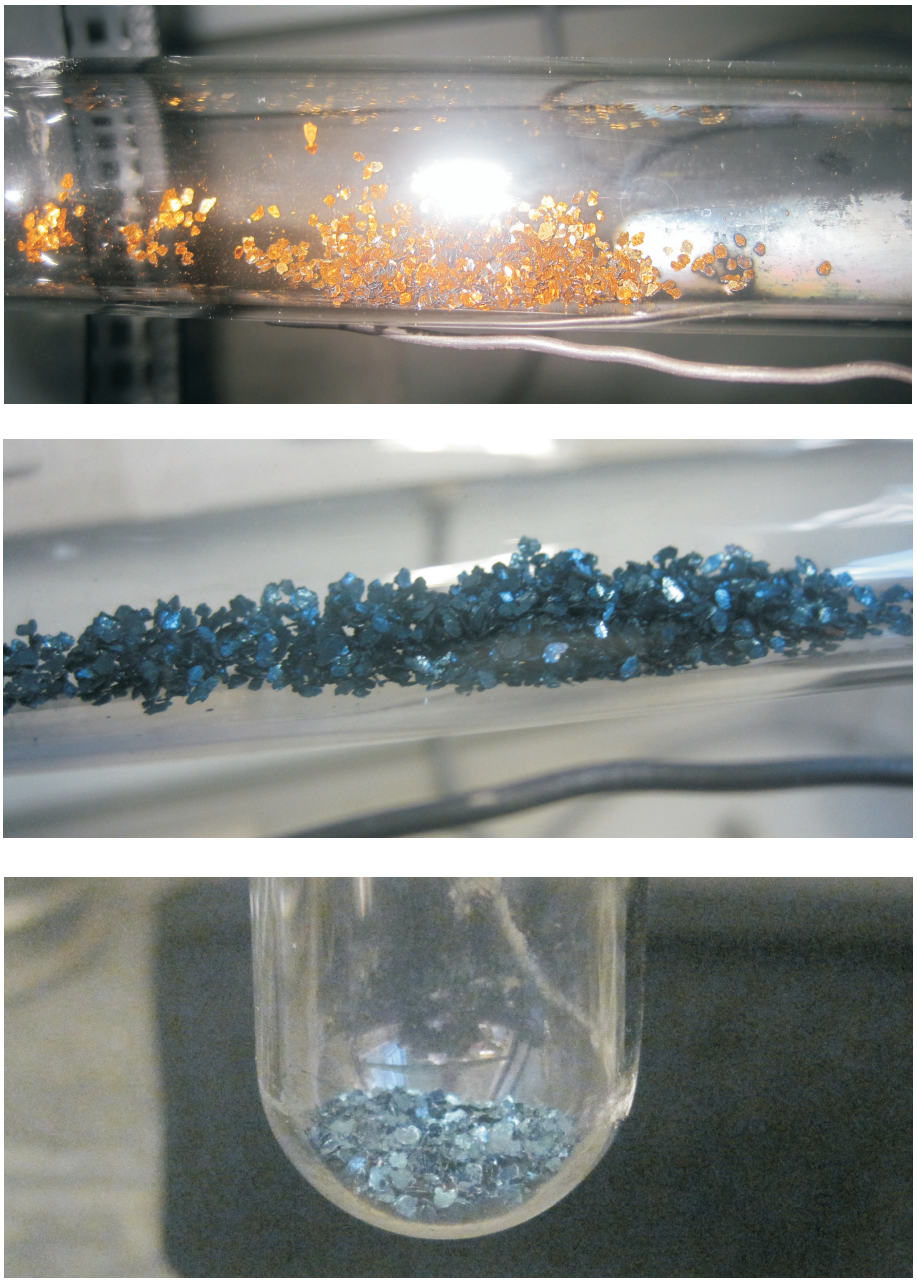

Figure 3.19: Top: Gold coloured flakes characteristic of stage-1 KC_8. Middle: With continued reaction, the potassium propagates thorughout the graphite gradually homogenising, clearly visible are the characteristic metallic blues of stage-2 KC_{24}, however the dark blue and greys of other flakes indicate further homogenisation is needed. Bottom: fully homogenised KC_{24}.

To ammoniate, the KC_y samples are placed into a flanged glass vessel and sealed with a valved top, removed from the glove box and attached to an ammonia gas handling system, a schematic of which is shown in figure 3.20. The whole gas handling system is then pre-evacuated down using a turbo-pump, before slowly cracking the valve on the reaction vessel to remove the glove box argon. Once sufficient vacuum (10^{-5} mbar) is achieved, the pump is closed off and ammonia is bled *slowly* from the reservoir into the rest of the gas handling system until a pressure of 1.5 bar is reached[3]. The start of the ammonia intercalation is immediately apparent as it is exothermic causing the reaction vessel to warm up noticeably near the GIC flakes. For very large batches ($>$ 2 g) the vessel is just about too hot to touch. It was usual to leave the ammoniation for half an hour or so, and on returning the ammonia pressure would again be topped up to 1.5 bar to replace pressure lost due to ammonia absorption into the GIC. The sample would be periodically agitated and then left overnight to produce a homogeneous sample. Inspection by eye is still useful at this point. Certainly, when ammoniating stage-2 KC_{24} compounds the stage-2 $K(NH_3)_x$ C_{24} compound still retains the same blue colour of the original KC_{24}, however ammoniation causes it to lose its metallic lustre somewhat. Again higher stages are harder to see by eye, but colour homogeneity is still a useful rough indicator of stage fidelity.

[3]This was mainly out of convenience; the reaction vessel is attached to the ammonia GHS via KF-25 fittings. As ammonia is toxic, we were unwilling to test the overpressure capabilities of these fittings despite the added fail-safe of a fume hood.

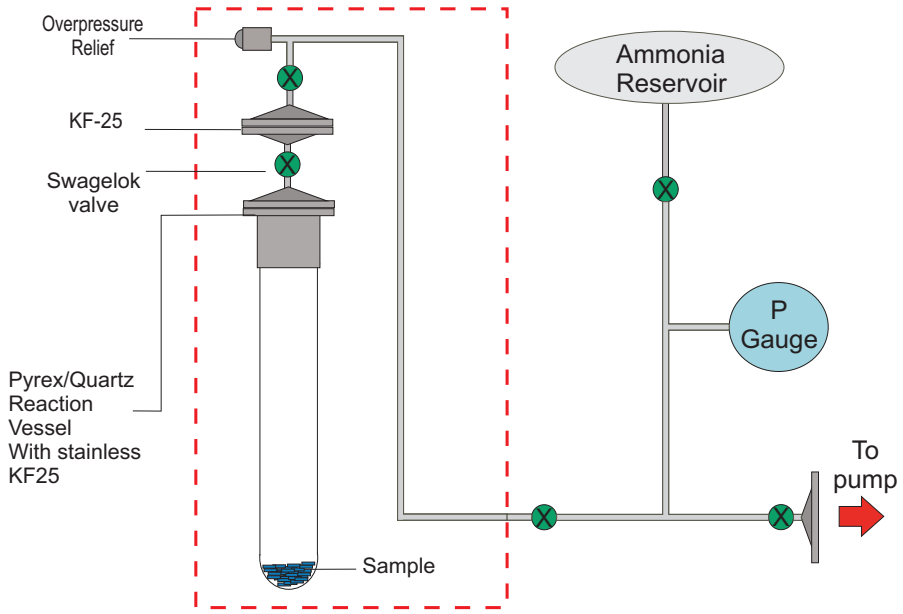

Figure 3.20: Schematic of the ammonia gas handling system, which includes an attached reaction vessel. The red-dashed box represents the part of the system that is kept within a fume hood in case of an ammonia leak.

After spending 16 - 20 hours ammoniating, the ammonia atmosphere is removed by immersing the reservoir in liquid nitrogen. Care must be taken at this point to cryo-pump slowly, as reducing the pressure too quickly can cause the sample to exfoliate. With the majority of the ammonia removed, the reservoir is again sealed and a turbo-pump used to pump away any remnant ammonia pressure. All valves are then closed, and the reaction vessel which now contains $K(NH_3)_x\ C_y$ compound is brought into the glove box where the sample is decanted into another Schott DURAN® container for storage. The compound is now ready for inspection via X-rays or for exfoliation.

3.2.4 Sample Staging

It was customary to check the staging at each step of the intercalation, measuring both KC_y and $K(NH_3)_x$ C_y samples. The introduction of regularly staged intercalant layers changes the lattice parameter along the c-axis. This can be measured via X-rays using the positions of the $(00l)$ reflections from the sample. Both KC_y and $K(NH_3)_x$ C_y are air sensitive, so any diffraction measurement must necessarily take place in an inert environment. There are many sophisticated ways of doing this, however Dr. Chris Howard has an ingenious solution which is to take a few of the GIC flakes and place them on a glass microscope slide, exposure to air is prevented by sealing over the flakes with Kapton tape. Samples will eventually degrade with this method, but it prevents exposure for long enough to perform $(00l)$ scans. These scans are presented in figure 3.21.

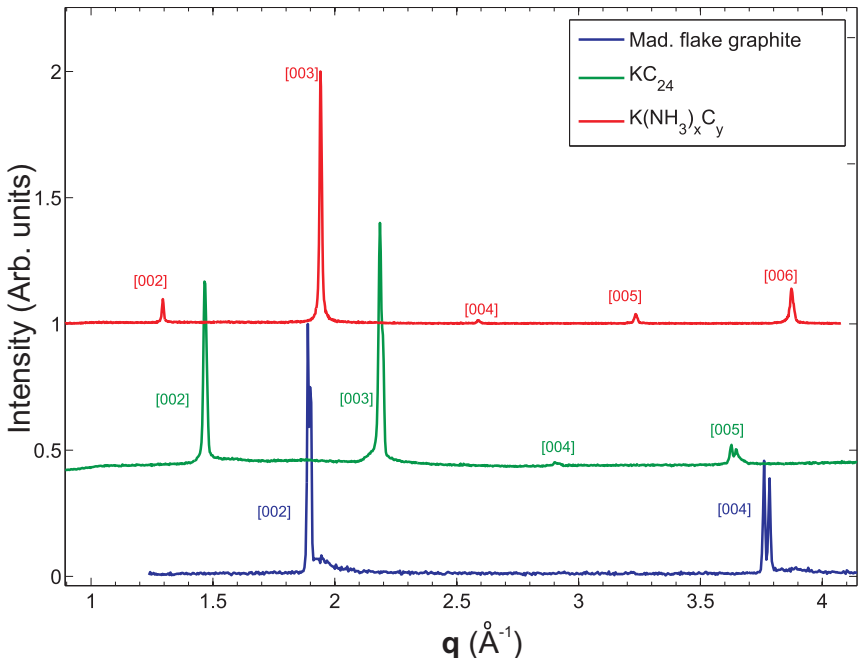

Figure 3.21: Comparison of $(00l)$ scans of Madagascan flake, KC_{24} and $K(NH_3)_x$ C_{24}. As is discussed in the text it is often useful to transform the x-axis from 2θ into q

By converting to $q = 4\pi \sin(\theta)/\lambda$, comparison between instruments of different wavelengths[4] is simple and Bragg's law becomes:

$$d = \frac{2\pi n}{q}, \tag{3.1}$$

where d is the lattice parameter and n is the order of the reflection. If the GIC is well staged, then d can be used to gauge the staging of the sample. Stage mixtures are described the theory of Hendricks and Teller (HT -model) [96]. Analysis through the HT-model requires long detailed $(00l)$ scans however, which simply cannot be achieved using our method of Kapton tape to prevent sample air exposure.

Sample	Lattice parameter (Å)	Literature (Å)
Mad. Flake	6.66 ± 0.02	6.71[41]
KC_{24}	8.63 ± 0.03	8.75[44]
$K(NH_3)_xC_{24}$	9.72 ± 0.02	9.8 - 9.9[76]

Table 3.2: As measured and literature lattice parameters. There is good agreement, however, there appears to be a small systematic error causing the measured lattice parameter to be consistently less than the literature value. This can be attributed to the finite thickness of the sample [97]. Other sources of discrepancy are discussed in the text.

The measured lattice parameter of 9.72 Å for our stage-2 $K(NH_3)_xC_{24}$ is consistent with a graphite-graphite-intercalant stack comprised of one 3.33 Å thick graphite to graphite layer and one 6.39 Å thick intercalant layer. It is interesting to compare this to the work of York and Solin [76], who performed *in situ* $(00l)$ scans of KC_y whilst varying the ammoniation pressure. These measurements, presented

[4]Radiation from both Copper and Molybdenum tubes were used, Cu-K_α and Mo-K_α.

in figure 3.2.4, show that the presence of ammonia initiates a stage transformation from stage-2 to a mixture of stage-1 and 2 compounds. At low ammonia pressures the stage-2 dominates, whilst at high pressure the compound is entirely stage-1. Increasing the pressure also correlates with an increased intercalant layer thickness. In the case of our samples which were ammoniated at 1.5 bar this would correspond to an intercalant layer thickness of approximately 6.5 Å. Our value of 6.38 Å can be attributed to the fact that our samples were not measured *in situ*, but instead after complete removal from the reaction vessel and thus in the complete absence of any ammonia pressure. It is interesting to compare our samples to the Bromine-graphite residue compounds that were discussed in sections 2.1 and 2.2. Where the removal of the Bromine vapour pressure results in the Bromine desorbing until a stable stochiometry is reached, the work of York and Solin suggests the similar, yet distinct behaviour; as the ammonia vapour is decreased, the potassium concentration remains unchanged but the GIC will gradually desorb ammonia. As can be seen by extrapolating back to zero pressure in figure 3.16, the lowest stable stoichiometry appears to to be one ammonia molecule per potassium centre. Unlike the Bromine residue compounds however, the staging phenomenon is still very much apparent.

Rudimentary measurement of the masses of our samples before and after ammoniation indicate that there are approximately 3 - 5 NH_3 molecules per potassium, though some of this weight can be attributed to adsorption of ammonia onto the flake surface.

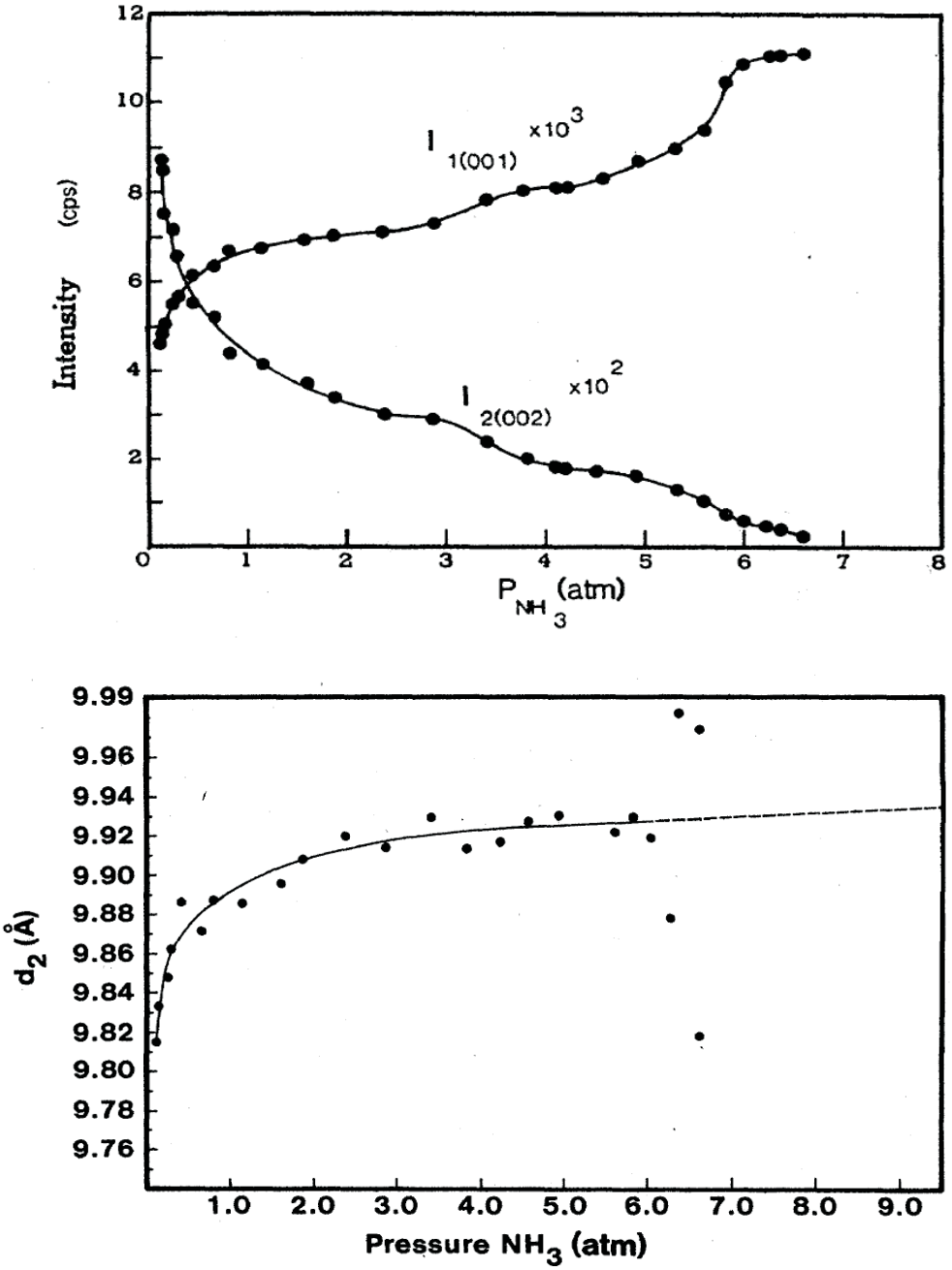

Figure 3.22: Reproduced from [76]. Variation in the intensities of $(00l)$ reflections associated with stage-1 and stage-2 components as a function of applied ammonia pressure. It is suspected that exfoliation by rapidly reducing the pressure occurs due to the re-staging process occurring too quickly. The bottom graph shows how the lattice parameter of the stage-2 compound is also dependent on applied ammonia pressure. All measurements are done *in situ*.

3.2.5 Discussion

The majority of the GIC batches that have been made in this project have been stage-2 $K(NH_3)_x$ C_{24}, made through the ammoniation of a stage-2 KC_{24} precursor. The question was eventually raised as to whether the final staging of the $K(NH_3)_x$ C_y compound had any effect on the exfoliation process. Higher stage GICs have a lower intercalant concentration, so a reasonable supposition would be that high-stage GICs exfoliate to a lesser extent than low-stage GICs. Table 3.3 lists all $K(NH_3)_x$ C_y batches that were made in the course of this project alongside the stoichiometry of the KC_y precursor.

Batch Number	KC_y precursor	$K(NH_3)_xC_y$ Final staging
2	KC_{24}	2
3	KC_{24}	2
4	KC_{24}	2
5	KC_{24}	2
6	KC_{24}	2
7	KC_{24}	2
8	KC_{36}	2
9	KC_{36}	3
10	KC_{24}	fail
11	KC_{24}	2
12	KC_{24}	2
13	KC_{36}	fail
14	KC_{36}	3
15	KC_{60}	4
16	KC_{96}	unknown
17	KC_{36}	3

Table 3.3: Summary of GIC batches.

All the batches shown in this table have been manufactured using the Madagascan flake as a source material. Other intercalations were performed, but they are not shown. In particular, several attempts were made to intercalate both washed

and unwashed flakes of kish graphite. In both cases, no evidence of intercalation could be seen in their $(00l)$ scans, and more importantly, none of these kish GIC attempts underwent exfoliation, even when subjected to very high temperatures. This observation meant that kish graphite was completely ruled out as a source material for the substrate. It is suspected that any potential host graphite must be reasonably pure in order to intercalate a species such as potassium which likely reacts preferentially with the impurities, rather than the graphite host. It should be noted however, that kish can be intercalated with HNO_3/H_2SO_4 and subsequently exfoliated, though no prototype substrates were made using this method.

As can be seen from the table, the $K(NH_3)_x$ C_y compounds of batches 8, 9, 14, 15 and 16 were manufactured from precursor GICs with a stoichiometry other than KC_{24}. The premise is that making a higher staged KC_y precursor in accordance with the empirical formulae of table 3.1, should then result in a higher stage in the final ammoniated compound.

Batch 8 was the first attempt at making KC_{36} which should have been stage-3 although ultimately, on ammoniation the final compound was still only stage-2. The conclusion was that the potassium intercalation had not homogenised properly and it was thought that higher temperatures than the usual 250 °C would be needed to correct this.

Batches 9 and 14 were then re-attempts at making a stage-3 compound based on the ammoniation of a KC_{36} precursor. The diffraction patterns shown in figure 3.23 show that the batch 9 and 14 $K(NH_3)_x$ C_{36} compounds display $(00l)$ reflections that are consistent with a 13.1 ± 0.03 Å unit cell. Assuming the $K(NH_3)$ intercalant layer thickness is 6.4 Å as before, this then implies batch 9 and batch 14 are both stage-3. Batch 15 was based on the ammoniation of a KC_{60} compound which should be stage-5 according to table 3.1, however scans performed on the batch 15 KC_{60} precursor indicate that it was likely composed of a stage-4/stage-5 mixture. Upon

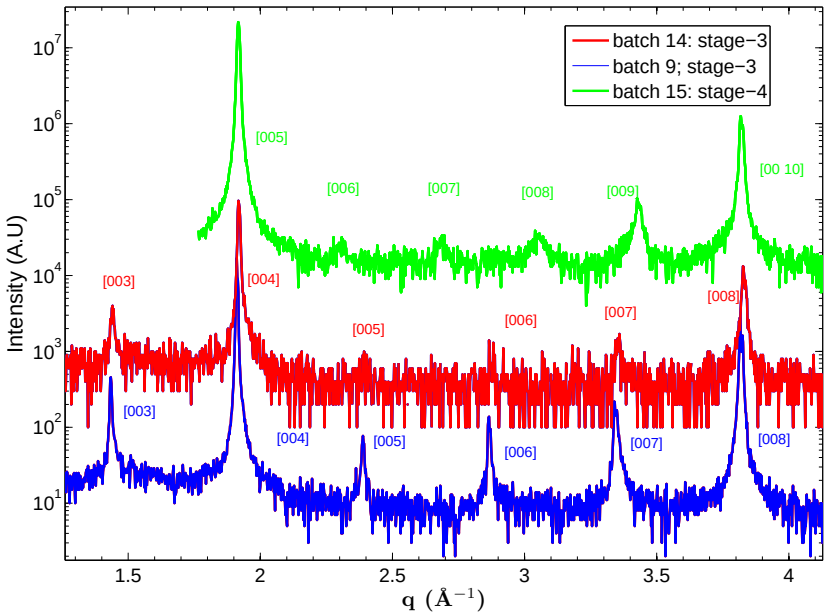

Figure 3.23: $(00l)$ scans of the final $K(NH_3)_xC_y$ compounds of batch 9, 14 and 15. The staging of batch 16 was never characterised. The reflection labels are consistent with stage-3 in the case of batches 9 and 14, whilst the labelling for batch 15 is consistent with stage-4. The y-axis has been adjusted and is logarithmic for clarity. The decreased signal-to-noise of the batch 14 compared to batch 9 can be attributed to a smaller receiving slit width

ammoniation, the final product can be seen from its $(00l)$ reflections to have a c-axis unit cell of 16.4 ± 0.08 Å which is consistent with a stage-4 compound.

Batches 14, 15 and 16 and made use of torch-sealed pyrex ampoules rather than the original glass reaction tubes shown in figure 3.18 to intercalate potassium. The procedure remains fundamentally unchanged; the pyrex ampoules are loaded with the requisite potassium and graphite and then sealed with an appropriate O-ring adaptor/valve/KF-25 connection piece. This is then removed from the glove box and pumped down to 10^{-5} mBar. Once base pressure has been reached, an oxy-acetylene torch is used to melt and collapse the neck of the ampoule, thereby

completely entombing the graphite and potassium within. The now-sealed ampoule, such as the one shown in figure 3.24, can then be placed in the furnace to start the intercalation reaction. The absence of KF fittings means that the ampoule can be left in the furnace for longer and at higher temperatures to promote homogeneity within the sample. Once the intercalation is complete, the ampoule is removed from the furnace and carefully cracked open in the glove box and the contents removed. The KC_y is then decanted into the usual glass reaction tube to perform the ammoniation.

Figure 3.24: Pyrex ampoule that has been sealed with an oxy-acetylene torch, and then used to create a KC_y compound.

Despite the success in creating these higher stage compounds, these investigations were discontinued after a search of the literature showed that other workers have found that the GIC staging appears to have no effect on any subsequent exfoliation [98, 99, 66]. For example, Furdin [98] exfoliated samples of graphite that had been intercalated with HNO_3 to stage 3 ,4, 7 and 10. The specific area and the expansion ratio of the exfoliated graphite samples showed no dependence on the stage of the original GIC. Similarly, Inagaki [66] exfoliated both low-stage and residue compounds intercalated with sodium-tetrahydrofuran. The c-axis expansion was the same in both instances.

This is rather counter-intuitive, as there must exist some lowest residue limit of intercalant concentration at which exfoliation will no longer occur. There are no detailed studies on this however, though based on the work of Furdin [98] and Inagaki [66] it seemed reasonable to assume that for the range of stages achieved in our samples at least, no measurable effect on the exfoliation should be expected.

3.3 Sample Exfoliation

With the newly intercalated samples of $K(NH_3)_x\ C_y$ stored away in the glove box, the next step is to exfoliate these samples. To begin, a freshly cleaned reaction vessel is filled with an amount (typically 0.1 - 0.2g) of GIC, and sealed with the usual KF-25/valve/KF-25 connection piece. The vessel is then removed from the glove box, attached to a turbo-pump and the argon slowly pumped away. For the sake of time we typically only pumped down to $< 10^{-3}$ mBar. Once this pressure is reached we then insert the vessel into a furnace at a pre-set temperature, all the whilst actively maintaining vacuum. If the furnace is above some critical temperature (180° C), the exfoliation can be seen instantly in the pressure gauge as the ammonia comes issuing out of the graphite.

A multitude of trial exfoliations were performed which seem to suggest that some element of thermal 'shock' is required to initiate the exfoliation process. Evidence for this is given by the fact that when the tube is inserted into the furnace and then the heating increased progressively, exfoliation often does not take place. It is thought that by progressively heating the GIC, the ammonia intercalant can be driven off with little or no exfoliation being observed. On removal, these GICs would sometimes show signs of being completely degraded and even high and sudden heating could not again initiate exfoliation. In other cases, GICs that had been subjected to a gradual and increasing temperature could still be made to exfoliate

if sudden heating was subsequently applied. The precise conditions governing this process are not known.

Figure 3.25 shows the resultant exfoliated graphite that resulted insertion into a furnace pre-set to 500°C. Unsurprisingly, it was found that sudden heating of GICs at higher temperatures produced greater c-axis expansions than in GICs subjected to sudden heating at lower temperatures.

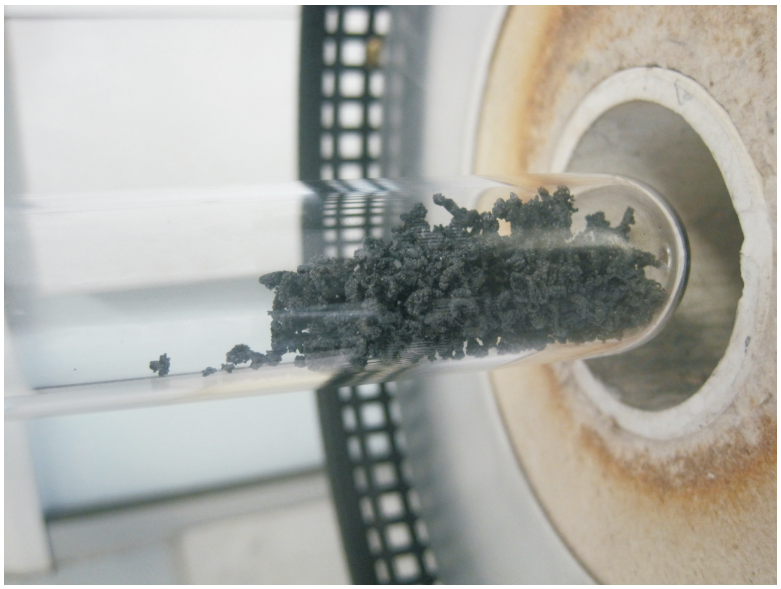

Figure 3.25: Top: An example exfoliation immediately after removing from a furnace pre-set to 500° C.

The exfoliation is then left at this temperature for > 8 hours to ensure that the exfoliation has fully progressed and the majority of the ammonia has been removed. After this time, the temperature is then ramped up to an elevated temperature to drive off any residue intercalants before it is removed from the furnace.

This second heat treatment was the subject of some investigation as it presented some practical issues. Initially we were unsure as to how high a temperature is necessary to remove the potassium intercalant; as the results of section 4.3 show, the

majority of the potassium is removed by heating to 700°C under vacuum, however at least 2000 ppm of potassium remains, though it is believed that ammonia has been completely removed at this point. Further testing, also presented in section 4.3 showed that subjecting the exfoliated samples to 1000°C under vacuum for 24 hours is sufficient to remove effectively all potassium. Most of the exfoliations performed in this project took place in the quartz tube, which in principle can be subjected to 1000°C temperatures quite comfortably, and indeed this was done. Unfortunately, repeated use of the quartz tube for exfoliations lead to degradation of the quartz, which in one case resulted in catastrophic failure. It is thought that at even moderately high temperatures, the normally unreactive quartz is susceptible to attack by the potassium vapour as it deintercalates out of the graphite. For this reason, the second heat treatment temperature is limited to 700°C, and it is assumed that any remnant potassium has negligible effect on adsorption or diffraction measurements. Even when limiting the heat treatment temperature to 700°C, the quartz tube could still be seen to progressively degrade, and on several occasions it was necessary for this tube to be repaired by the glass blower at UCL. The quartz tube was eventually decommissioned, and a stainless steel (grade 314) tube made by the workshop at RHUL, which was then used to perform exfoliations.

Furthermore, this second heat treatment also posed the problem of secondary exfoliation. If the furnace is allowed to increase to 700°C at its maximum ramp rate of 20 °C/min, then the sample would often appear to undergo further exfoliation on top of that which had occurred on the initial furnace insertion. Eventually, we found that if the sample is under vacuum at the initial exfoliation temperature for a prolonged period (overnight typically), and then the ramp rate to 700°C is limited to 5°C/min, it was seen visually that the graphite underwent minimal further exfoliation. For the best results ramp rates of < 1°C/min were eventually adopted.

When the exfoliation is completed, the reaction vessel is removed from the fur-

nace and allowed to cool before removing the exfoliated contents, which are now ready to be pressed into a foil.

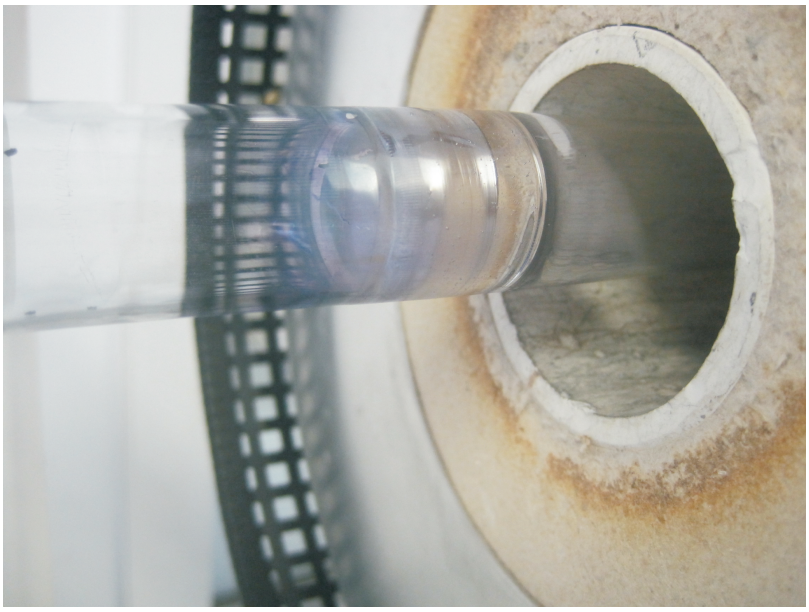

Figure 3.26: Photograph showing potassium condensing/depositing a the nearest cold point outside the furnace. Hints are of this are first seen at around 300 ° C as the first potassium starts to come off, however 500 ° C was necessary to achieve visible condensation and as will be discussed in section 4.3, 1000 ° C was required for complete removal.

3.4 Foil Pressing

The exfoliated graphite can be pressed into a foil using a standard laboratory pellet die and hydraulic press, such as the one that is shown in figure 3.27. The exfoliated sample is placed into the die as indicated in the figure, and the whole assembly placed under a hydraulic press. The piston of the hydraulic press is 8 cm in diameter, which is driven by a manual hand pump with a gauge which measures the pressure of the hydraulic fluid. This means that for every 10 bar of hydraulic pressure, 7500 N is

exerted at the piston face which then pushes down on the die piston. The diameter of the anvil was 19 mm, this then means that for every 10 bar in the hydraulic pump, the sample experiences 177 bar in the pellet die. With a few exceptions, all foils were compressed with 177 ± 60 bar of pressure. Typically, the mass of exfoliated material that was loaded into the pellet die was 0.1 g. On compression, these produced foils that were typically 300 ± 50 μm in thickness.

The exfoliated graphite is auto-consolidating; it holds together without the aid of binders. Qualitatively, it was found that graphite that had been exfoliated at high temperatures produced a more uniform and structurally stable foil, whilst low temperature exfoliated graphite produced a granular foil that would crumble easily. A comparison of two such foils are shown in figure 3.28. These prototype foils are now ready for characterisation, and this is discussed in the next chapter.

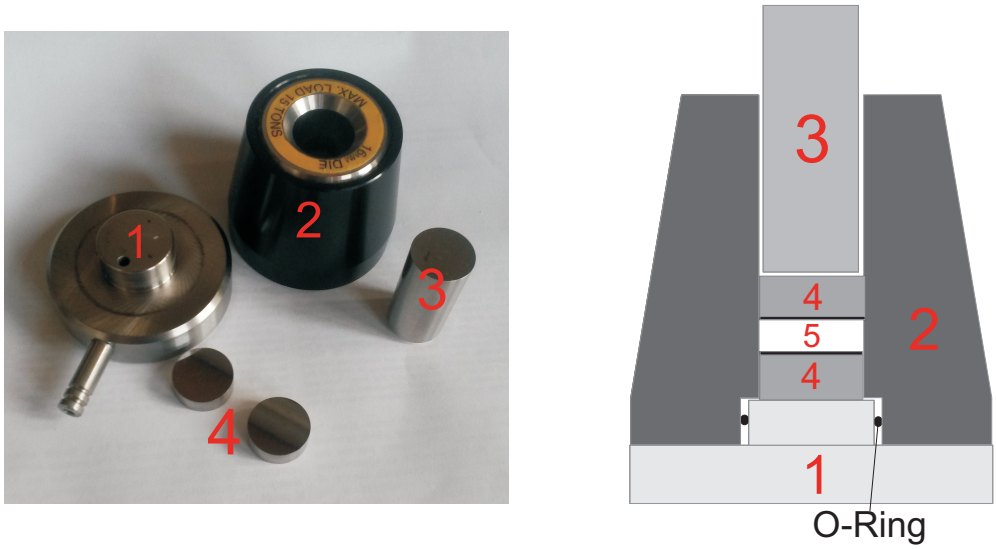

Figure 3.27: Photograph and diagram of operation of the evacuable pellet die that was used to make the substrate foils. The various labels are 1) die base 2) die body 3) die piston 4) optically polished anvils 5) sample space in between anvils with optical surfaces facing each other.

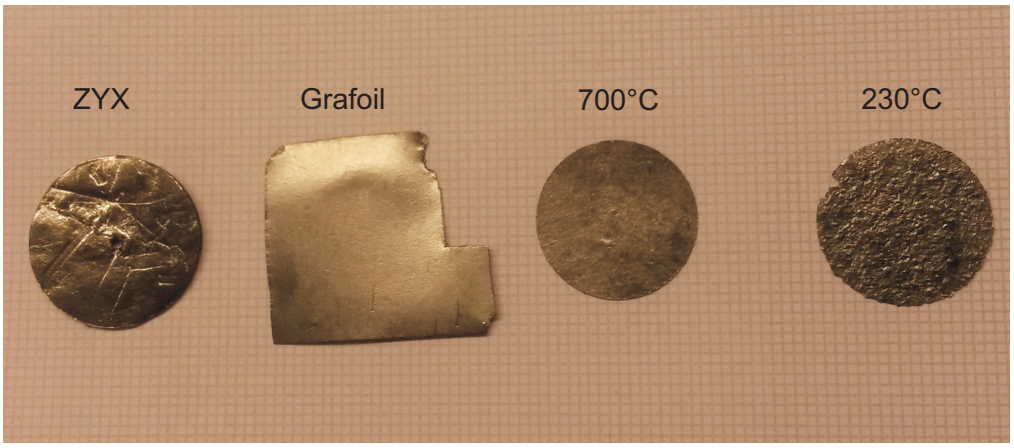

Figure 3.28: Photograph showing two foils that have been pressed from graphite exfoliated at different temperatures. Samples of ZYX and Grafoil have been included for reference.

3.5 Minimum Number of Detectable Spins

As is discussed in sections 3.1.4 and 3.2.1, the graphite source material and intercalation method have been chosen so as the maximise the surface coherence lengths in the resultant exfoliated material. It seems intuitive therefore, that the exfoliation process can also be adjusted and optimised with this specific goal in mind.

It was concluded that we should attempt to exfoliate the graphite as little as possible; a more vigorous exfoliation results in greater disruption of the graphite host material, which in turn leads to smaller crystallite sizes and commensurably smaller surface coherence lengths, as evidenced by the data in table 2.1. This unfortunately means that the specific area and the typical surface coherence length of a substrate can be considered as conflicting requirements. In principle, if surface coherence length were the only requirement then it should be sufficient to adsorb a gas onto a single (001) face of a high quality graphite crystal. Indeed, there have been studies [100, 101] that have shown that this is possible using certain scattering techniques. For NMR studies however, it is necessary to have a larger adsorption surface area.

Other works on ZYX have shown [73] that it is possible to perform SQUID NMR measurements on a substrate with as little as 2 m^2/g, however, in order to establish the boundaries for this work it was necessary for us to calculate the minimum surface area that could be used in a hypothetical SQUID NMR experiment, and still obtain a signal. This was done using specifications from previous low temperature NMR experiments performed here at Royal Holloway [102, 103]. The calculations shown here follow a similar form to those found elsewhere [102, 103, 104] and assume some knowledge of basic NMR. A brief introduction to the theory of NMR can be found in chapter 5.

To begin, we will assume an experimental cell like the one described in sections 5.3.5 - 5.3.11, which is a common Royal Holloway cell design, whereby the substrate is encapsulated by two orthogonally mounted saddle coils. By reciprocity, the flux threading through the receiver coil, ϕ_r can be expressed as

$$\phi_r = M_0 V_s B_{1,c} \kappa, \tag{3.2}$$

where M_0 is the magnetisation of the sample, V_s is the sample volume, $B_{1,c}$ is the field current ratio of the receiver coil, and κ is a factor between 0 and 1 which accounts for inhomogeneity in the receiver coil field profile and the sample filling factor.

If the sample volume contains a collection of spin 1/2 ^{3}He atoms, which are then assumed to behave as a paramagnet, the magnetisation of the sample can be obtained by the expression,

$$M_0 = N_v \mu \tanh(\hbar \gamma B_0 / 2 k_B T), \tag{3.3}$$

where N_v is the volumetric number density of the particles, γ is the gyromagnetic ratio, and B_0 is the NMR field. In the limit $\hbar \gamma B_0 << 2 k_B T$, this can be simplified

to,

$$M_0 = \frac{N_v \mu \hbar \gamma}{2k_B T} B_0 \tag{3.4}$$

further simplifying by substituting $N_v = N/V$, $\omega = \gamma B_0$ and $\mu = \gamma\hbar\ /2$

$$\phi_r = \frac{N\gamma\hbar^2\omega}{4k_B T} B_{1,c}, \kappa \tag{3.5}$$

As is shown in figure 5.9, the receiver coil is coupled via a flux transformer and through an input coil onto the SQUID. The flux that is then coupled through the SQUID for detection is given by

$$\phi_{sq} = \left(\frac{M_i}{L_r + L_i}\right)\left(\frac{N\gamma\hbar^2\omega}{4K_B T}\right) B_{1,c}\kappa, \tag{3.6}$$

where L_r and L_i are the inductances for the receiver and input coil respectively, and M_i is the mutual inductance between the input coil and the SQUID.

For a frequency domain experiment the signal to noise ratio can be expressed as

$$\left(\frac{S_p}{N_p}\right)_f = \left(\frac{\phi_{sq}}{K_N^f}\right)\sqrt{\frac{T_2^*}{2K_T\langle P_N\rangle}}, \tag{3.7}$$

Where K_N^f is the ratio of the peak noise to the rms noise in the frequency domain and is taken to be 2.5 [105]. K_T is defined in terms of the capture time $T_{cap} = K_T\ T_2^*$. A general rule is that one should capture for at least $5T_2^*$ to avoid line distortion effects, thus this is taken as the value for K_T. $\langle P_N\rangle$ is the intrinsic device noise and can be found in the SQUID device specifications from the manufacturer [106].

Using experimental specifications from previous works [102] to substitute into equations 3.6 and 3.7, it is possible to obtain a reasonable estimate of what the minimum number of detectable spins will be.

The following values have been substituted; $M_i = 7$ nH, $L_i = L_r = 1.1$ μH, $B_{1,c}$

= 2.5 mTA^{-1}, $K_T = 5$, $K_T^f = 2.5$, $\langle P_N \rangle = 0.525\ \mu\phi_0 \mathrm{Hz}^{-1/2}$. For ^{3}He, $\gamma = 2\pi \times$ 32.44 MHz T^{-1} and for a recent NMR experiment [103] at T = 1 K, the operating frequency was 50 kHz and T_2^* times were on the order of 1 ms. The resulting signal to noise in terms of a number, N of ^{3}He atoms is;

$$\left(\frac{S_p}{N_p}\right)_f = 3.779 \times 10^{-19} N \tag{3.8}$$

If the criterion for detectability is taken to be that the signal to noise ratio is greater than 1, then the minimum number of detectable ^{3}He spins in an experiment with these specifications is 2.646×10^{18}. By way of example; in the first monolayer of ^{3}He on graphite a commensurate $\sqrt{3} \times \sqrt{3}$ solid is formed at approximately 0.6 coverage. At this point the density is 6.36 atoms per nm^2, or more simply 6.36×10^{18} per m^2 of surface area. For this reason it was decided that it would be preferable to keep the substrate specific surface area at around 1 m^2/g in order to keep the signal size at a measurable level.

3.6 Summary

During this work, many batches of GICs have been manufactured in accordance with the procedures laid out in section 3.2.3. As can be seen from table 3.3, a total of 17 batches have been made using the Madagascan flake. Typically these batches were comprised of 1 - 2 g of GIC material, from which small amounts (0.1 - 0.2 g) were taken to perform test exfoliations, many of which were made into prototype substrate foils using the pellet press described in section 3.4. Each of these prototypes is then designated using a Number/Letter, where the number denotes the GIC batch that was used, and the letter labels the specific exfoliation procedure.

As is discussed in section 3.5, it is thought that vigorous exfoliation results in greater expansion of the graphite host, exposing larger surface area for adsorption.

This unfortunately comes at the expense of surface coherence length, so it has been assumed that a 'gentle' exfoliation procedure is preferable. To this end, it was felt that the exfoliation temperature, T_E provided the best means of achieving this 'gentle' exfoliation. This is evidenced by the comparison in figure 3.28; the foil that was exfoliated at 230°C has undergone less exfoliation than the foil exfoliated at 700°C, which results in the 230°C foil appearing more granular.

A number of prototype foils were then made and subjected to the characterisation methods described in the next chapter, with a particular emphasis on crystallite sizes from (110) diffraction line broadening and surface area measurements using adsorption isotherms. A list of the prototype substrates that were successfully characterised[5] can be found below in table 3.6, which also includes a summary of the parameters used in their manufacture.

As is discussed in this chapter, these exfoliations took place whilst actively maintaining the vacuum in the reaction vessel. The sample was then left at the exfoliation temperature, T_E overnight under vacuum before subjecting it to a second heat treatment, which involved ramping the furnace to 700°C. The exfoliated material was removed and compressed into foils using the pellet press.

Special attention should be given to the batch 11 NMR substrate which was manufactured for the preliminary NMR experiment described in chapter 5. The total mass of GIC batch 11 was 4.8 g, which was processed in four large exfoliations, using the conditions shown in the table for each run. This is in contrast to the usual 0.1-0.2 g amounts used to manufacture the other prototype substrates. After all the exfoliations had been completed, the collected material (3.8 g in total) was transported to RHUL where it was subjected to yet further heat treatment. The procedure adopted here was to load the exfoliated sample into molybdenum boats, which were then placed into a furnace and subjected to 24 hours at 1000°C under

[5]In many cases, due to their fragile nature, many prototype foils would disintegrate during handling before a characterisation could be completed.

Sample	T_E(°C)	Tube	Heat Treatment	Pressure (bar)
4H	700	Quartz	700°C	180
5E	400	Quartz	20°C/min to 700°C	180
6A	400	Quartz	20°C/min to 700°C	180
6C	350	Quartz	none	180
6D	250	Pyrex	none	180
8A	250	Quartz	5°C/min to 700°C.	180
8B	225	Quartz	none	180
8C	220	Quartz	5°C/min to 700°C	360
8D	200	Quartz	5°C/min to 700°C	180
8E	224	Quartz	1°C/min to 700°C	180
9A	200	Quartz	0.5°C/min to 700°C	180
9B	190	Steel	0.5°C/min to 700°C	180
11-(NMR)	350	Quartz	1°C/min to 700°C	180
14A	200	Steel	0.5°C/min to 700°C	180
14C	200	Steel	0.5°C/min to 700°C	180

Table 3.4: Summary of prototype substrate manufacture parameters.

vacuum. As the results of section 4.3 show, the choice of molybdenum boats has likely lead to some contamination in this substrate. After this heat treatment, the exfoliated material was then pressed into the standard 19 mm foils. A hole punch was then used to cut these foils down to 16 mm in diameter so as to fit into the NMR cell, where the cell loading process is described in detail in section 5.3.9. The offcuts from the punching process were kept for characterisation.

Chapter 4

Substrate Characterisation

The previous chapter outlined the basic procedure required to intercalate and then exfoliate flakes of Madagascan graphite. The exfoliated material can then be compressed using a laboratory pellet die. The exfoliated material holds together without the aid of any binders and the resultant disk, or 'foil' is structurally quite stable. These foils are the prototype substrates which are then ready to be characterised.

4.1 X-rays: Crystallite Sizes

Given the stated aim of this project, to produce a substrate with very large surface coherence lengths, it would be preferable to have a characterisation program whereby the value of L_s can be reliably measured. As is discussed in section 2.2.1, L_s can be estimated by analysis of (hk) lineshapes obtained by diffraction from 2D commensurate crystals at monolayer completion. Unfortunately, such a measurement poses a significant technical challenge, not least because of the requirement of synchrotron radiation. Another characterisation method was therefore needed which could provide indicators of the substrate surface quality and which can be performed within a reasonably short time frame. Atomic Force Microscopy (AFM)

and Transmission Electron Microscopy (TEM) have been employed previously [107, 73] as an alternative to monolayer scattering to ascertain the surface coherence length of ZYX-type substrate. Some AFM has been applied in this project, however as a technique it was deemed to be too time-consuming to be useful as a primary means of characterisation.

We decided that estimating the typical crystallite sizes of the prototype substrates could be used as an indirect measure of the substrate surface quality. As can be seen from table 2.1 in section 2.3, the in plane crystallite dimension of ZYX has a literature value of >3000 Å, with a surface coherence length of 1800 - 2300 Å. For Grafoil, the in plane dimension of 400 Å accommodates a surface coherence length of 100 - 200 Å. These numbers are self consistent; the lateral size of an adsorbing (001) face cannot be larger than the lateral size of the crystallite on which it resides. This leads to our central assumption; for a substrate to have large surface coherence lengths, it is then a necessary (but not sufficient) condition that the substrate must be comprised of crystallites with a large L_a dimension.

The substrate preparation procedure described in the previous chapter then went through many iterations with the aim of producing a substrate with the largest possible crystallite sizes, on the premise that this would result in commensurably larger surface coherence lengths. Crystallite sizes were estimated by analysing the line profiles obtained by X-ray diffraction from our prototype substrates.

4.1.1 The Diffractometer

X-ray diffraction has been used to confirm the staging of our graphite intercalation compounds (section 3.2.4), to estimate the crystallite sizes of the prototype exfoliated substrates (section 4.1) and to estimate their mosaic spread (section 4.4). Two instruments were used, both PANalytical X'pert pro [108] Bragg-Brentano geometry powder diffractometers. The Bragg-Brentano scattering geometry, which is outlined

in figure 4.1, is usually set up to perform a standard $\theta - 2\theta$ scan. In this scenario the specimen is placed on the sample plate and the angle Ω is fixed such that $\Omega = \theta$. The source and the detector then move in unison in an arc above the sample maintaining $\Omega = \theta$, such that to scan through 1° in 2θ, the source and the detector must each contribute 0.5° in θ. Both the source and the detector can move around the arc with a minimum step size of 0.001°, which implies that the minimum step size in 2θ is then 0.002°.

The sample plate is able to tilt to either side with a range of approximately $\pm$ 10° in such a way that the angle Ω can be varied independently of 2θ. During a rocking curve measurement, the source and detector are kept fixed and the sample plate rocked back and forth allowing an independent scan through Ω to take place.

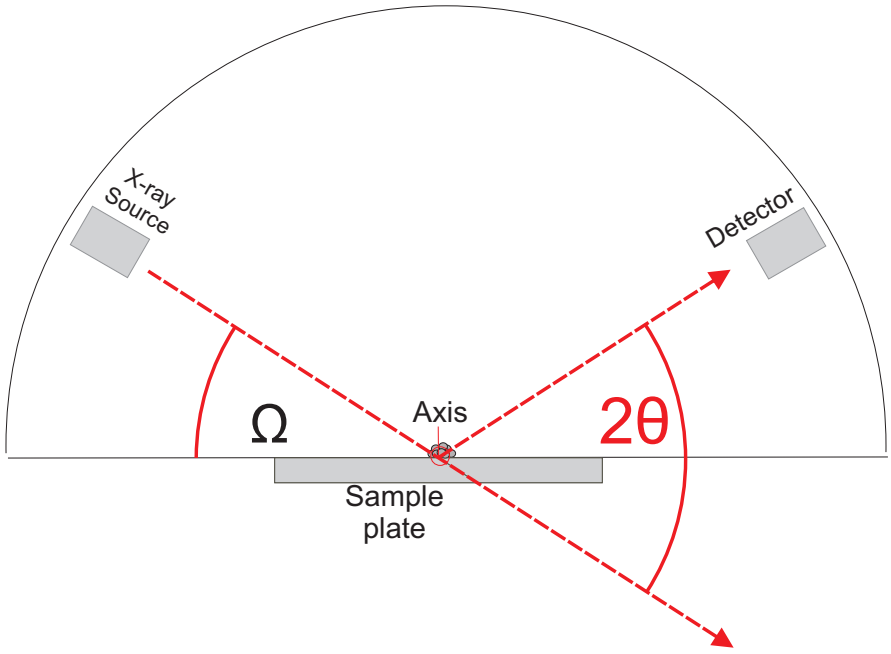

Figure 4.1: Bragg-Brentano diffractometer geometry; the sample lies on the sample plate, whilst the source and detector move in an arc above the sample around a fixed axis. The sample plate can be used to define a coordinate system for the diffractometer and this is shown in figure 4.2.

The two diffractometers differed only in the wavelength of their sources; both of which were of the same rotating anode design whereby electrons are accelerated to energies of 20-40 keV at a rotating target disc made from either copper or molybdenum. The molybdenum source produces a Mo-K_α doublet with wavelengths 0.70930 Å and 0.71359 Å. The other source produces radiation characteristic of Cu-K_α, the wavelengths being 1.54056 Å and 1.54439 Å for the $K_{\alpha 1}$ and $K_{\alpha 2}$ respectively. The copper tube was favoured for its greater intensity.

The X-rays that are produced in the tubes then pass through a series of collimators and monochromators. Additionally, there are two adjustable apertures between the source and the sample which are called the divergence (D-slit) and anti-scatter (AS-slit) slits which control the beam spot size at the sample. These slits both had a minimum aperture size of 0.5 mm and each could be widened in increments of 0.1 mm.

The X-rays diffracted by the sample are recorded by a solid state detector which measures the diffracted intensity. Before entering the detector the beam first passes through a set of Soller slits [109] and the receiving slit. Soller slits are a series of stacked copper foils which are separated by a few mm, and serve to further collimate the beam. The receiving slit (R-slit) has a similar effect to the divergence and anti scatter slit, and defines the size of the beam that is inspected by the detector, the width of the receiving slit can be as narrow as 0.01 mm, and can be increased in increments of 0.01 mm. The divergence, anti-scatter and receiving slit play a key role in determining the instrument resolution function of the diffractometer. The meaning of a resolution function and how it is measured is discussed in more detail in section 4.1

It is useful to define a coordinate system for the diffractometer, particularly when working with samples which display some degree of preferred orientation. In texts on powder diffraction [110] it is common to define several coordinate systems within the

diffractometer with origins centred on the source, the sample stage and the detector. In our case, it is sufficient to define only one coordinate system which uses the sample stage as the fixed point of reference, and all measurements and sample orientations can then be expressed in terms of this coordinate system. Figure 4.2 is a re-rendering of the Bragg-Brentano geometry of figure 4.1 with a coordinate system defined on the top surface of the sample stage. In a normal 2θ scan, the source and the detector are

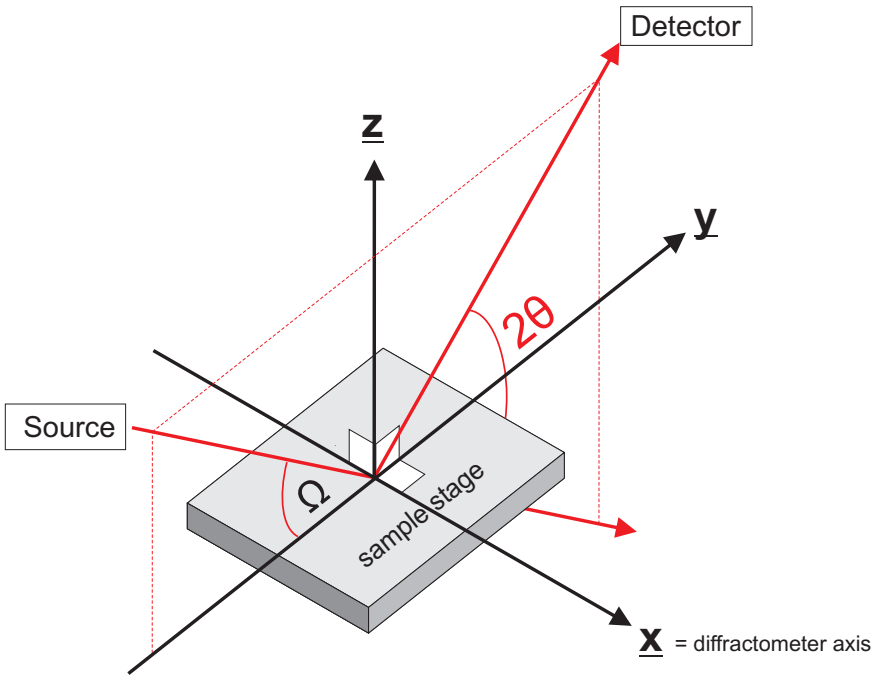

Figure 4.2: Bragg-Brentano diffractometer coordinate system

constrained to move in an arc within the y-z plane above the sample, where the x-axis defines the axis of rotation for the whole diffractometer. As is described in section 2.2.1, graphitic substrates are not isotropic powders, instead they display varying degrees of crystallite alignment(mosaic spread). In this scenario it will be necessary to define the orientation of the sample c-axis within the diffractometer coordinate system for different measurements. For example, a graphite sample laid flat onto the sample stage such that the c-axis is nominally aligned with the diffractometer z-axis

is the optimum arrangement for recording $(00l)$ reflections. Sample orientations will be discussed in greater detail in section 4.1.5.

4.1.2 Line Broadening Analysis

The average size of a crystallite along a particular crystallographic direction can be inferred from the peak broadening from (hkl) lines obtained by powder diffraction. For example, the c-axis crystallite dimension, L_c of a graphite sample can be estimated from the broadening of the $(00l)$ diffraction peaks. Similarly, estimates of the L_a dimension can be obtained from the broadening of the $(hk0)$ peaks.

An understanding of how the finite size of the diffracting domain can lead to broadening can be seen by a simple analysis of Bragg's law ;

$$n\lambda = 2d\sin(\theta), \tag{4.1}$$

By recognising that the crystallite dimension, L, along a particular axis can be expressed as $L = md$, i.e. there is a finite number, m of diffracting crystallographic planes. Equation 4.1 can then be rewritten as;

$$\begin{aligned} mn\lambda &= 2md\sin(\theta) \\ &= 2L\sin(\theta), \end{aligned} \tag{4.2}$$

This equation can then be differentiated with respect to θ to give:

$$0 = 2(\Delta L)\sin(\theta) + 2L\cos(\theta)\Delta\theta \tag{4.3}$$

The smallest possible increment in ΔL is the distance, d between the diffracting

planes. Performing this substitution and rearranging gives;

$$L = \frac{d\sin(\theta)}{\cos(\theta)\Delta\theta} \tag{4.4}$$

Substituting $\lambda/2 = d\sin(\theta)$ from equation 4.1;

$$\text{Ł} = \frac{\lambda}{2cos(\theta)\Delta\theta} \tag{4.5}$$

The quantity $2\Delta\theta$ can be interpreted as the range in 2θ over which the Bragg condition is satisfied, i.e., the intensity can be described by some peak shape with a characteristic width broadening parameter, β. Making this substitution results in an expression for the crystallite size in terms of the peak broadening called the Scherrer equation [111]

$$L = K\frac{\lambda}{\beta(2\theta)\cos(\theta)} \tag{4.6}$$

The derivation shown here is a simplified derivation due to Klug and Alexander [112]. The dimensionless pre-factor K that has been added here arises from advanced derivations [113] which take into account the shape of the diffracting crystallites and the width definition for β[1] that is used. The value of K typically lies between 0.89 and 1, and for graphite measurements, $K = 0.94$ [74] has been used.

The derivation of the Scherrer equation presented above is predicated on the assumption that the diffracting crystallites are finite, but otherwise perfect. If the crystallite contains defects such as vacancies or stacking faults however, then this will cause local disruption of the lattice, which manifests as a variation in the lattice d-spacing. Using a similar differential analysis of Bragg's law, Stokes and Wilson

[1]There being two popular methods for defining width; the Full Width at Half Maximum (FWHM) and the integral breadth, which is the width a rectangle with the same height and integrated area as the peak.

[114] were able to relate the *inhomogeneous strain* to the peak broadening;

$$2\frac{\Delta d}{d} = 2\Delta\theta\cot(\theta), \tag{4.7}$$

where again $2\Delta\theta$ can be equated with the peak width, β, and the quantity $2\Delta d/d$ represents the inhomogeneous strain within a sample. The different dependence in θ of equations 4.6 and 4.7, means that it is possible to separate the size and strain broadening contributions from the sample if multiple orders of the same reflection are obtained. Williamson-Hall [115], Double-Voigt [116] and Warren-Averbach [117] are examples of analysis techniques that are able to quantify the size and strain within a sample using multiple reflection orders.

The study of material micro-structure through the broadening of diffracted peaks is known as Line Broadening Analysis and comprehensive reviews of the field and its techniques can be found in the collections by Mittemeijer [118] and Snyder [119]. Before any broadening analysis can be applied it is first necessary to remove the broadening contribution of the instrument.

4.1.3 Instrumental Broadening

It is common in optics, spectroscopy and diffraction to use the language of signal analysis to model the measurement process; the measured profile, I^m arises from convolution of the instrument, I^i with the sample signal, I^s.

$$I^m = I^i * I^s \tag{4.8}$$

In an ideal measurement, the instrument is capable of infinite discrimination with an infinite acceptance, i.e., the form of I^i is described by a Dirac delta function. In reality however, instruments have finite resolution and it is common to perform the reverse of equation 4.8 by deconvolving I^i from the measured profile I^m to obtain

an estimate of I^s.

In X-ray powder diffraction, this deviation from the ideal manifests as intrinsic broadening in the measured intensity of diffraction lines, where non-idealities in the diffractometer optics are thought to be the most important sources of instrumental broadening[120], for example, if the X-rays that are produced are not perfectly collimated, then the beam will display some finite divergence. As is shown in figure 4.3, this can be be seen to introduce uncertainties into the angle at which the beam strikes the sample which consequently will introduce uncertainty in the angle at which the diffracted peak intensity is measured. This effect can be compounded further by any offsets from the diffractometer axis and by transparency in the sample. Discussion and modelling of these broadening contributions can be found in the work of Ida et al. [120, 121]

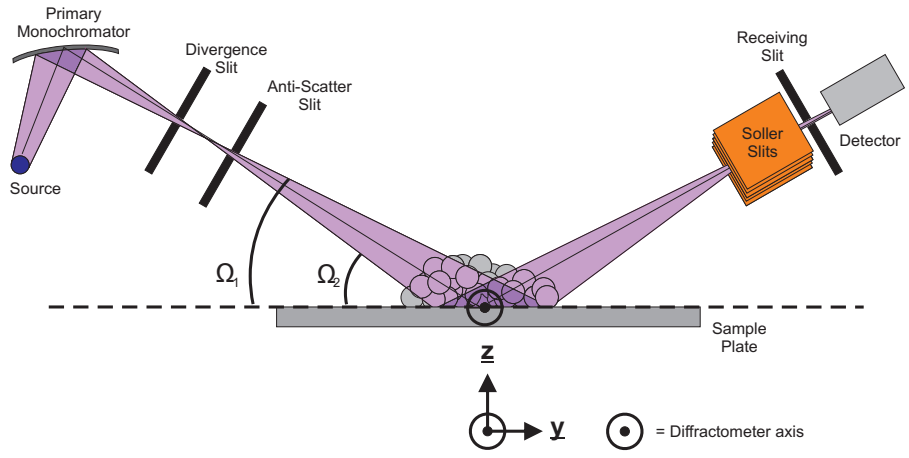

Figure 4.3: Schematic of diffractometer optics and how they contribute to broadening, by defining the footprint of the beam and its divergence. The uncertainty in the beam path is shown by the angles Ω_1 and Ω_2.

This intrinsic and unavoidable broadening then represents a fundamental res-

olution limit of the instrument which be interpreted in two ways; as the smallest d-spacing that can be resolved or, given the inverse relationship between broadening and crystallite size, as a reasonable upper limit to the size of crystallite that can be measured. Higher resolutions correspond to smaller discernible d-spacings and larger measurable crystallite sizes, and as can be seen from figure 4.3, higher resolutions are achieved when the various slit apertures are as small as possible so as to minimise the beam divergence. Unsurprisingly, the consequence of narrowing these slits is reduced intensity at the detector and a compromise must be made between the resolution and achieving an acceptable signal to noise ratio.

Naturally in order to remove the broadening contribution of I^i, the instrument resolution must be estimated. There are two approaches; analytic and empirical. Ida and co-workers have shown that it is possible to model both lab X-ray sources [122] and synchrotrons [121] to obtain an analytic representation of the instruments' resolution. The more common empirical approach is to use a standard material in which size and strain effects have been annealed out to immeasurable levels, so that the diffracted peaks from the sample are due solely to the broadening of the instrument. More detailed aspects of measuring the instrument resolution are discussed in the next section.

Once I^i has been characterised, the computational means by which it is removed from I^m also has two approaches. The first, the so-called Stokes deconvolution [123] makes use of the deconvolution theorem by taking the Fourier transform of both I^m and I^i. This is generally considered to be the most rigorous method, however it is computationally intensive and is complicated further by the presence of the K_α doublet in diffracted profiles.

The second approach is based on analytic fitting of the diffraction peaks. By moulding some function to both I^i and I^m it is potentially very simple to remove the instrument contribution via some simple algebraic expression. If possible, it

is preferable to fit both I^m and I^i with functions which have simple analytic convolutions. An obvious choice for such a function is that workhorse of science; the Gaussian. If both I^i and I^m are fitted with Gaussians of integral breadth β_g^i and β_g^m respectively, by equation 4.8, I^s is another Gaussian with a width, β_g^s given by;

$$\beta_g^s = \sqrt{(\beta_g^m)^2 - (\beta_g^i)^2} \tag{4.9}$$

Where the Gaussian is given by;

$$g(x) = I(0) \exp\left(\frac{-\pi x^2}{\beta_g^2}\right) \tag{4.10}$$

Another common fitting function is the Lorentzian, which also shares a favourable convolution property; using only Lorentzians in equation 4.8 results in the following simple deconvolution expression:

$$\beta_l^s = \beta_l^m - \beta_l^i \tag{4.11}$$

Where the Lorentzian is given by

$$l(x) = I(0)\frac{1}{\beta_l^2/\pi^2 + x^2} \tag{4.12}$$

Unfortunately neither function adequately fits diffraction data particularly well [112, 124]. It is known that the Voigt (and it approximations) give superior fits to powder diffraction data [125, 126].

The Voigt function can be be constructed by a convolution of a Gaussian with a Lorentzian;

$$V(x, \beta_g, \beta_l) = (g * l)(x) = \int_{-\infty}^{+\infty} g(x', \beta_g) l(x - x', \beta_l)\, dx', \tag{4.13}$$

where both the Gaussian and Lorentzian are given in equations 4.10 and 4.12 respectively. The Voigt is a very useful line-shape that finds application throughout diffraction and spectroscopy and as such has received a great deal of mathematical attention with the aim of efficient and rapid computation. Many modern numerical implementations are expressed in terms of the complex error function. Authors such as Balzar [127] present the Voigt function as proposed by Langford [128]:

$$V(x) = I(0)\left(\frac{\beta}{\beta_l}\right) Re\left[erfi\left(\frac{\pi^{1/2}x}{\beta_g} + ik\right)\right], \tag{4.14}$$

where

$$k = \frac{\beta_l}{\pi^{1/2}\beta_l} \tag{4.15}$$

As a consequence of being composed of Lorentzian (β_l) and Gaussian (β_g) components, the Voigt shares the convolution property that if I^i and I^m in equation 4.8 are modelled as Voigts then I^s can be reasonably assumed to be a Voigt also.

Deconvolution of Voigt profiles simply requires that the individual Gaussian and Lorentzian components of each profile are separately deconvolved in accordance with equations 4.9 and 4.11

$$\beta_g^s = \sqrt{(\beta_g^m)^2 - (\beta_g^i)^2} \tag{4.16}$$

$$\beta_l^s = \beta_l^m - \beta_l^i \tag{4.17}$$

Where the superscripts, s, m and i denote sample, measured and instrumental profiles as before, and the subscripts l and g distinguish between Lorentzian and Gaussian components of each profile. Combining these via the Voigt parameter

$$k^s = \frac{\beta_l^s}{\pi^{1/2}\beta_g^s}, \tag{4.18}$$

the full integral breadth of the sample, β^s of the sample signal I^s can now be calculated via;

$$\beta^s = \frac{\beta_g^s \exp(-(k^s)^2)}{k^s} \tag{4.19}$$

With function breadth methods all that is required are the quantities β^s, β_g^s and β_l^s as these now fully represent the line profile of the sample free from contributions from the instrument. The assumption that all profiles in X-ray diffraction can be modelled as a Voigt is the central tenet of the "double-Voigt" method and is described in detail by Balzar [127].

4.1.4 Measuring and Fitting I^i

Any analysis of line broadening requires characterisation of the instruments resolution which can be empirically measured by diffracting from a specially prepared sample - called the standard - in which size and strain effects have been annealed out to immeasurable levels. It is also necessary to balance the crystalline perfection of the standard against the requirements imposed by the powder condition. An isotropic powder composed of well annealed 5-10 μm crystallites is considered to be the optimum [129] compromise between these conflicting requirements.

The standard that was eventually chosen was a mica slide (synthetic fluorophlogopite - NIST SRM 675) that is part of the instrument calibration kit. Mica standards are typically used to calibrate peak position at low 2θ, however the sharp peaks obtained from the mica compare favourably to similar measurements performed on LaB_6 standards reported elsewhere [126]. Although not ideal, it was concluded that the mica standard gave a reasonable estimate of the instrument resolution. The mica also had the added advantage that it presented many reflections throughout 2θ, meaning that the instrument resolution at various angles could be well characterised.

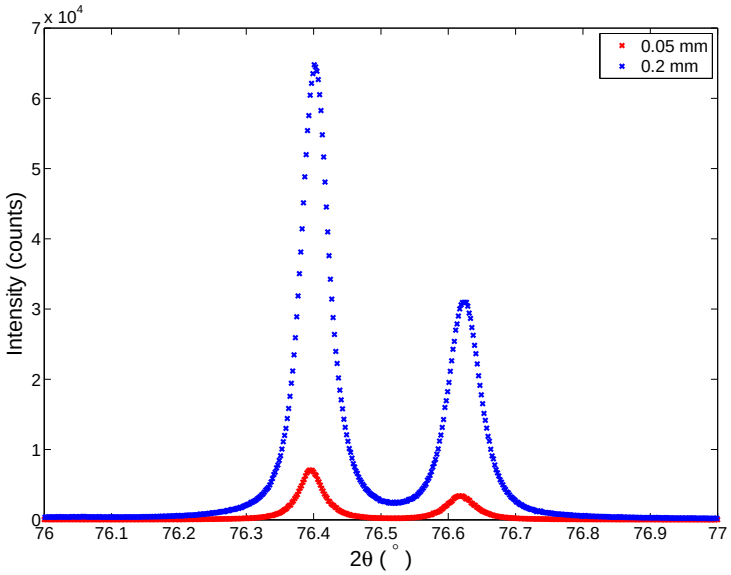

Figure 4.4: Diffracted intensities from the (008) reflection of the mica standard. The divergence and anti-scatter slit settings were 0.5 mm in both measurements. The graph shows the effect of different receiving slit width. The Cu-K_α doublet is well resolved.

The diagram of figure 4.3 illustrates the importance of the divergence, anti-scatter and receiving slit in defining the instrument resolution, where narrower slit apertures correspond to increased resolution. It is important to note that any characterisation of I^i can only be applied to measured profiles, I^m measured at the same angle and with the same instrument settings. Typically the divergence and anti-scatter slit width was kept fixed at 0.5 mm and the resolution was adjusted using the receiving slit only. Figure 4.4 shows the difference in intensity for two different receiving slit widths.

These measured peaks then require fitting with Voigt profiles in order to be able to remove their contribution from the I^m intensities obtained when measuring graphite samples. All fitting and analysis was done in MATLAB, making use of the MFit package [130] which is a specialised toolkit written specifically to analyse

diffraction data. As is shown in figure 4.5, each peak of the K_α is modelled as a single Voigt such that the entire doublet intensity is fitted as the sum of two Voigt profiles. Analysis can then be performed using the width parameters from each individual fitted Voigt, though typically the larger $K_{\alpha 1}$ peak was used.

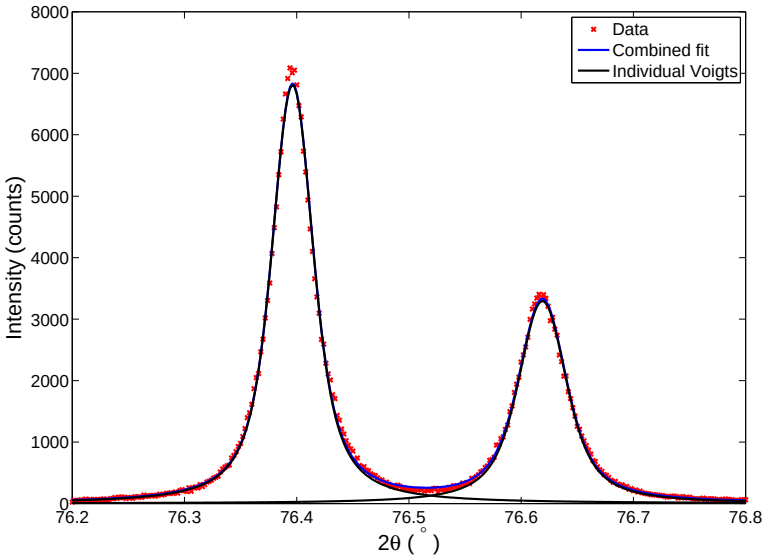

Figure 4.5: Fitted intensity profile for the 0.05 mm recorded resolution profile from figure 4.4. Due to the high resolution, the K_α is well resolved and peak overlap is minimal.

At this point it should be noted that the expressions 4.10, 4.12 and 4.14 given for the Gaussian, Lorentzian and Voigt respectively in the previous were expressed in terms of the integral width β, largely due to the simplicity of expression. The Mfit toolkit fits Gaussian, Lorentzians and Voigts using the FWHM as the width definition. This does not change the analysis significantly as conversion between the integral width, β and the FWHM, f for both Gaussian and Lorentzian profiles requires only a multiplicative factor:

$$\beta_g = \frac{f_g}{2}\sqrt{\frac{\pi}{\ln 2}} = 1.064467019 f_g \tag{4.20}$$

$$\beta_l = \frac{\pi f_l}{2} = 1.570796327 f_l \tag{4.21}$$

It is easy to see that these multiplicative factors cancel out during the deconvolution procedures of equations 4.16 and 4.17. The FWHM of the Voigt, f_v is then calculated from the Gaussian and Lorentzian FWHM components using the expression;

$$f_v = 0.5346 f_l + \sqrt{0.2166 f_l^2 + f_g^2} \tag{4.22}$$

which approximates the Voigt FWHM to within 0.02 % [131]. In the case of the fit to the mica standard that is shown in figure 4.5, the fit values obtained for the $K_{\alpha 1}$ peak of the doublet are $f_g^i = 0.025$ °, $f_l^i = 0.029$ ° and $f_v^i = 0.045$ °. Resolution profiles were recorded for different receiving slit widths, however the profile that is recorded and fitted in figure 4.5 is representative of the broadening that was typically deconvolved from the measured profiles.

4.1.5 Substrate Crystallite sizes

With an established method of removing the instrumental broadening, the next stage was to estimate crystallite sizes using the broadening of peaks obtained from diffraction from our samples. As has been discussed, the primary hypothesis was that having large in-plane crystallite dimensions, L_a is a necessary condition for large surface coherence lengths. For this reason we decided to focus on analysing $(hk0)$ reflections from the graphite substrates. This presents some technical challenges; the prototype substrate foils such as the ones shown in figure 3.28 displayed a favoured orientation such that lying the foil flat on the sample plate of a Bragg-Brentano type diffractometer will result in only $(00l)$ reflections being measured. In order to measure the $(hk0)$ family of reflections, the foil must stood on its side as shown in figure 4.6, so that substrate basal planes are parallel with the diffractometer x-z plane. Unfortunately the sample stage is a fixed feature of the diffractometer, and does not present much scope for modification without significant overhaul, so the foil had to be fixed in place by using an adhesive which proved to be crude yet effective. In order for the beam to pass directly through the main body of the substrate foil rather than through the adhesive holding it in place, some nylon spacers were made up that provided a 10 mm offset of the sample stage from the diffractometer axis.

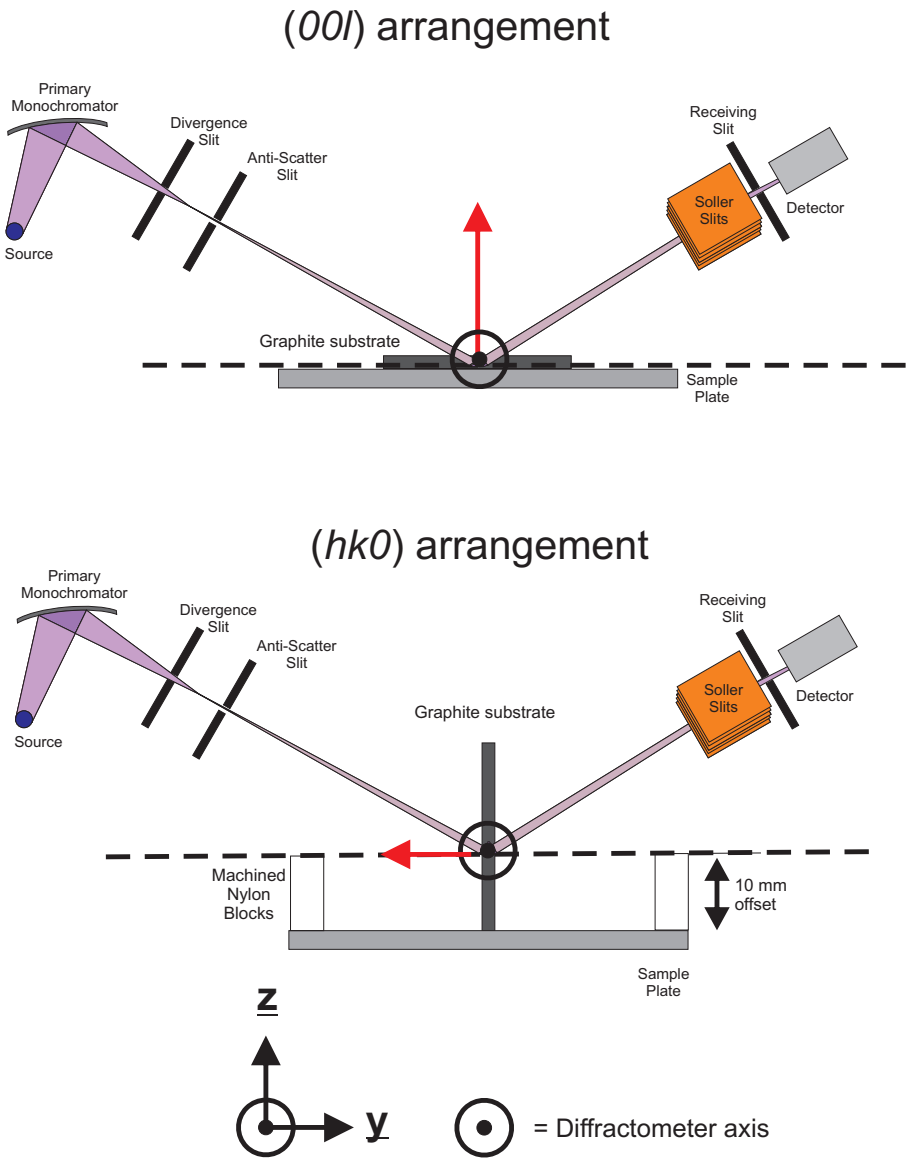

Figure 4.6: Diagram of possible substrate orientations to obtain $(00l)$ and $(hk0)$ reflections. The red arrows indicate the c-axis direction of the samples.

This improvised geometry is recognised as being sub-optimal and more effective geometries will be discussed in section 4.6 of this chapter. It is possible however to perform a simple optimisation routine which maximises the scattered intensities; by setting the diffractometer to an angle in 2θ where a peak is expected to occur (table 4.1), and then performing a quick scan in 2θ with relatively wide divergence, anti-scatter and receiving slit widths, a low resolution ($hk0$) peak can be recorded. A rocking curve is then performed on this peak, and the results used to determine an offset in Ω which allows the orientation of the foil to be modified to optimise the intensities. An iterative process then ensues whereby the slit widths are progressively narrowed so as to increase the resolution, followed by a brief rocking curve to further optimise the intensity. This cycle is repeated until the working resolution of the instrument has been reached. For most measurements reported here, the divergence and anti-scatter slit were set to 0.5 mm and the receiving slit was typically set to 0.05 mm. The resolution recording for this instrument setting is shown in figure 4.5.

In addition to these difficulties in obtaining the ($hk0$) reflections from the graphite substrates, there is also the added inconvenience presented by the crystal structure of graphite itself. As the calculated peak position and intensities in table 4.1 show, the ($hk0$) planes are weakly scattering and the second order reflections of the (100) and (110) are virtually non-existent.

λ	(hkl)	2θ (°)	I/I_{002} (%)
Cu	(002)	26.56	100
Cu	(004)	54.69	6.81
Cu	(100)	42.38	3.54
Cu	(200)	92.58	0.21
Cu	(110)	77.51	5.37
Cu	(220)	-	-
Mo	(002)	12.14	100
Mo	(004)	24.42	7.98
Mo	(100)	19.15	3.85
Mo	(200)	38.88	0.27
Mo	(110)	33.50	7.21
Mo	(220)	70.402	0.64

Table 4.1: Selection of graphite powder peak positions and intensities calculated using PowderCell [132] for Cu-K_α (1.5406 Å) Mo-K_α (0.0709 Å) radiation

We found that we could reliably measure the (110) reflection from various graphite samples by using the more intense copper X-ray tube. However, it was often necessary to perform scans with long exposure times to allow counts to accumulate in the detector, in many cases this meant leaving the measurement to run overnight.

Recognising the difficulties in measuring these samples, and the fact that this is a novel technique for the low temperature group, we decided to check the feasibility of the method by comparing the (110) broadening in samples in which the hierarchy of crystallite sizes is known to some extent. It seems reasonable to expect that a sample of HOPG would be composed of larger crystallites than ZYX which in turn is more crystalline than Grafoil. In terms of the (110) reflection we should therefore expect Grafoil to display the broadest peaks and HOPG to display the sharpest.

A sample of Grafoil-GTA grade was obtained from an existing laboratory stock which has been used in previous low temperature experiments at RHUL. The material is typically 150 μm in thickness, and is a flexible foil like material which can be easily cut using scissors. The specimens that were measured were small 20×20 mm squares cut from a larger sample.

ZYX is a more elusive material as UCAR-ZYX is no longer commercially available. Fortunately however, M. Bretz had sent Dr. Chris Lusher a small sample of ZYX in 1991 which had then been used in a torsional oscillator experiment. The sample was a 17 mm diameter, 3 mm thick disk. This was sliced into two disks 2 mm and 1 mm thick. The 1 mm disk was then split further into two 0.5 mm thick pieces. One of these 0.5 mm ZYX specimens was then used for the X-ray characterisations.

For the HOPG sample, a small fragment of ZYH was found which was approximately 10×10 mm in area and 0.5 mm in thickness. In all these samples, the thickness dimension is aligned with the c-axis. These samples were then mounted in turn onto the diffractometer as shown in figure 4.6. The intensity was optimised using the iterative rocking curve described in this section, and high resolution scans of the (110) peaks were obtained for each sample. Figures 4.7 show the results of these measurements. In each case the diffractometer settings were the same, the divergence and anti-scatter slit were set to a width of 0.5 mm, whilst the receiving slit width was 0.05 mm.

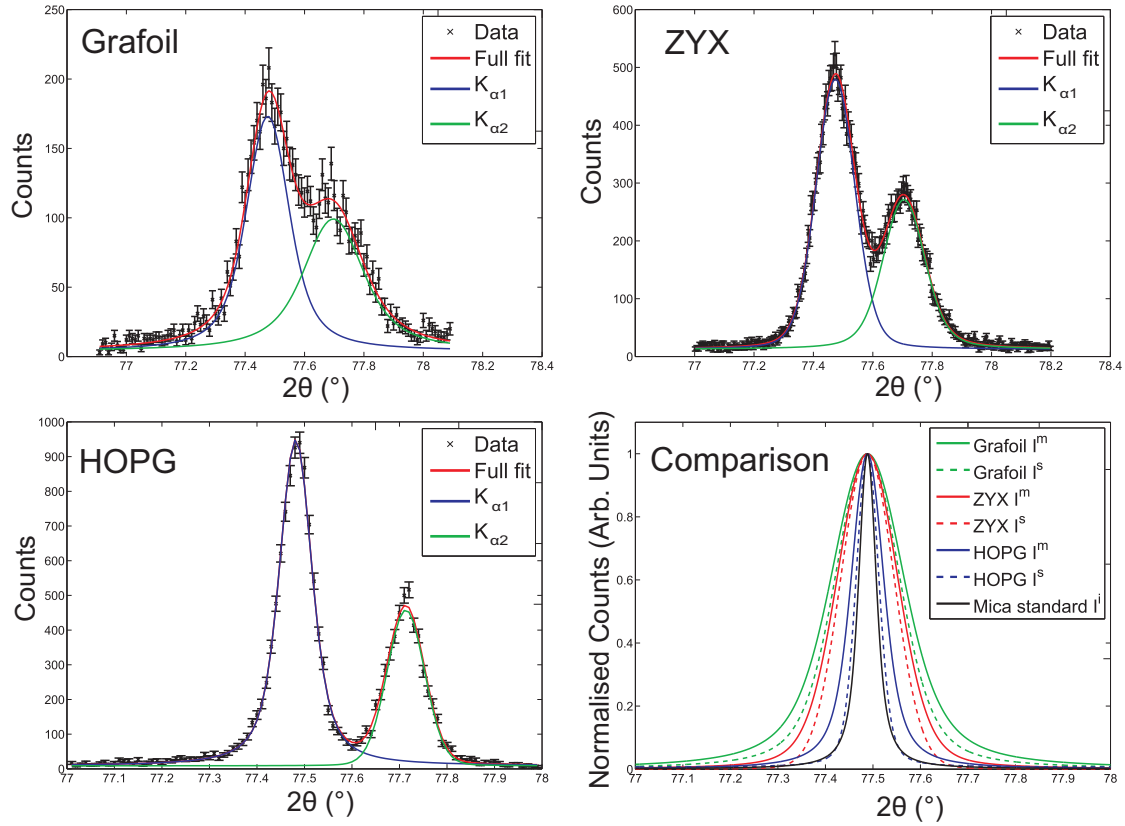

Figure 4.7: (110) diffraction peaks obtained from Grafoil, ZYX and HOPG. The bottom right panel is a comparison of normalised Voigt functions which have been fitted to the $K_{\alpha1}$ (110) peak for Grafoil, ZYX and HOPG. The resolution recording obtained from the mica has also been included. The width parameters for these curves are given in table 4.2

The Grafoil measurement can be seen to have the smallest peak size in terms of the counts measured; this is unsurprising given that the 150 μm thickness of the Grafoil means that the total mass of Grafoil sample in the diffracting volume is less than in the ZYX or HOPG measurements. Similarly, the lower counts of the ZYX compared to the HOPG can be attributed to the lower density of the ZYX, which is approximately quarter that of unexfoliated graphite.[2]. Due to the different thickness

[2]The bulk density of Grafoil is taken to be 0.9 - 1.1 g/cm^3 and ZYX has a density of approximately 0.5 g/cm^3 [69, 73], values which were crudely confirmed by us using a micrometer. The density of graphite is 2.2 g/cm^3

and densities of these samples, the scan time for the Grafoil and ZYX samples was 24 hours compared to only 4 hours for HOPG.

By using these long measurement times, sufficient counts have been obtained which then allows for the (110) to be modelled as the sum of two Voigts, one for each peak of K_α doublet. Figure 4.7 also shows a comparison of Voigt fits to the $K_{\alpha 1}$ (110) peaks obtained from Grafoil, ZYX and HOPG alongside Voigts which have been constructed using the instrument corrected width parameters, f_g^s and f_l^s.

Sample	f_g^m	f_l^m	f_v^m	f_g^s	f_l^s	f_v^s
Grafoil	0.1449	0.0889	0.1983	0.1427	0.0598	**0.1774**
ZYX	0.1323	0.0338	0.15132	0.1299	0.0047	**0.1324**
HOPG	0.0542	0.0448	0.082	0.0478	0.0158	**0.0568**
Mica	0.0254	0.0291	0.0443	-	-	-

Table 4.2: Voigt width parameters

The fits shown in the bottom right panel of figure 4.7, along with their respective width parameters shown in table 4.2 reveal that the hierarchy of broadening in the samples is as expected; the Grafoil (110) peaks are the broadest whilst both HOPG peaks are the narrowest, confirming our previous suppositions about the crystallinity of these samples. Lacking any means by which to remove strain contributions, we assume that all sample broadening is due to finite crystallite size and that therefore the Scherrer equation can be applied. Substituting the f_v^s values from table 4.2 into equation 4.6 calculates the crystallite sizes of the Grafoil, ZYX and HOPG samples to be 650 Å, 800 Å and 1870 Å respectively.

It is informative to compare these crystallite sizes to those obtained in the literature, though it should be noted that line broadening techniques applied to graphitic samples have received surprisingly little attention in the literature. For the graphitic

substrates Grafoil, Papyex and ZYX much of this data has been collated in table 2.1 in section 2.3. For non-exfoliated graphite samples, there is even less data, with the works by Guentert [133], Hirai [134] and Morant [135] seem to be the extent of available literature.

Our estimate of 650 Å for the crystallite size of Grafoil is somewhat larger than the 400 Å value obtained by Vora *et al.* [26] using neutron diffraction. It should be noted however that no specifics of the line broadening analysis is given so it is unclear whether our methods are directly comparable. Gilbert et al. [74] on the other hand have applied a similar Scherrer analysis to the (110) diffraction line from Papyex to obtain an estimate for L_a of 600 Å, which is similar to the value obtained here. Several (110) measurements of Grafoil were made, and the broadening observed consistently produced crystallite estimates of 600 - 700 Å.

The crystallite size estimate of 1870 Å for the HOPG sample is somewhat consistent with the work of Morant [135], who performed a modified Scherrer analysis on (110) reflections obtained from pyrolytic graphites deposited at a variety of temperatures. Morant discusses the unique problems of performing line broadening analysis on graphite samples, particularly with regard to the difficulties in removing strain broadening contributions due to the lack of higher order reflections in the $(hk0)$ lines. The strain contributions are assumed to be due to defects and stacking faults, and by applying the stacking fault correction factor of Wilson [136] estimated by analysis of the (112) diffraction line the strain contribution is removed from the (110) line. Morant uses this modified method to estimate a typical L_a crystallite size of approximately 3 μm for the most crystalline sample. As was noted earlier, the resolution profile of the instrument, I^i can be interpreted as an upper limit on the size of crystallites that can be estimated. The results of Morant can be put into perspective by inverting the Scherrer equation to estimate the peak width produced by a sample composed of 3 μm crystallites whilst assuming all other (strain, instru-

ment) broadening contributions are neglected. Performing this calculation results in a peak width of 0.0035°. For context, the minimum step-size of our diffractometer is 0.002°, so this deduced crystallite size is deemed to be somewhat unrealistic. If this strain correction is then ignored, the broadening observed by Morant in the (110) is consistent with L_a sizes on the order of 1000-4000 Å, which is in line with our observation of 1870 Å. Multiple scans of the (110) peak from HOPG give crystallite estimates that range from 1320 - 1870 Å.

Our L_a size estimate of 800 Å for the ZYX is somewhat troubling; it is significantly smaller than the 3000 Å value which is given in table 2.1, section 2.3 which was obtained by Birgeneau and co-workers [6]. As with Grafoil, multiple scans of the ZYX (110) were made, with the broadening in each being consistent with 790 - 840 Å sized crystallites. This obviously does not match up with the established literature describing a substrate which has a surface coherence length on the order of 2000 Å. There are several explanations for this discrepancy, and as in the case of the HOPG sample, it is likely that strain within the sample contributes significantly to the observed line broadening, which given that we have only one ($hk0$) order of reflection to work with unfortunately means this strain cannot be removed reliably. In a sample such as ZYX which has undergone exfoliation and then subsequent compression, it seems reasonable that strain would be a prominent contributor to broadening.

Another important factor to consider is the sample orientation that is used by Birgeneau and others to obtain 2D (hk) peaks from adsorbed monolayers; in our measurements the (110) reflections are obtained by scattering in transmission such that the X-ray radiation is incident perpendicular to the basal plane orientation of the graphite sample. During a tentative monolayer scattering measurement under the supervision of Dr Stuart Clarke from Cambridge which is discussed in section 4.6, we later learnt that the preferred geometry for obtaining (hk) diffraction lines is to

orientate the sample so that the radiation is incident into and along the basal planes i.e. the basal planes of the substrate lie parallel to y-z plane of the diffractometer. This geometry will be discussed further in the conclusion of this thesis, however the key point is that an y-z mounted sample will allow larger crystallites to contribute to the powder peak intensity, particularly when the sample is spun to improve averaging. Conversely, an x-z mounted sample will have a tendency to be weighted to measuring the smaller crystallites in the sample.

It is also important to note that many authors such as Birgeneau and Vora do not venture any detail whatsoever the method used to determine the L_a dimension of the substrate crystallites, though it appears likely that this size is determined by the Half Width Half Maximum (HWHM) of a diffraction peak as measured in $q = 4\pi \sin\theta/\lambda$, which is a good approximation for small crystallites but becomes invalid as the crystallite size is comparable to the instrumental resolution. For this reason, the values of 400 Å and 3000 Å for Grafoil and ZYX may simply not be comparable to the results shown in figure 4.7.

Despite the difficulty in corroborating with values available in the literature via this new crystallite method, it was felt that it still had value as a comparative method; it can be assumed that strain is an undesirable by-product of the exfoliation process and should also be minimised in any new substrate. The line broadening in the (110) can then be taken as a general indicator of crystallinity in the substrate, and the manufacturing process was then modified so as to produce minimal (110) line broadening.

Prototype substrate foils were thus measured using the method outlined in this section, and the width parameters then compared to those obtained for Grafoil, ZYX and HOPG samples, which are taken as benchmarks. Extra care had to be taken during handling, as our samples were often quite delicate and fragile in comparison to the benchmark samples. Figure 4.8 shows (110) scans obtained for two prototype

substrates exfoliated under different conditions. The prototype foil 4H had been exfoliated at a temperature of 700°C under vacuum in a quartz glass tube using 0.1 g of GIC taken from batch 4. The sample was left for 12 hours to remove excess intercalant. The foil 9B was made by exfoliating 0.15 g of batch 9 GIC at 190°C under vacuum in a metal tube for 12 hours. This sample was then ramped to 700°C at a rate of 0.5°C/min to remove excess intercalant. Both samples were compressed into foils using the same nominal pressure of 180 bar.

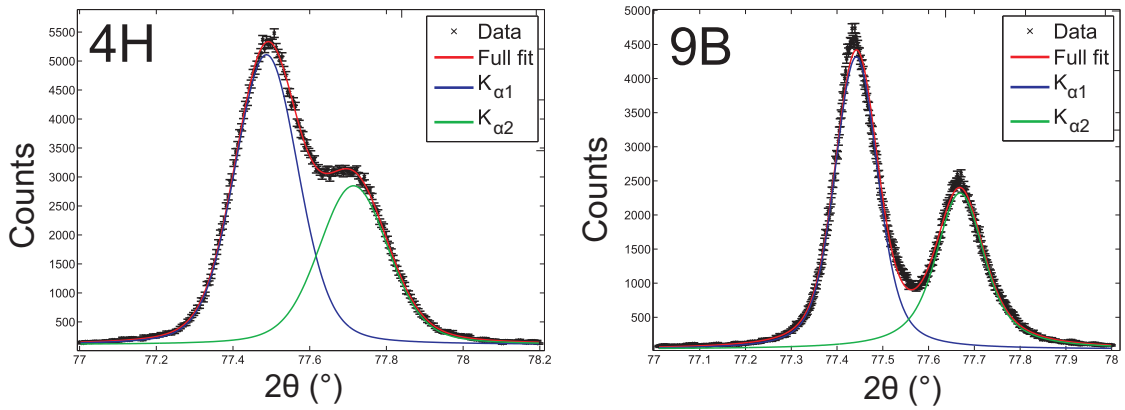

Figure 4.8: (110) diffraction peaks obtained from prototype foils 4H and 9B

These two peaks obtained from samples exfoliated under different conditions support the supposition that exfoliating at lower temperatures produces substrates with greater crystallinity; the K_α doublet obtained from the 9B foil is clearly resolved, whilst broadening causes significant peak overlap in the 4H sample. Using the corrected widths, f_v^s from table 4.3 in the Scherrer equation estimates the crystallite sizes to be 600 Å and 1200 Å for 4H and 9B respectively.

Sample	f_g^m	f_l^m	f_v^m	f_g^s	f_l^s	f_v^s
4H	0.1727	0.0404	0.1953	0.1708	0.0113	0.1769
9B	0.087	0.041	0.111	0.0832	0.0119	0.0898

Table 4.3: Uncorrected and uncorrected Voigt width parameters for foils 4H and 9B

4.1.6 Summary

Using the method described in the preceding sections, the prototype substrate have been characterised by the broadening in their (110) diffraction lines. These lines are fitted, and corrected for instrumental broadening using the deconvolution relations in equations 4.17,4.16 and 4.22. The resultant width can then be interpreted directly as an indicator of crystallinity or input into the Scherrer equation to obtain an estimator of crystallite size which ignores strain contributions. The results of these measurements are shown in table 4.6, and a detailed discussion presented in section 4.6. A table is given in appendix B which gives the fit parameters to the (110) diffraction lines that were successfully obtained from prototype substrates.

With the crystallinity of the prototype characterised, samples could then be transported from UCL to RHUL for surface area characterisation. This was achieved using krypton vapour pressure isotherms, and is discussed in the next section.

4.2 Adsorption: Surface Area Measurements

The primary focus has been to produce a highly crystalline substrate, upon the assumption that this would necessarily accommodate much larger surface coherence lengths. As has been discussed in section 3.5, it was surmised that this would compete with the requirement of substrate surface area. The calculation of the signal to noise of a hypothetical SQUID-NMR experiment found in the same section indicates that the value 1 m^2/g represents a reasonable lower limit for a substrate to still produce an observable ^{3}He NMR signal. Any promising substrates with large crystallite sizes would then need to be characterised to check that they satisfied the surface area requirements.

The phenomenon of physical adsorption has been introduced in section 1.1, as has the notion of an adsorption isotherm whereby the amount of gas adsorbed by a substrate is calculated as a function of the recorded vapour pressure above it. Adsorption isotherms can be used to infer properties about the adsorbed film and by extension the adsorbing substrate. Undoubtedly, the most widespread application of the adsorption isotherm is as a means of determining the substrate surface area. For example the type II and type IV isotherms which are shown in figure 1.2, section 1.1 are typical of gas adsorption by industrially useful adsorbents like carbon black. Such isotherms can then be interpreted using the Brunauer, Emmett an Teller (BET)[137] equation to obtain an estimate of the adsorptive capacity of a material, which can be loosely interpreted as a surface area.

The standard method of determining the surface areas of graphitic substrates is to perform nitrogen or krypton isotherms at 77.3 K [138, 69]. Various features in the recorded isotherm can be related to well understood physical phenomenon which allows the surface area to be determined very accurately and therefore to define a coverage scale for the graphite surface.

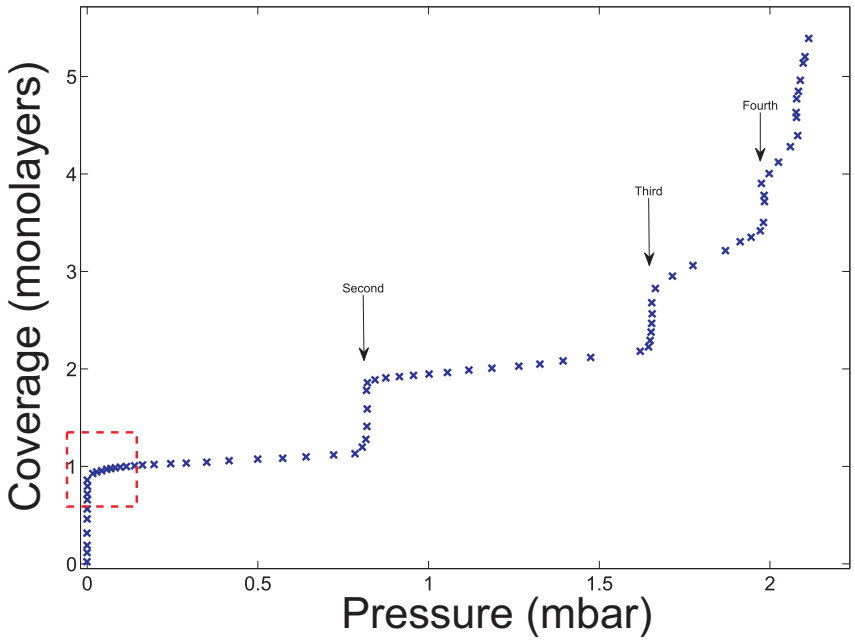

Figure 4.9: Adsorption isotherm of Krypton on an exfoliated graphite adapted from [20], displaying distinct 'steps' which indicate layer by layer formation. Features indicative of 2D phase transitions can be seen by detailed inspection of the region enclosed by the red box.

As is discussed in section 1.2, simple gases like nitrogen and krypton will adsorb onto the graphite (001) faces layer by layer displaying a characteristic stepwise, type VI isotherm such as the one shown in figure 4.9, where each 'step' represents the formation of a distinct layer which is only one atom or molecule thick. If the graphite substrate is particularly homogeneous, a small 'sub-step', similar to that shown in figures 4.10 and 4.11, can be observed in the monolayer-to-bilayer region of the isotherm.

Scattering studies [25, 6] performed *in-situ* on adsorbed monolayer films as they are grown epitaxially, were used to show that simple gases adsorbed onto graphite can exist in a variety of states that are 2D analogues to bulk phases of matter. Phase diagrams, such as those shown in figures 4.10 and 4.11 were proposed for these adsorbed systems. The sub-steps that can be seen in nitrogen and krypton

adsorption isotherms are then attributed to the phase transitions that occur within the film as the coverage is increased.

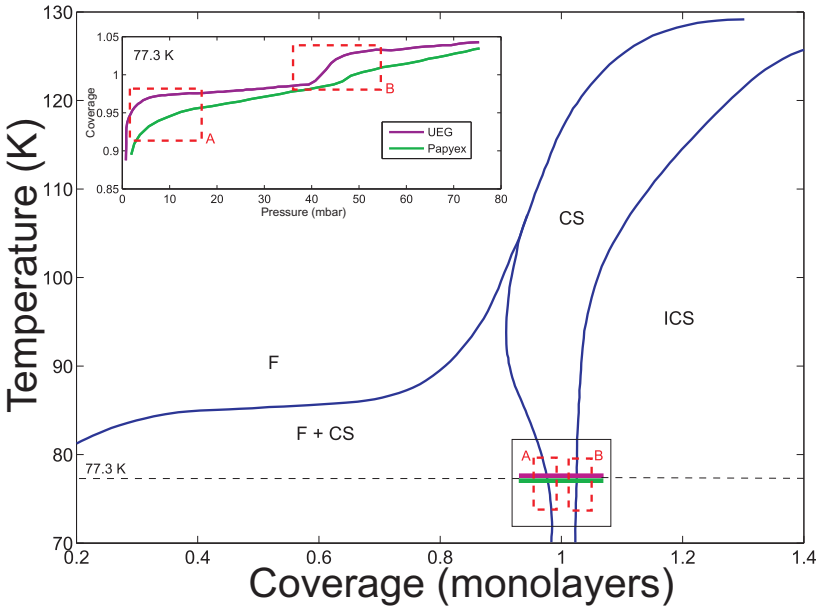

Figure 4.10: Phase diagram of krypton on graphite, adapted from [6]. The inset which is adapted from [70] shows the sub-step that occurs in the isotherm due to phase transitions within the film. The labels F, CS and ICS denote Fluid, Commensurate Solid a Incommensurate Solid respectively. The boxes A and B are discussed in the text.

As can be seen by their phase diagrams, the nature of the sub-step in the nitrogen and krypton isotherms are very similar, though subtle differences exist. At 77.3 K, the first layer of krypton on graphite co-exists as 2D-fluid with a $\sqrt{3} \times \sqrt{3}$ commensurate solid for most coverages. During this co-existence, the isotherm pressure remains low and constant at approximately 0.5 μbar. Near monolayer completion, the fluid freezes out leaving only the commensurate solid (C-solid) in its place. This transition can be seen in the isotherm as an increase in the observed pressure, which is highlighted by the region A in figure 4.10. The C-solid persists for a short range of coverages, as remaining vacancies in the solid become occupied. The C-solid then continuously transitions into an incommensurate solid (IC-solid), which is marked

by the distinctive sub-step in the isotherm at region B. As can be seen from the isotherm inset, the sub-step is considerably suppressed in the Papyex in comparison to the UEG (uncompressed exfoliated graphite) sample. This is attributed to the reduction in surface coherence lengths that occurs when Papyex is compressed from the UEG precursor.

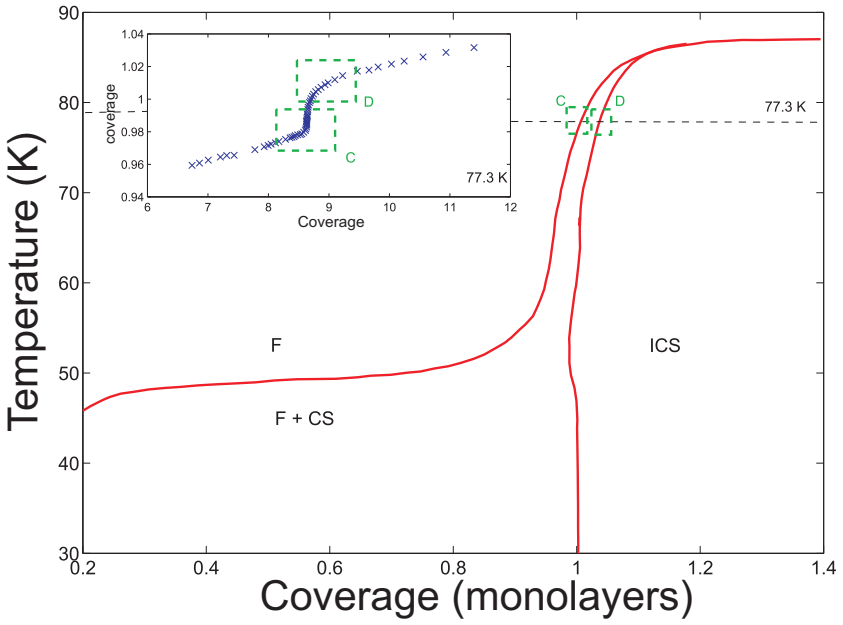

Figure 4.11: Phase diagram of nitrogen on graphite, adapted from [6]. The data shown in the inset is an adsorption isotherm performed on one our prototype substrate.

The sub-step that is seen in the nitrogen isotherm near monolayer completion occurs due to the film transitioning from a 2D fluid to a co-existence between a 2D fluid and a $\sqrt{3} \times \sqrt{3}$ density commensurate solid. As the coverage is increased through this region, the commensurate component grows until the monolayer is fully solidified, at which point the film transitions into an incommensurate solid. The fluid-coexistence and commensurate-incommensurate transitions can be seen in the adsorption isotherms in the regions marked C and D respectively.

In both krypton-graphite and nitrogen-graphite isotherms, these sub-steps are

intrinsically linked with the formation of a commensurate solid on the graphite surface. As can be seen from the $\sqrt{3} \times \sqrt{3}$ schematic in figure 1.5, section 1.2, the bound molecules form a triangular lattice, with each molecule occupying the centre of every third graphite hexagon. Each molecule can then be considered as occupying 15.71 Å^2, which naturally leads to a very precise means of determining the substrate area.

Given that many simple gas-graphite monolayer systems are commensurate just before the formation of the second layer, it is a common convention to define the coverage scale in terms of the commensurate density, and isotherms and phase diagrams are then presented with the coverage expressed in units of commensurate monolayers, as can be seen in figures 4.9-4.11. It should be noted that some uncertainty can exist in defining this scale; the sub-steps are closely associated with $\sqrt{3} \times \sqrt{3}$ formation, but the point at which the monolayer is *fully* commensurate is not clear from the isotherm. That being said, it is generally accepted that nitrogen and krypton isotherms allow the surface area of graphitic substrate to be characterised to within 5 %. The next section outlines the experimental procedure to obtain a successful isotherm.

4.2.1 Adsorption Procedure

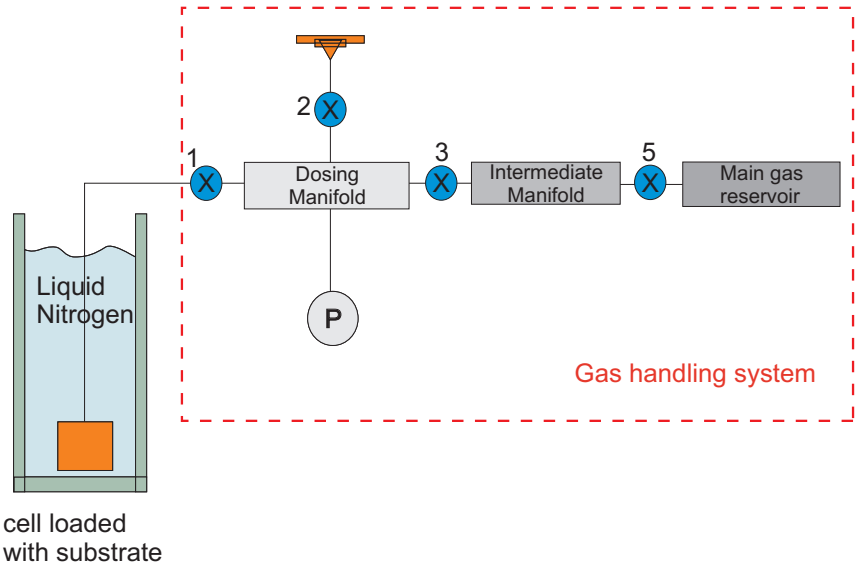

Figure 4.12: The basic adsorption isotherm apparatus consists of a dewar which can be filled with liquid nitrogen, a simple copper cell which holds the sample along with spacers which serve to minimise the dead volume. This is then be connected by a fill line to the gas handling system. The gas handling system shown in this diagram is a simplified schematic of that shown in figure 5.4

The apparatus used for performing vapour pressure isotherms is shown in figure 4.12. Operation is simple; a substrate foil is out-gassed at >500°C under vacuum to remove moisture and surface contaminants. The out-gassed foil is loaded into the copper cell which is then sealed with an indium gasket. The cell and gas handling system up to valve 5 is then evacuated using a turbo-pump attached to the KF-16 port at valve 2. The whole apparatus is then checked for leaks using a leak detector which can be attached to the turbo-pump. During the cell loading process the sample is briefly but unavoidably exposed to air for several minutes. It is therefore necessary to leave the cell and gas handling system evacuating for at least 12 hours to remove any moisture that was adsorbed onto the foil or that has been introduced

into the gas handling system during the cell loading.

Once this evacuation is finished, all valves of the gas handling system are closed and the pump is removed. The cell is then immersed into liquid nitrogen, bringing the temperature of the sample to 77.3 K. Gas can then be admitted into the dosing manifold from the reservoir using the manifold between valves 3 and 5 as an intermediary gas storage. The volume of the dosing manifold enclosed by valves 1,2 and 3 has been previously measured by Dr. Jan Nyeki using helium volume sharing and was found to be 1.80 ± 0.01 cm^3. The gauge at P is a Paroscientific [139] quartz transducer which is able to measure the pressure in the dosing volume whilst simultaneously measuring the ambient temperature. Knowing the volume, pressure and temperature of the gas in the dosing manifold means that the total number of atoms/molecules can be calculated using the ideal gas equation. This known quantity of gas in the dosing manifold is referred to as a 'shot' of gas, which is slowly bled through valve 1 allowing the gas to then be adsorbed onto the surface of the graphite foil. Once the pressure reaches equilibrium, valve 1 is closed and another shot of gas can be admitted into the dosing manifold. The isotherm process is then simply a succession of admitting known quantities of gas to the cell and recording the subsequent pressure. Figure 4.13 shows the fundamental vapour pressure isotherm of the pressure as a function of the amount gas admitted to the sample.

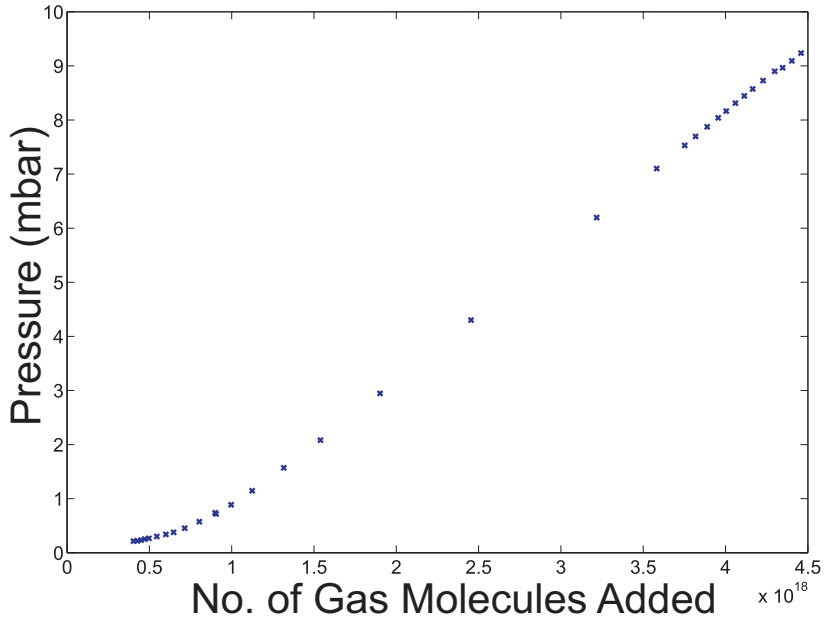

Figure 4.13: Nitrogen isotherm of an uncompressed exfoliated sample; pressure as a function of the amount of gas admitted.

In this form, the isotherm is not complete as corrections need to be applied to this data to account for the transpiration effect and the amount of molecules in the vapour phase, referred to as the dead volume of the apparatus.

The transpiration effect describes the phenomenon whereby two volumes at two different temperatures connected via a narrow tube will display different pressures. This only occurs at low pressures when the mean free path of the gas in the higher temperature volume is several times greater than the connecting tube diameter. In the apparatus of figure 4.12, the pressure in the dosing volume (which is at room temperature) will be slightly higher than in the cell. To correct for this we applied the expression of Takaishi and Sensui [140];

$$\frac{(P_1/P_2)-1}{\sqrt{T_1/T_2}-1} = \frac{1}{AX^2+BX+C\sqrt{X}+1} \tag{4.23}$$

Where P and T are the pressure and temperature and the subscripts 1 and 2 denote

the cell and dosing volume respectively. The coefficients A, B and C are gas specific constants and are given in the appendix. The quantity X is equal to $2P_2d/(T_1+T_2)$ where d is the diameter of the connecting fill line, which was either 0.76 mm or 1.3 mm, depending on the apparatus used. This is a small effect and is only important at pressures below 1 mbar; for a measured pressure of 0.215 mbar in the dosing volume, the transpiration corrected pressure in the cell is calculated as being 0.190 mbar. This correction then becomes less and less significant at higher pressures; for a reading of 8.966 mbar in the dosing volume the corrected pressure in the cell is 8.964 mbar.

When gas is admitted to the cell through valve 1 to the sample it is either adsorbed onto the substrate surface or it exists as a vapour in equilibrium with the film above the sample. As the molecules in the adsorbed film do not contribute to measured pressure and are assumed to have negligible volume, it is possible to calculate the number of adsorbed molecules, N_{ads} by the expression;

$$N_{ads} = N_{add} - N_{vap} \tag{4.24}$$

Where N_{add} is the number of molecules added to the cell and N_{vap} is the number of molecules present in the vapour phase above the sample. As shown in figure 4.13, N_{add} is simple accountancy; each shot of gas from the dosing manifold adds more molecules which can be calculated using the ideal gas equation. N_{vap} is calculated in a similar way; due to the low pressures, the vapour can be assumed to be an ideal gas [20] which then occupies the 'dead volume' of the isotherm apparatus which includes the sample cell, the fill line and the dosing manifold. N_{vap} can then be calculated from the measured value of the dead volume.

The *effective* dead volume can be accurately characterised by volume sharing of helium gas from the dosing manifold once the isotherm is completed, however

it is necessary to first remove the adsorbate gas in the isotherm apparatus using a turbo-pump. This can be aided by partially lifting the cell out of the liquid nitrogen so as to desorb the adsorbed film. Pumping on the apparatus for 20 minutes in this manner is sufficient to remove most of the adsorbate. Once this is done, all valves are closed and the cell is re-immersed in the liquid nitrogen. The dosing manifold is loaded with helium which is then allowed to expand through valve 1 into the fill line and cell, the subsequent pressure is recorded and used to calculate an effective room temperature dead volume for the apparatus.

Typical dead volumes ranged from 6 - 20 cm^3, depending on how many spacers were in the cell. Figure 4.14 shows a plot of number of adsorbed atoms as a function of pressure which is obtained after applying both transpiration and dead volume corrections to the data in figure 4.13. The axes have been swapped so that pressure is on the horizontal in line with literature convention.

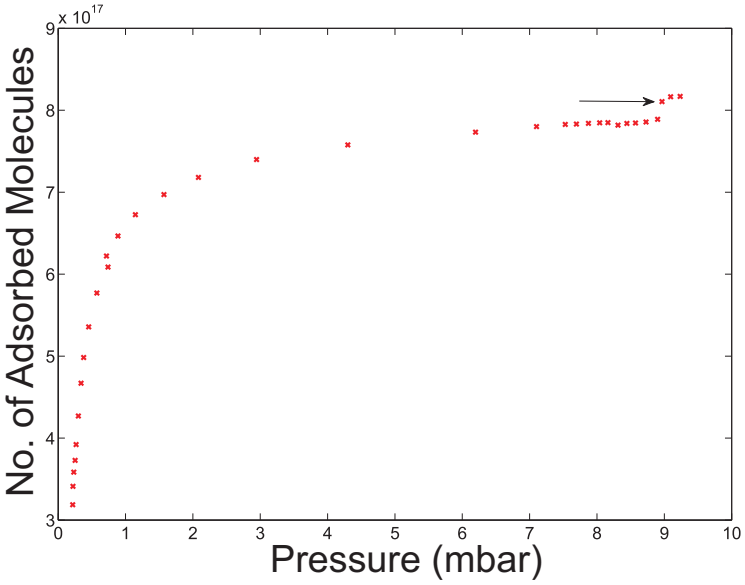

Figure 4.14: Nitrogen isotherm of an uncompressed exfoliated sample complete with dead volume and thermomolecular pressure corrections. A sub-step is clearly visible at 9 mbar which demarcates the point at which the $\sqrt{3} \times \sqrt{3}$ commensurate solid forms and which also indicates the completion of the first nitrogen monolayer. The dead volume for this isotherm was 16.07 cm^3 at room temperature.

Interpreting figure 4.14 is simple; the sub-step at 9 mbar indicates that the film state is a co-existence of a fluid with a commensurate. Where the sub-step ends, as indicated by the arrow, it is assumed that the film has solidified completely, with the substrate being fully coated in $\sqrt{3} \times \sqrt{3}$ solid.

At this point, there are 8.106×10^{17} adsorbed N_2 molecules, with each molecule occupying 15.71 $Å^2$. The total surface area of this substrate is then 0.1273 m^2, which for 0.0678 g of sample gives a specific area of 1.88 m^2/g.

By comparing figures 4.13 and 4.14 it can be seen that more than 80% of the N_2 molecules are in the vapour phase. This presents a problem when measuring samples with small total surface area, as can be seen from equation 4.24, the error in determining N_{ads} will be dominated by the error in determining N_{vap}. Thus if the dead volume is not accurately characterised this translates directly as an error in the surface area determination.

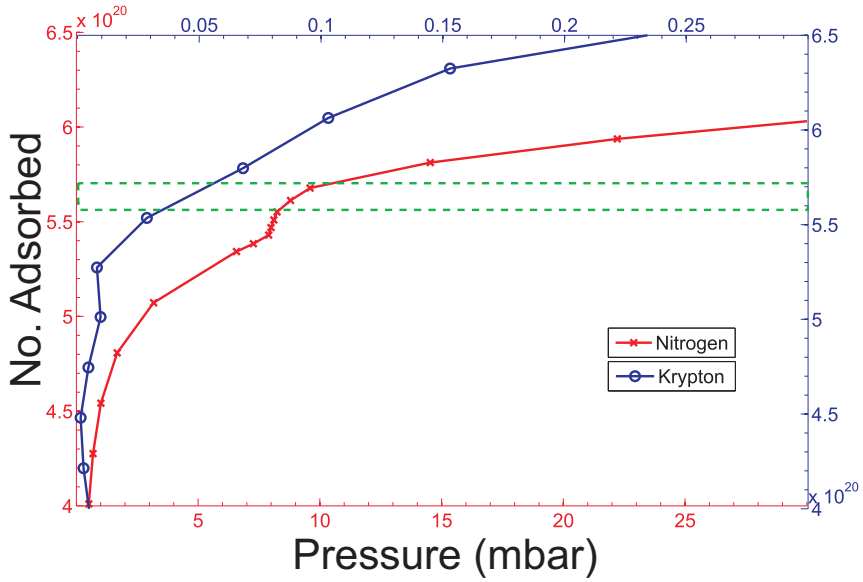

Figure 4.15: Comparison of krypton (blue) and nitrogen (red) isotherms which were performed on the same Grafoil sample. The data has been enlarged in the region where the sub-steps should occur. The total surface area calculated from this measurement was 86 ± 2 m^2. The dead volume was 10.0 ± 0.2 cm^3. The region enclosed by the green dotted highlights where commensurate density is thought to occur.

In principle, using krypton isotherms as a means of determining surface area should be more accurate as the krypton sub-step feature is seen at a lower pressure. This means that there are fewer atoms in the vapour phase and any dead volume errors are mitigated. Figure 4.15 shows the comparison between a nitrogen and krypton isotherm that was performed by Frank Arnold on a 'ballast cell' which contained several grams of Grafoil which had been subjected to diffusion bonding (section 4.7). The advantage of this measurement was the large total surface area of the sample and small dead volume which meant that for both measurements $N_{vap} << N_{ads}$ making this a very accurate surface area characterisation.

The sub-step indicated phase co-existence can be seen clearly in the nitrogen isotherm, however no sub-step is visible in the krypton isotherm. It is clear that

the krypton isotherm in figure 4.15 does not have sufficient resolution to observe a sub-step which is likely suppressed to some extent as it is in Papyex. As the inset in figure 4.10 shows, the sub-step can be seen in both Papyex and UEG samples at 40 - 50 μbar. Comparing the krypton and nitrogen isotherms we see that the 40-50 μbar region of the isotherm lines up with the the end of the nitrogen sub-step. Using this as a justification, we therefore assume that commensurate density occurs in the krypton isotherm at 50 μbar. Figure 4.16 shows a krypton isotherm that was performed on the prototype substrate foil 4H. The surface area is calculated for this foil by interpolating from 50 μbar to obtain the number of atoms adsorbed at this point in the isotherm. As was done in the analysis of figure 4.14, the film is assumed to be commensurate with each atom having an effective area of 15.4 Å^2. This leads to a total foil area of 0.33 m^2, which for a 81.5 mg foil gives 4.15 m^2/g.

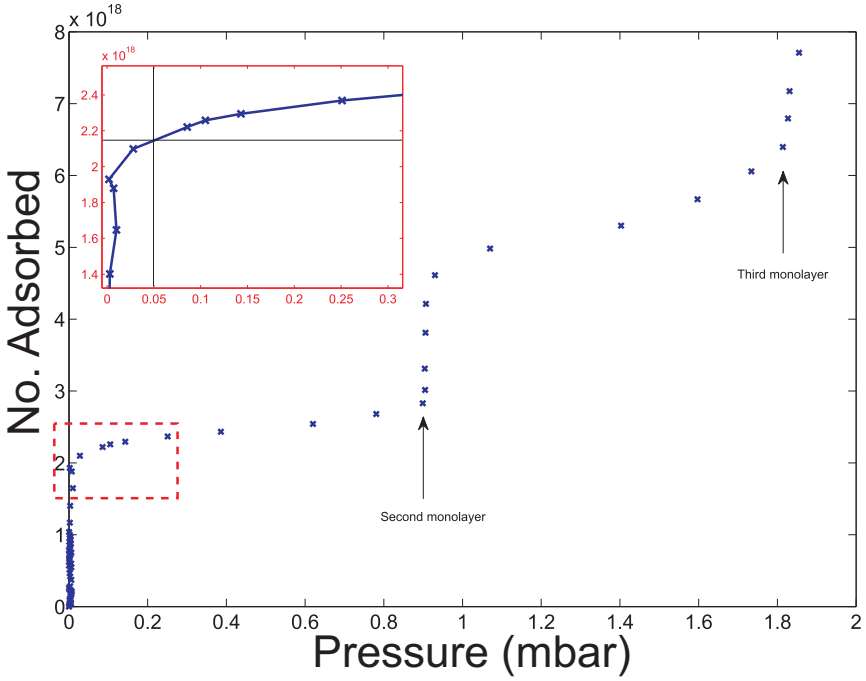

Figure 4.16: Krypton isotherm of a prototype substrate, which was pressed from graphite exfoliated at 700° C. The specific area of this substrate was 4.20 m^2/g. The dead volume in this measurement varied between 10.2 and 10.4 cm^3

It is interesting to investigate the effect of dead volume errors on the surface area estimate obtained from this adsorption isotherm. From calculation we find that at 50 μbar there is approximately 2.18×10^{16} krypton atoms in the vapour phase for a dead volume of 10.3 cm^3. This is a factor of 100 fewer than the number of krypton atoms that are adsorbed onto the substrate surface. Providing that our assumption of commensurate density at 50 μbar is correct, then a 100 % error in determining the dead volume for this measurement results in only a 1 % error in the surface area determination. The main source of error then simply becomes the resolution of the isotherm in the region surrounding 50 μbar.

Using this krypton isotherm method we have successfully measured samples with total surface areas as small as 0.02 m^2, though typically our samples presented surface areas of 0.1 m^2 or greater. The results of these surface area measurements are presented in table 4.6. Performing isotherms on our own samples of Grafoil and ZYX revealed their specific areas to be 18.3 m^2/g and 1.95 m^2/g respectively, which is in agreement with the literature values [69]. It should be noted that whilst performing nitrogen isotherms on our sample of ZYX, strange oscillating pressure behaviour was seen near commensurate density. This is discussed in further detail in section 4.26.

The primary disadvantage of this method is its time intensive nature; the isotherm apparatus is unfortunately not automated and shots of gas were admitted into the adsorption cell by opening and closing valves by hand. Additionally, each data point in figure 4.16 could take perhaps twenty minutes to equilibrate, though often this was as long as two hours. This means that only a fraction of the all the prototype substrates that were manufactured had their surface areas characterised.

As has been mentioned in the adsorption procedure, before loading the prototype substrate foils into the copper adsorption cell, it was customary to subject the sample to a moderate heat treatment of 500°C under vacuum for 8 - 12 hours to

remove common surface contaminants. During these heat treatments we noticed that those substrate foils that had been manufactured from low temperature exfoliations displayed a tendency to disintegrate during this preparatory heat treatment. As is discussed in section 4.3, subjecting the exfoliated samples to heat treatment at 700°C is not sufficient to completely remove all the potassium intercalant, and it was thought that the foils were disintegrating as a result of further exfoliation taking place. This hypothesis was ruled out when it was shown that exfoliated samples that had been subjected to temperatures (1000°C) sufficient to remove all the intercalant, would form foils that would still disintegrate when heated. The exact temperature is not known, but it appears that this behaviour is only seen in samples exfoliated at low temperatures, in particular all samples exfoliated at temperatures below 250°C showed evidence of this disintegration on reheating. In section 4.7, which describes the diffusion bonding process, it is shown that this disintegration can be prevented provided that the foils are compressed during heating.

4.3 Purity Analysis

As is covered in section 3.1.1, it was originally intended that Kish was to be the starting graphite for the new RHUL exfoliated graphite substrate. The PPMS measurements described in section 3.1.2 show that even after acid washing and heat treatment at 1000°C, the kish graphite showed evidence of increased magnetic impurities relative to Grafoil, precluding it as a substrate source material.

This raised the broader issue of how best to assess the purity of prototype substrates, which should contain as few impurities as possible, especially those which could interact with the ^{3}He nuclei during a low temperature NMR experiment. Having no means of performing quantitative measurements ourselves, purity analyses were conducted externally by Dr. Nathalie Grassineau of RHUL earth sciences and by Evans Analytical Group (EAG) at one of their subsidiary laboratories in Tournefeuille, France. EAG is a company that specialises in analytic measurements for industry.

The first sample analyses took place at the RHUL earth sciences analytical laboratory using Atomic Emission Spectroscopy (AES). This technique is performed by taking the sample and 'digesting' it in a strong acid. The resulting solution is then sprayed into a flame, wherein the elements in the spray will emit their characteristic atomic spectra. The intensity of each of these spectra is related to the concentration of that element in the sample. Three samples; kish, Madagascan flake and 'exfoliated batch 7 (EB7)' were characterised using this method. The kish sample was composed of >0.5 mm flakes which had been obtained through sieving, with the sample undergoing no other treatments. The Madagascan flake sample required no sieving, however it was subjected to out-gassing at 500°C to remove common contaminants. The EB7 had been made by exfoliating the entirety of GIC batch 7 at 700° under vacuum, where it was left for 12 hours in an attempt to remove all the potassium intercalant. The results of the purity analysis for these samples are

given in table 4.4

It was hoped that further samples could be characterised using the AES technique, however it was found that small graphite particulates in the acid digestion had lead to the catastrophic blockage of the spray nozzle, which then precipitated a complete overhaul of the AES instrument. This unfortunately meant that an alternative means of purity analysis was required.

A further two samples were therefore sent to EAG in France to be characterised via Glow Discharge Mass Spectrometry (GDMS). This technique works by exposing the sample to a discharge of accelerated argon ions. This then ablates the surface and the constituent atoms of the sample are liberated into the plasma phase. The make-up of this plasma can then be analysed via mass spectrometry, providing a direct measurement of the elemental composition. Two samples, which were designated as 'exfoliated batch 12 (EB12)' and 'exfoliated composite batch (ECB)' were sent to France for analysis. The results for these samples are presented in table 4.4, and specific details regarding sample histories of EB12 and ECB are given in the discussion.

4.3.1 Results and Discussion

Element	GTA[22]	kish	Mad. flake	EB7	EB12	ECB
Aluminium	47.28	2197.2	55.9	39.9	-	-
Antimony	-	-	-	-	0.05	0.05
Barium	0.82	20.7	5.6	3.4	0.11	0.6
Bismuth	-	-	-	-	0.05	0.05
Calcium	**58.88**	**11598.6**	**121.2**	**72.5**	**4.4**	**6.2**
Chlorine	-	-	-	-	0.74	0.7
Chromium	5.45	45.2	2.8	3.5	20	0.86
Cobalt	-	-	-	-	0.49	0.1
Copper	0.7	-	-	-	-	-
Iron	**190.8**	**82303.9**	**87.3**	**170.8**	**38**	**20**
Lead	-	-	-	-	0.73	0.05
Magnesium	40.3	3376.5	22.3	25.5	2	2.4
Manganese	8.07	2476	2.5	3.5	1.5	0.74
Molybdenum	**1.35**	-	-	-	**590**	**0.2**
Nickel	11.46	13.4	3.8	4.3	2.3	0.5
Phosphorous	-	107.6	1.9	3.8	1.4	8.5
Platinum	-	-	-	-	0.73	0.05
Potassium	**22.19**	**277**	**25**	**1987.2**	**2.9**	**4.2**
Silicon	**229.69**	-	-	-	**82**	**72**
Sodium	-	824.1	172.7	153.9	8.3	0.75
Strontium	0.61	16.3	0.5	0.4	0.05	0.05
Sulphur	-	-	-	-	16	4
Tin	18	-	-	-	0.05	0.05
Titanium	11.5	921.5	9.3	3.8	0.59	0.33
Vanadium	14.72	74.5	0.2	0.3	0.11	0.11
Zinc	2.16	15.1	0.8	1.5	0.32	0.33
Zirconium	6.76	-	-	-	0.19	0.16

Table 4.4: Purity Analyses of samples - data in pppm. Data in bold text is for clarity and referred to in the text. Purity data for Grafoil GTA is available from the manufacturer and is included as a benchmark for comparison.

The results for the kish sample are unsurprising and agree qualitatively with the PPMS data in figure 3.5, which shows that kish contains a large concentration of

magnetic impurities, thought the AES value of 82000 ppm is several times larger than the 14000 ppm obtained by the PPMS. Needless to say, these results justify our decision to forego kish as a substrate source material.

The Madagascan flake sample by contrast appears to be of a comparable purity to Grafoil GTA, where, with the exception of aluminium, calcium and potassium, the Madagascan flake appears to have a lower concentration of impurities across the range tested. With this result we were satisfied that the Madagascan flake was suitable as a source material for the new substrates, however it remained to be seen if we could remove all the intercalant from the sample after exfoliation. To this end we then submitted the EB7 sample for testing which showed that even at 700°C a significant amount of the potassium intercalant remained.

It was suspected that this potassium could be removed if the sample had been treated at a higher temperature. The EB12 sample that was analysed was made by exfoliating 1.5 g of GIC from batch 12 at 350°C under vacuum, before slowly ramping the temperature up to 700°C where it was left for 12 hours. Previous attempts to heat exfoliated samples to higher temperatures had caused the quartz glass reaction vessel to crack, and it is thought that potassium and quartz react at these high temperatures, gradually causing the reaction vessel to degrade. For this reason, the EB12 sample was then transported to RHUL where it was subjected to a second heat treatment at 1000°C under vacuum for 24 hours. The results in table 4.4 show that with the exception of chromium and molybdenum, the impurity concentrations in the EB12 sample are lower than Grafoil *and* the original Madagascan flake source material. Presumably because the exfoliation process expands the graphite structure so significantly, this then allows impurities deep within the Madagascan flake to escape during the heat treatment. The high molybdenum concentration in the EB12 sample has been attributed to the use of molybdenum crucibles that were used to contain the sample during the second heat treatment. Most importantly the results

of EB12 show that the potassium intercalant can be effectively removed provided the sample is heated to 1000°C.

The final sample to be characterised was the ECB sample. This sample was made by exfoliating GICs taken primarily from the remnants of batch 14 and 15. Approximately 2 g of this composite GIC was then exfoliated at 210°C under vacuum, using a stainless steel tube as the reaction vessel and a muffle furnace. After 12 hours, the temperature was ramped at 1°C/min to 700°C, dwelling for another 12 hours. This was then removed, and the ECB sample transported to RHUL where it was subjected to the same heat treatment as EB12; 24 hours at 1000°C under vacuum, with the exception that the molybdenum crucibles had been replaced by crucibles machined from high purity graphite. The purity results are clear; the potassium is effectively removed, no molybdenum is present due to the graphite crucibles, and no increase in metal impurities such as chromium, iron or nickel can be seen from performing the exfoliation in the stainless steel tube.

The procedure applied to the ECB sample represents an effective method of purifying our substrate samples. The Madagascan flake has a greater impurity than the the benchmark Grafoil GTA, and impurity concentrations can be decreased even further after the exfoliation process and subsequent 1000°C heat treatment at RHUL. It should be noted that most of the prototype substrate foils that were made were not subjected to this second heat treatment due to time constraint. Most exfoliated graphites were only subjected to moderate out-gassing procedures (700°C under vacuum) before being pressed into a foil, as it was assumed that this is sufficient to remove the majority of the potassium - this assumption is justified by the results of EB7, and any remnant potassium is thought not to affect the surface area or diffraction measurements.

4.4 X-rays: Rocking Curves

There are several ways to measure the mosaic spread of a substrate, and there is disagreement between methods, which are discussed in section 2.2.1. Rocking curves performed on the (002) reflection of graphite is the method that has been applied here. Not all manufactured samples were characterised with this method as the primary aim of this project was to produce substrates with large surface coherence lengths, and mosaic spread was considered a secondary concern. The measurements suggest that our samples display a range of mosaic spreads. Overall they appear to have smaller mosaic spreads than Grafoil, but larger than ZYX, which was considered to be acceptable for our purposes.

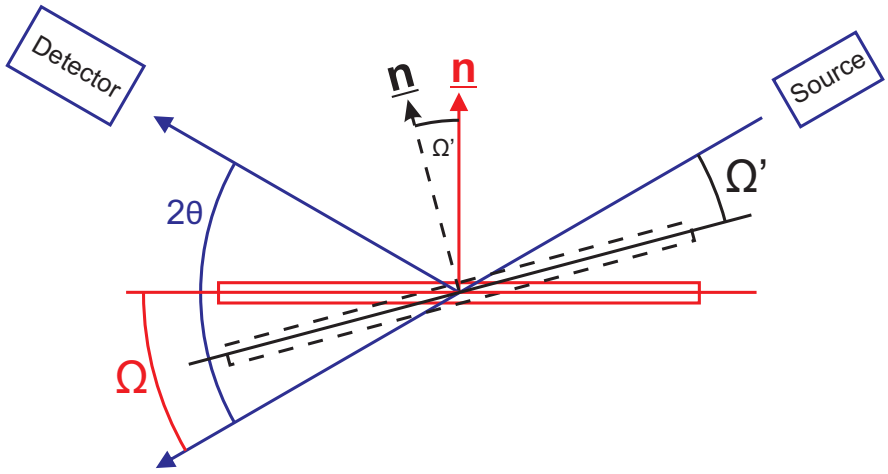

Figure 4.17: Basic rocking curve procedure; in a normal 2θ scan, the detector and source move in unison such that $\Omega = \theta$. Rocking curves measure the peak intensity as function of changing Ω only, by keeping the detector and source being fixed in position whilst the sample stage is 'rocked' back and forth.

The basic procedure for performing rocking is outlined in figure 4.17; a foil similar to those shown in figure 3.28 is laid flat on the diffractometer sample plate with the basal planes of the substrate parallel to the x-y plane of the diffractometer. The optics are aligned on the (002) reflection of graphite, which in the case of a

copper wavelength, of 1.540598 Å, is at 26.555° in 2θ. In a normal scan of 2θ, the x-ray source and the detector move in unison so that $\Omega = 2\theta$. In a rocking curve measurement, when the optics are aligned on the selected peak, the source and and detector are kept fixed and the sample plate is rotated or 'rocked' about the diffractometer (x) axis so as to perform a scan in Ω only. Performing a rocking curve on a selected (hkl) peak then records the intensity of that peak as function of Ω. Figure 4.18 shows representative data. The mosaic spread is then estimated by taking the direct FWHM of these curves.

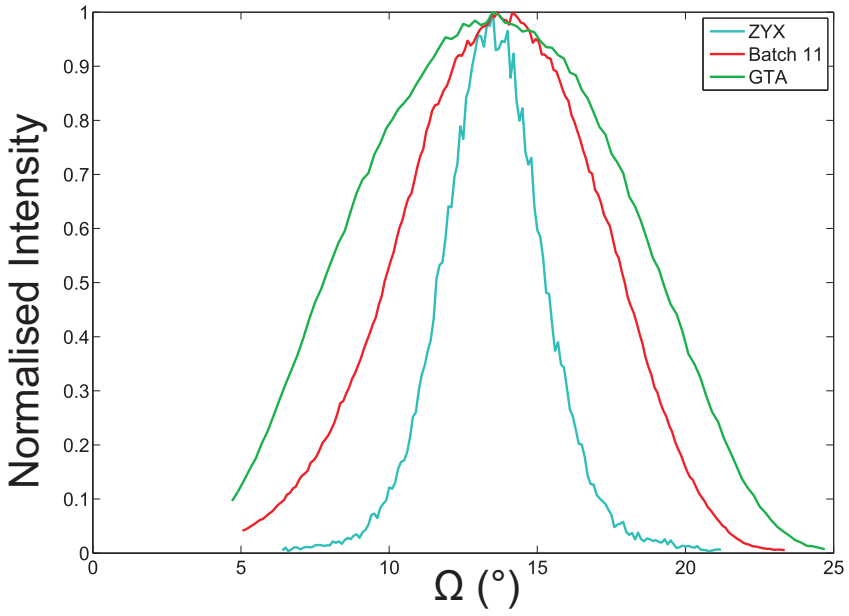

Figure 4.18: Comparison of rocking curves for ZYX, batch 11 and GTA Grafoil. The FWHM of the ZYX curve is 3.7° and for GTA the FWHM is 11.6°. The batch 11 foil displays a FWHM of 8.1 °.

The rocking curves on the X'pert pro diffractometers are limited to a full scan range of 20 ° in Ω, but as figure 4.18 shows, this is sufficient to obtain enough of the rocking curve to estimate a FHWM. The smallest FWHM of 4.5° was seen in the 6A substrate, and the largest FWHM of 11° was seen in the 8A substrate. Despite this range, all of the RHUL substrates measured appear to have a smaller mosaic

spread than grafoil, whose rocking curves had FWHMs of 11.6 - 14°. ZYX showed the smallest mosaic spreads with rocking curve FWHMs of 3.7°.

It is important to note that using (002) rocking curves as a means of estimating the mosaic spread of a sample gives smaller values than those reported in table 2.1; ZYX is quoted as having a mosaic spread of 9° and Grafoil of 30° plus an isotropic powder component. This data, which is largely taken from the work by Birgeneau *et al.*[6] is obtained by analytic fitting to (hk) peaks diffracting from adsorbed monolayers. Such a measurement characterises the mosaic spread of the 2D crystals that form on the graphite surface whereas the rocking curves performed here measure the mosaic spread of the material itself. The original works which first introduced ZYX [141, 71] describe the then new substrate as having a mosaic spread of ≤ 3 ° measured via an unspecified method, a result which is more consistent with our own measurements.

4.5 Adsorption: Surface Quality

The line broadening measurements of section 4.1 are predicated upon the assumption that larger crystallites are a necessary condition for large surface coherence lengths, which in turn imply greater substrate homogeneity. Irrespective of the success of these measurements, we had no clear indication as to the quality of the surface area obtained by our exfoliation process. As we did not have the requisite expertise to conduct a monolayer scattering experiment to directly asses the surface coherence lengths, we investigated whether adsorption isotherms could be used to assess the homogeneity of our substrate foils.

Since the very first observations of stepwise isotherms on graphitic substrates by Polley [15], it has been known that the homogeneity of the substrate surface plays a key role in determining what features can be seen in an adsorption isotherm. Using graphitised carbon blacks Polley showed that increased crystallinity, as measured by the strength of the (002) diffraction line, corresponded with more pronounced steps in the adsorption isotherm. Similarly, the introduction of exfoliated graphite substrates by Duval and Thomy [19] provided a yet more homogeneous surface, which produced isotherms with distinct 'sub-step' features which are not seen in graphitised carbon black substrates. It can be seen from the krypton isotherm segments in figure 4.10 that the sub-step observed in the Papyex isotherm is suppressed relative to the UEG isotherm sub-step. The diminishing of this sub-step is attributed to the decrease in the homogeneity that occurs when UEG is compressed into Papyex. This is consistent with the surface coherence lengths presented in table 2.1, which show that the 850 Å L_s of UEG is reduced to 200-300 Å when it is compressed into Papyex. The 'sharpness' of krytpon and nitrogen sub-steps have been previously used by other researchers as a qualitative indicator of surface homogeneity, for example Niimi *et al.* [73] have used nitrogen sub-step seen in a 77 K nitrogen isotherm as evidence that their lab-made ZYX substrate is more homogeneous than Grafoil.

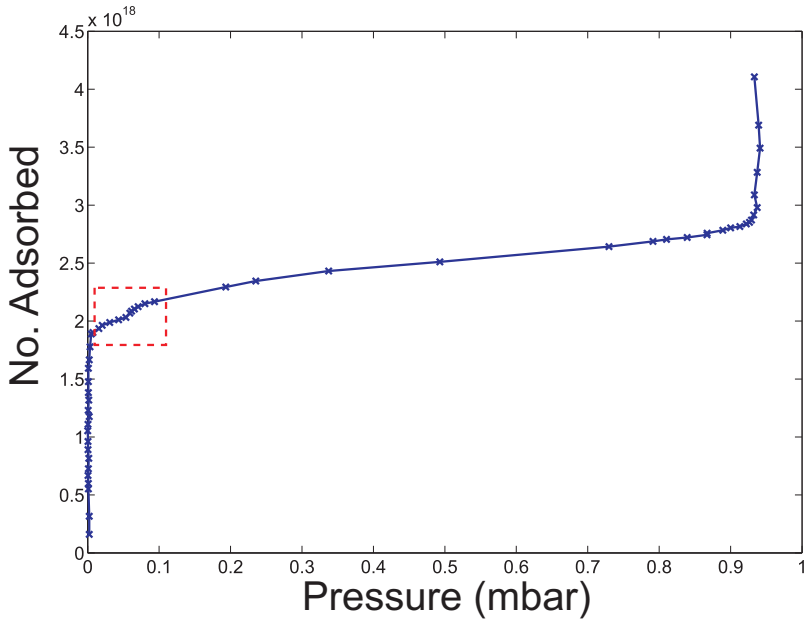

Figure 4.19: Krypton isotherm performed on the offcuts from the batch 11 NMR substrate. A sub-step can be seen at 50 μbar. The mass of substrate in this isotherm was 0.2 g, which implies that the specific area is 1.53 m^2/g.

Figure 4.19 shows a krypton isotherm that was performed on offcuts of the batch 11 NMR substrate. Despite the very low total surface area in the adsorption cell, a sub-step can be clearly seen which indicates that, for the NMR substrate at least, the surface is sufficiently homogeneous to observe the commensurate-incommensurate transition in the krypton monolayer. Encouraged by this result we attempted to perform a high resolution krypton isotherm on the the NMR substrate residing in the actual NMR cell, however this proved to be impracticable due to the low saturated vapour pressure (2.319 mbar) of krypton at 77.3 K, which served to limit the shot size considerably meaning that any isotherm on the NMR cell would take too long. For this reason we decided to investigate the nitrogen fluid-coexistence sub-step as this would hopefully allow for comparison to data in the literature [73, 138].

4.5.1 Procedure

It was decided that a nitrogen isotherm should be performed on the NMR substrate *in-situ* in the cell mounted on the cryostat. The cell assembly and cryostat are described in detail in section 5.3 and related subsections. The procedure is very similar to that laid out in section 4.2.1. The substrate, having been subjected to a heat treatment of 1000° under vacuum before being loaded into the NMR cell, can be cleaned between isotherms by prolonged (>24h hour) evacuation at room temperature using a turbo-pump. The main bath of the cryostat is then filled with liquid nitrogen to cool the cryostat insert which is shown in figure 5.3.

If the cryostat insert is evacuated, then the temperature recorded at the cell plate by the germanium thermometer is >78 K. By adding a small dose of helium exchange gas into the insert, the cell plate temperature quickly reached 77.5 K. At this temperature a nitrogen isotherm was then performed, where the resolution was increased in the region of the sub-step. It was found that during this measurement the temperature recorded by the germanium thermometer varied by as much as 0.3 K. For this reason we decided to perform another isotherm at the actively maintained temperature of 74 K, as there exists high resolution data from Greywall [138] which allows for comparison with Grafoil. The lower temperature also causes the sub-step to be observed at a lower pressure, which has the additional benefit of reducing errors associated with the dead volume characterisation.

Having again cleaned the substrate surface by pumping, the cell is again cooled by filling the cryostat with liquid nitrogen. The temperature of this bath can be decreased by reducing the vapour pressure above it. As can be seen from figure 5.2, the rotary pump that is normally used for the 1 K pot can be adopted to pump directly on the liquid nitrogen by opening the bath valve. One of the main concerns was that we did not want to reduce the pressure to such an extent that the nitrogen bath reached the triple point (63.151 K, 125.2 mbar), as this could

then violently bubble, causing damage to the interior of the cryostat. Temperature control of the bath was done manually; by feathering the pot valve and monitoring the temperature with the RhFe thermometer at the bottom of the cryostat, we were able to maintain a temperature of 70 K. If the bath temperature was too low or too high, then the pot valve would respectively be closed or opened slightly to correct this. Temperature fluctuations were typically of the order of 0.5 K over the course of an hour.

If the insert is evacuated and no exchange gas is used, the temperature at the cell plate is rather isolated from short term temperature oscillations in the bath. This allowed us to maintain 74 K at the cell plate by using a local heater in conjunction with a PID controller. Ultimately, our control was limited by the 50 mK resolution of the germanium thermometer at these temperatures.

As the bath temperature needed to be constantly monitored and controlled, for safety reasons it was necessary to perform the isotherm in one continuous run. After the isotherm was completed, the majority of the nitrogen adsorbate gas was evacuated from the cell and gas handling system by pumping for an hour, after which the dead volume was then characterised by volume sharing of helium gas. For the measurement shown in figure 4.20, the dead volume was found to be 15.68 cm^3, though calculations show that even at the highest pressures, the ratio N_{vap}:N_{ads} is at most 0.06, so any errors in the dead volume characterisation have minimal impact on the isotherm.

Figure 4.20, shows the coverage normalised data from the 74 K isotherm taken on the NMR substrate alongside data obtained by Greywall [138] using Grafoil as a substrate.

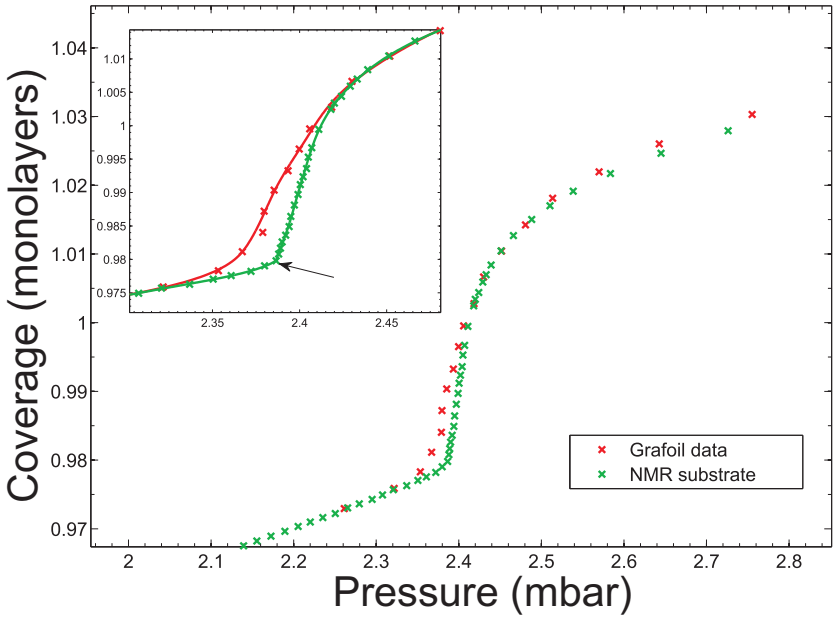

Figure 4.20: Coverage normalised comparison of the isotherm sub-step as measured on our NMR substrate and Grafoil [138]. The inset shows this feature in higher detail in which the data has then been fitted by a moving window spline. For our data it was necessary to fit piecewise two separate splines, which join at the point marked by the arrow. These splines are used in the analysis described in the following section.

Although the resolution of the Greywall data is not as high as ours, the comparison shows that the sub-step observed in our isotherm data is significantly sharper; there is a pronounced discontinuity in the pressure which is consistent with the film undergoing a first-order phase transition from a fluid into a coexistence of fluid and solid. It is thought that the blurring, or rounding of this transition is primarily caused by the substrate displaying a range of binding energies [142, 143, 144, 145]. This is discussed in more detail in the following section.

4.5.2 Adsorption Potential Distribution

Other authors [73] have used the sharpness of the nitrogen sub-step as qualitative evidence for greater homogeneity in their manufactured substrates. Desiring a more precise means of interpreting our isotherms, we have applied the analysis outlined by Kruk and co-workers [146], whereby the *adsoprtion potential distribution* is calculated from the isotherm data.

The central premise of this analysis is that at every point in the isotherm, the film and vapour are in equilibrium, i.e. their chemical potentials μ_f and μ_v are equal. For an ideal gas the chemical potential is given by

$$\mu(T) = RT \ln \left[\frac{P_0(T)}{P} \right], \tag{4.25}$$

where T is the temperature and $P_0(T)$ is the saturated vapour pressure. If the isotherm vapour can be assumed to be ideal, then the pressure observed in an isotherm can be treated as a probe of the adsorbed film, which itself is intimately governed by the nature of the adsorbing surface. An isotherm plot of coverage-versus-pressure is then readily transposed to coverage-versus-adsorption potential. The adsorption potential distribution is then obtained by the differentiation of the coverage, ϕ with respect to the adsorption potential,

$$\chi_r = -\frac{d\phi}{d\mu} = -\frac{1}{N_m}\frac{dN_{ads}}{d\mu}, \tag{4.26}$$

where the coverage, ϕ is defined in the isotherm by the number, N_m at which monolayer capacity has been reached.

In their work, Kruk and co-workers perform detailed isotherms on a variety of carbon black powders, where each sample had its crystallinity assessed based on the strength of its (002) graphite diffraction line. Key results are shown in figure 4.21

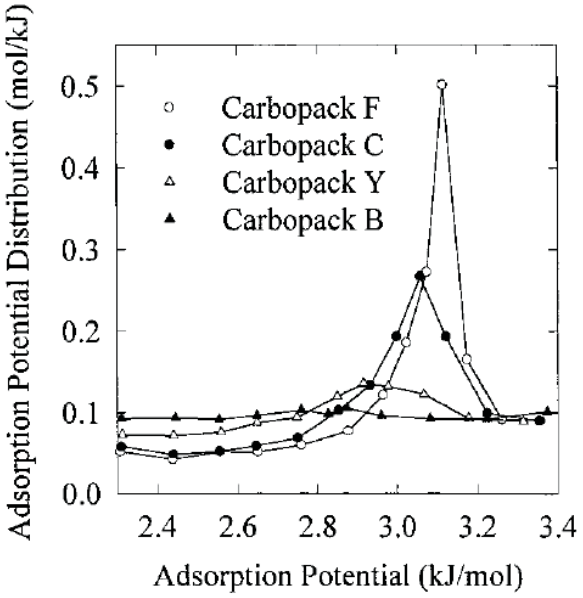

Figure 4.21: Adsorption potential distributions for different carbon blacks, calculated at the fluid-coexistence transition. Data taken from [146]. The carbon powders in order of degree of graphitisation are; F>C>Y>B.

This is evidence that the degree of crystallinity in the adsorption substrate is positively correlated with surface homogeneity. Ecke [142] and Dash [147] both propose that an adsorption isotherm on a perfectly homogeneous and flat substrate should display a vertical sub-step, which would then manifest as a delta function in the adsorption potential distribution using the analysis method of Kruk. The advantage of this method compared to others described in the literature [145], is that it is largely model independent, whereas other methods make assumptions about the form of an ideal isotherm.

Given that we believe our substrates to be more certainly crystalline than Grafoil, we should therefore expect that analysing the data in 4.20 should result in a larger and narrower adsorption potential distribution as a consequence of our substrate being more homogeneous.

In order to use equation 4.26 on the data in in figure 4.20, we have found it

necessary to use a moving window spline fit to the data so as to smooth out the effect of scatter, which can cause large divergences. As our own data is clearly discontinuous, we have chosen to fit two separate splines which join at the point of discontinuity. It is these spline fits that are then used in equation 4.26, with the results shown in figure 4.22.

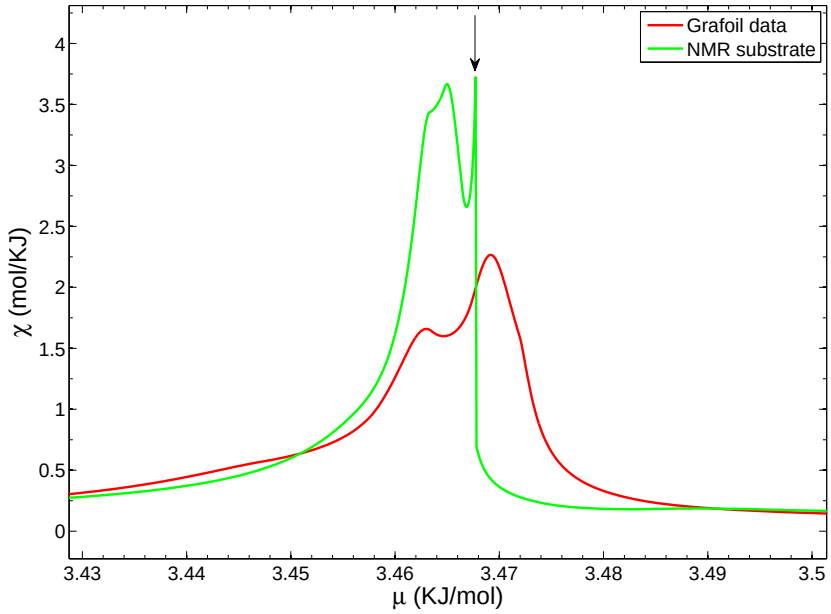

Figure 4.22: Adsorption potential distributions, calculated from the data in figure 4.20. The arrow indicates the discontinuity that arises due to fitting two piecewise splines to our data.

The features around the peak plateau are caused by measurement noise at the 1 μbar level. This prevents us from making a quantitative comparison of the new substrates. Without reference to any particular adsorption model, it is expected that the adsorption potential distribution is in part governed by the distribution of binding energies of the substrate. The narrower peak is therefore evidence that the batch 11 NMR substrate is more homogeneous than Grafoil.

In order to use this technique as a quantitative probe, pressure stability of the order 100 nbar would be necessary, which is achievable using thermally stabilised volumes.

It was originally hoped that this technique could be performed on other substrates, with priority being given to ZYX and then Grafoil so that direct comparison could be made. However, in light of the strange pressure oscillations near monolayer completion that were observed during a 77 K nitrogen isotherm on our ZYX sample, it seems unlikely that we would have been able to analyse the ZYX sample with this new technique. Additionally, on opening the cryostat so that the necessary modifications could be made, it was found that during the 74 K isotherm moisture had been drawn into the bath space causing significant corrosion damage to the insert. Clearly operating for a prolonged period with an underpressure in the bath space exceeded the design specifications of the dewar. Further isotherms at 74 K were therefore not performed.

4.6 Results and Discussion

Using the procedures described in chapter 4, a variety of prototype substrate have been manufactured and then characterised using the methods outlined in this chapter. A central assumption of the project has been that substrate crystallinity is an indirect indicator of substrate homogeneity; for this reason we have chosen to employ diffraction techniques as a means of probing the microstructure of these new materials. The primary means of characterisation has been through the analysis of diffracted (110) lines from our prototypes substrates. Other techniques have been used to assess other key properties of our substrates; adsorption isotherms have been used to confirm that the new materials meet the minimum surface area requirement of 1 m^2/g. Rocking curves performed on our substrates show that their mosaic spreads lie between those of Grafoil and ZYX. Finally, purity analysis shows that, provided the sample is subject to sufficient heat treatment, no residue remains of the intercalation process and the exfoliated material can be purified to a point where the contaminant concentration is less than Grafoil.

The results of the line broadening, adsorption isotherms and rocking curves have been summarised in table 4.6. A full summary of the (110) line broadening fit parameters can be found in the appendix. Many of the substrates had multiple measurements performed, and for the sake of clarity the average value is presented here.

Sample	T_E(°C)	f_v^s(°)	L (Å)	Mosaic (°)	Specific Area (m^2/g)
Grafoil	-	0.1608	660	11.6-14	18.3
ZYX	-	0.1311	810	3.7	1.95
4H	700	0.1734	610	10	4.20
5E	400	0.0651	1630	6.5	-
6A	400	0.1467	725	4.5	-
6C	350	0.1289	824	5.5	-
6D	250	0.0924	1151	7.5	-
8A	250	0.06145	1733	11	-
8B	225	0.0799	1331	-	-
8C	200	0.1240	858	-	-
8D	225	0.1362	780	-	0.93
8E	225	0.0824	1307	-	-
9A	200	0.12177	878	-	1.02
9B	190	0.0850	1251	-	-
11 (NMR)	350	0.1167	913	8.1	1.58
14A	200	0.1222	870	-	0.99
14C	200	-	-	-	0.96

Table 4.5: Summary of prototype substrate characterisations. T_E is the initial exfoliation temperature.

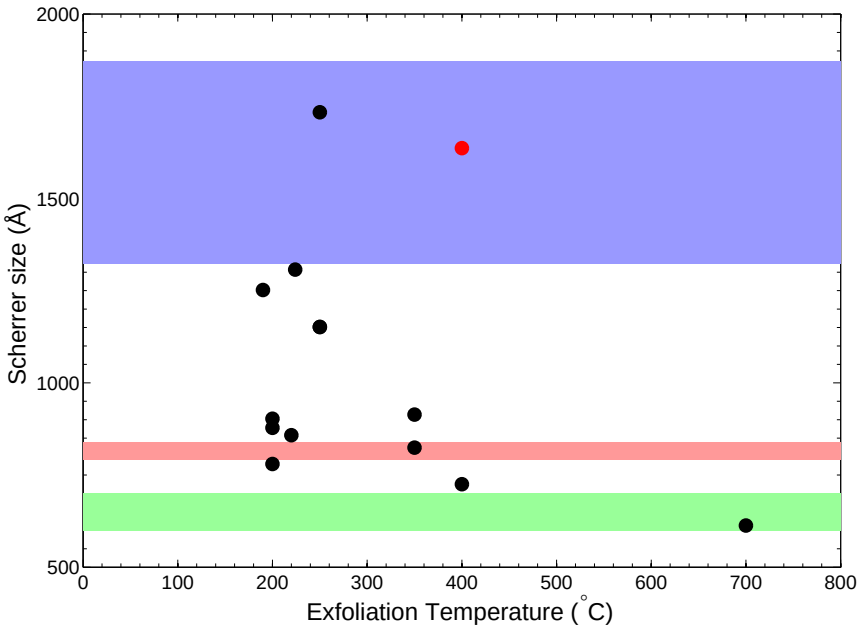

Figure 4.23: Graph of exfoliation temperature, T_E versus L, the apparent Scherrer size. The green, red and blue shaded regions represent the size ranges of Grafoil, ZYX and HOPG respectively. The red data point is measured from the 5E substrate, which is thought to be an anomaly as is discussed in the text.

The results in table 4.6 are presented such that the key control parameter is the exfoliation temperature, which is then expected to govern the crystallite size in the exfoliated material. We anticipated that higher exfoliation temperatures results in a more vigorous vapourisation of the intercalant which then disrupts the host graphite to a greater degree thus producing smaller crystallites in the process. As can be seen from figure 4.23, plotting the crystallite size as a function of exfoliation temperature produces a scattered graph with no clear trend. This could be attributed to the fact that the sample histories, which are given in the appendix, show some evolution in the procedure; it was not until the batch 8 foils that an established method of removing the remnant intercalant was established. For example, the foils 6C and 6D were not subjected to a long slow heat treatment to remove this residual intercalant,

though it is assumed that exposing these samples to air without the second heat treatment has negligible effects on the sample crystallinity. Another explanation however is that applying the Scherrer equation to analyse the (110) line broadening is not valid in this scenario as we have been unable to account for strain broadening effects due to lack of higher order $(hk0)$ reflections. We have therefore chosen to interpret the line broadening as an indicator of generalised crystal quality. Figure 4.24 is a plot of all f_v^s values from table B, as a function of the substrate exfoliation temperature.

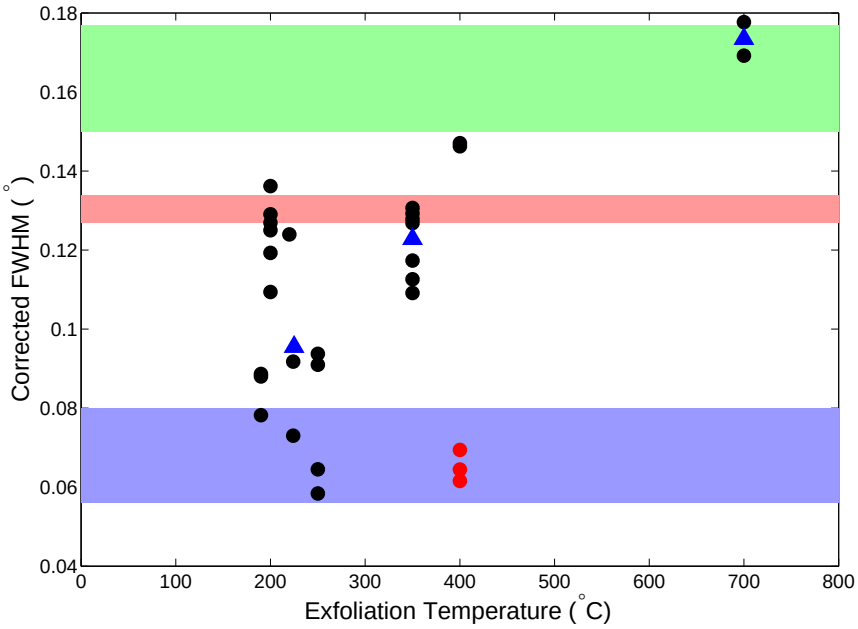

Figure 4.24: Graph of exfoliation temperature, T_E versus the corrected FWHM, f_v^s, using all the values in table B. The blue points represent averaging, which is justified in the text.

The most striking feature of this graph is the large amount of scatter in the measured widths of the low temperature exfoliated samples, the majority of which display widths that are less than or equal to ZYX. The foils that make up these

data points were all exfoliated at temperatures below 250°C, where many of the data points are repeat measurements on the same sample, which were taken by resetting the instrument and running the θ-2θ scan again without realigning the sample. Initially it was thought that this variation could be attributed to errors associated with the fitting of the Voigt functions to the diffracted peaks, however for those foils where several repeat measurements were performed, it can be seen that the width variation is typically on the order of 10%, with the largest range being seen in the 8E foil, with a range of 20%. The width variation could also be attributed to the differing secondary heat treatments of the substrates, which of course cannot be ruled out as a possibility.

As understanding of this technique has grown, it is now thought that this variation is due to poor particle statistics arising from the granularity of the sample, which is then exacerbated further in the Bragg-Brentano geometry. In an ideal powder diffraction measurement, the sample is composed of a great many crystallites such that, on average, all crystallite orientations are represented equally. This results in the so-called Debye-Scherrer rings. For a well conditioned powder (no preferred orientation, particle size < 10 μm), this ring is uniform throughout its circumference, and it is unnecessary to capture the entire ring; it is sufficient to intersect through the ring radially and measure the diffraction pattern in one-dimension. This is the principle behind the Bragg-Brentano diffraction geometry

If however the powder sample is composed of larger crystallites, this then means that all crystallite orientations (and sizes) are unlikely to be well represented in the diffraction volume. Such a measurement results in a 'spotted' or 'textured' diffraction ring. In this scenario a Bragg-Brentano diffractometer is unable to fully characterise the diffraction pattern, as different intersections (represented by the arrows in figure 4.25) of the ring will produce different intensity profiles due to this granular variation.

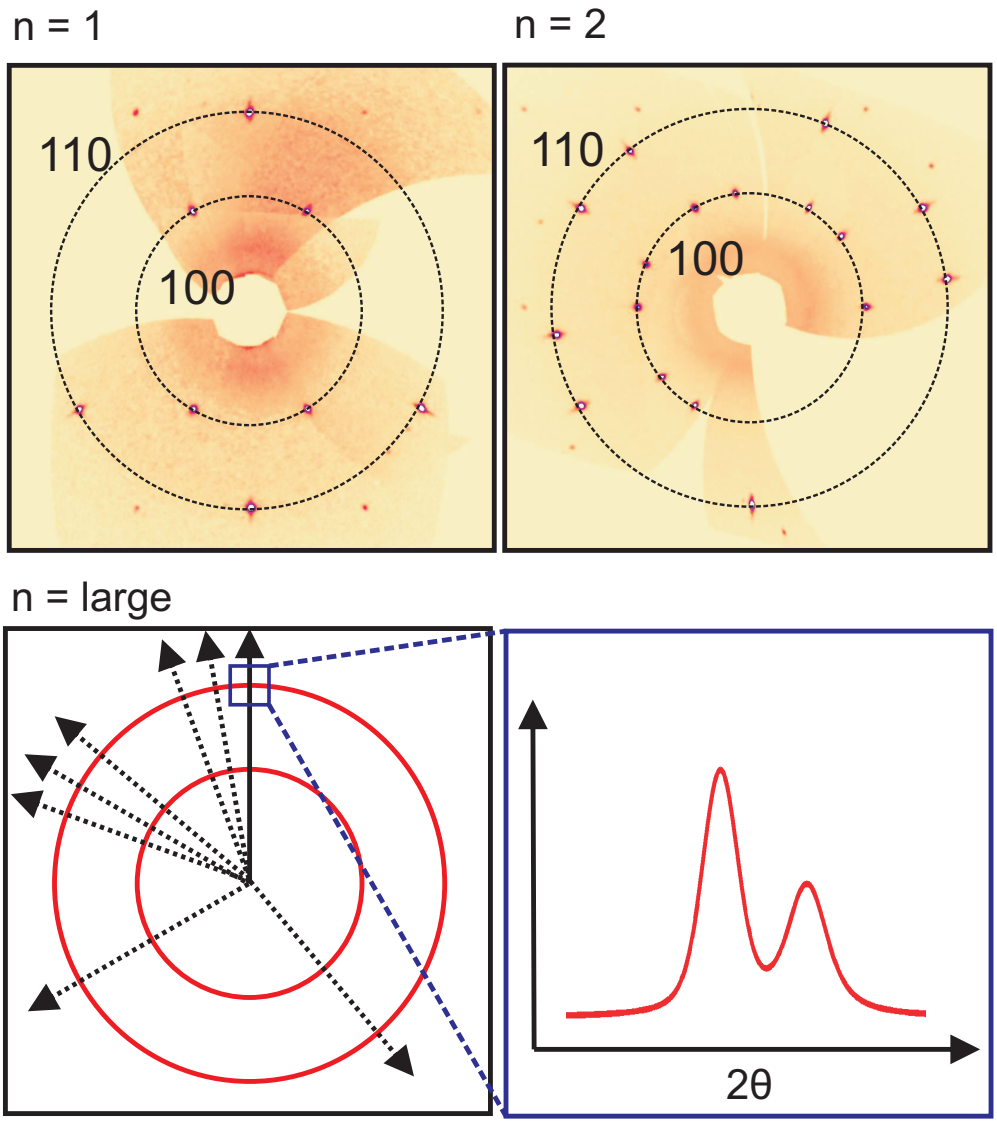

Figure 4.25: Schematic showing how a powder ring is formed from a large number of crystallites in the diffracting volume. The top left and right panel are scans using a single crystal diffractometer, where in the left panel only one ($hk0$) pattern can be seen, whilst in the right panel there is evidence of two crystals in the beam. If a very large number of crystals are present, then Debye-Scherrer rings are observed, as represented in the bottom left panel. In the Bragg-Brentano geomtery, data is obtained by intersecting through these lines as symbolised by the arrows.

This effect can be minimised, though never fully eliminated, by integrating the intensity around the full angular range of the ring. Another way of achieving this integration physically is to simply spin the sample, which is a method commonly employed in Bragg-Brentano and Debye-Scherrer geometries.

Alternatively, if a sufficiently large number of separate scans are performed on the material, and the X-ray beam then illuminates a different volume of sample in each case, this is equivalent to intersecting the diffraction ring at many locations so that gradually an average can be built up. This reasoning can be applied to the data in figure 4.24 if it assumed that for temperatures below 250°C, the samples display roughly equal levels of exfoliation. The many individual measurements performed across all these prototype substrates can then be considered as part of one larger measurement, in which the powder ring has been sampled at many different intersections. Using this construction the widths of all the measurements at 250°C or lower are then averaged into one single width. Applying this assumption to the data points at 350°C and 700°C then gives the trend that we would expect; observed widths decrease with decreasing exfoliation temperature, as shown by the blue data points in figure 4.24.

This of course could be simply a result of there being only two measurements on the one sample (4H) at 700°C, which may simply be a statistical anomaly, and it is entirely possible that performing a large number of separate measurement on the 4H foil, or other 700°C samples would display a similarly large range of (110) widths as is seen in the low temperature samples. This seems unlikely however, given that the observed (110) line profile for 4H, which is shown in figure 4.8 shows marked line broadening, with the two peaks of the K_α doublet overlapping significantly. The only other sample that displayed this level of peak overlap was Grafoil, and it is interesting to note that both Grafoil and 4H are visually very similar, as were all samples that were exfoliated at higher temperatures. It is recognised however that

further measurements on 4H, or other 700°C samples are required in order to fully justify this assertion.

Despite the limitations of these (110) line broadening measurements, particularly with regards to sample granularity, it is important to note that of all the substrates exfoliated at temperatures below 250°C, the majority display (110) widths which are narrower than is observed in our sample of ZYX, and in many cases the widths of these substrates are comparable to HOPG, indicating that our prototype substrates are more crystalline than both Grafoil and ZYX. If this crystallinty can be taken as an indirect indicator of the surface quality, then it is expected that the exposed adsorption surfaces will be commensurably more homogeneous.

In applying this analysis we have disregarded the data obtained from the 5E foil, which was exfoliated at a temperature of 400°C. The (110) widths observed from this foil were exceptionally narrow, however it is now thought that 5E was an anomaly, as it displayed little to no exfoliation and the foil was very delicate and susceptible to crumbling. No other samples exfoliated at 400°C displayed such low levels of exfoliation and it is thought that 5E is simply a result of the GIC having degraded due to an error in the loading process caused by a leak.

Adsorption isotherms performed on the prototype substrates show that at a minimum, specific areas are on the order of 1 m^2/g. The surface area of graphite is known [66] to be positively correlated with the exfoliation temperature, and this can be seen in our samples; 4H displays 4× the surface area of any other prototype substrate, as a result of having been pressed from graphite exfoliated at 700°. This relationship has not been studied systematically however, as we have chosen to characterise only a fraction of the substrate foils due to the time intensive nature of the adsorption isotherm measurement.

In terms of mosaic spreads, no clear dependence on exfoliation temperature can be seen, though it is expected that as with the (110) line broadening measurements,

rocking curves would be subject to local granular variation in the substrate, particularly in those samples manufactured from low temperature exfoliated graphite. In any case, it is important to note that for all substrates that were characterised, the observed mosaic spread is less than that of Grafoil, which is considered to be an improvement.

Based on the evidence from these characterisation measurements, we have finalised the exfoliation procedure which we believe will produce an exceptionally homogeneous substrate. In preparation of this, GIC batch 17 was manufactured with the sole purpose of being exfoliated to produce the final substrate. Batch 17 was made using a total of 7.576 g of Madagascan flake graphite, which has been outgassed at 500°C under vacuum for several hours in accordance with the protocols laid out in section 3.2.3. Using 0.749 g of potassium, this graphite was intercalated as KC_{36} using the ampoule method described in section 3.2.5. After allowing the sample to homogenise in the furnace for several days, the KC_{36} was removed and then exposed to ammonia to produce the ternary compound. The staging and homogeneity of the batch was then confirmed by eye and by $(00l)$ scans which confirmed the sample to be stage-3.

For the final procedure we had intended to exfoliate the batch 17 GIC in a series of exfoliations with 1 g of GIC in the metal reaction vessel, using a temperature of 190°C. The first run was unsuccessful as a significant fraction of the GIC material had not undergone exfoliation. It is thought that at low temperatures, because the exfoliation is far less vigorous and forceful, it is much more likely that the expansion of the graphite can be inhibited by other flakes which lie on top or to the side.

After some experimentation it was found that a compromise could be made if the mass in the reaction vessel was limited to 0.4 g at any one time, and if the exfoliation temperature was set to 230°C. The final exfoliation procedure was as follows; 0.4 g of batch 17 was loaded into the metal reaction vessel and evacuated down to 10^{-4}

mbar. Once this pressure was reached, the metal tube was inserted into a muffle furnace at a temperature of 230°. Using the control interface on the furnace, the heating program was set so that the furnace would remain at a temperature of 230°C for 12 hours, after which the heat would be increased to 700°C at a rate of 0.3°C/min. The sample would then be left at this temperature for a further 12-18 hours before being removed from the furnace. The exfoliated sample is then removed from the reaction vessel and stored in the glove box. This process was repeated a total of eight times to produce 3 g of exfoliated material. Once sufficient material had been collected, this was gathered and taken to RHUL to be subjected to further heat treatment to remove contaminants. At RHUL, the exfoliated graphite sample was loaded into a graphite crucible, and then subjected to 24 hours at 1000° under vacuum. As has been discussed in section 4.3, this heat treatment is able to purify the graphite samples to an extent where it displays contaminant concentrations lower than Grafoil.

4.7 Diffusion Bonding

Having made the requisite exfoliated material for the final substrate it was now necessary to press this into foils and prepare these for installation into a cell for a sub-millikelvin NMR experiment. One of the main challenges at ultra-low temperatures is ensuring a good thermal conduct of the sample with the nuclear demagnetisation stage. For studies of helium on graphite the established protocol is to diffusion bond the graphite to annealed silver or copper foils, where the ends of these foils can then be connected to an anchoring post that is in good thermal contact with the demagnetisation stage.

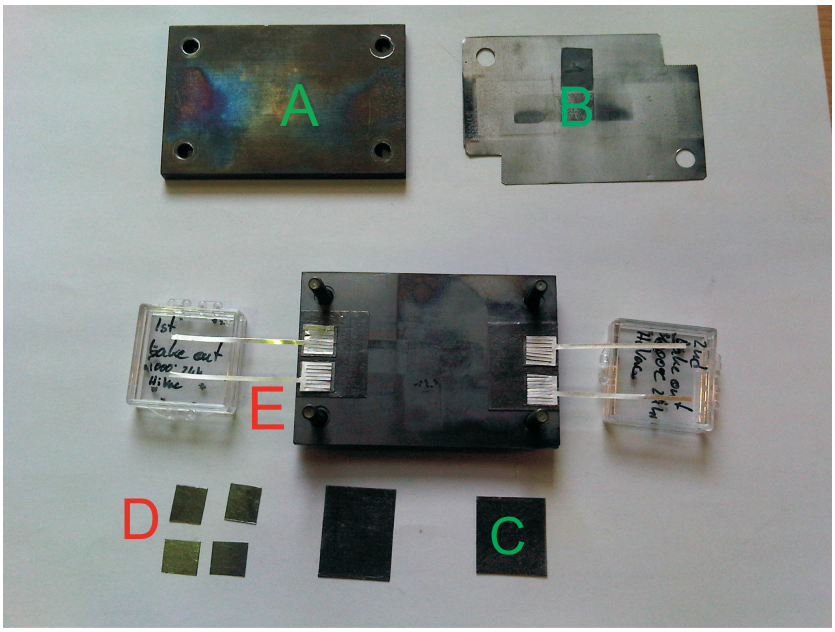

Figure 4.26: Stainless steel vice for diffusion bonding graphite substrate foils to silver. The labelled pieces are A; stainless steel vice plate, B; molybdenum plate spacer, C; Grafoil spacer, D; adsorption substrate, E; silver foil. Photo courtesy of Frank Arnold.

The diffusion bonding process is performed using a stainless steel bonding vice, which is shown in figure 4.26. Typically, diffusion bonds are made by sandwiching the silver between two substrate foils. On either side of this sandwich are placed a Grafoil and then molybdenum spacers. This entire apparatus is sandwiched between the two steel vice plates, and secured together at each corner with steel nuts and bolts. A torque wrench is used to ensure that all four corners are tightened to 1 Nm. As can be seen from the figure the silver foils have long tongues reaching outside of the vice, which are used to connect to the thermal anchoring post. The fully tightened vice is then placed into the furnace which is evacuated to 5×10^{-5}mbar, and thoroughly checked for leaks. The temperature is then raised to 750°C where it dwells for 45 minutes before being cooled.

In Grafoil, a known side effect of this diffusion bonding process is a significant

reduction of specific area; In some cases, the specific surface area has been reduced by as much as 40% [69]. This was of some concern to us; based on the adsoprtion isotherms of the substrate foils 9A, 14A and 14C, it was expected that the final substrate would most certainly have a specific area on the order of 1 m^2/g. If this area is then reduced by 40% by diffusion bonding, another exfoliation process may be required in which the exfoliation temperature is slightly higher to counteract this loss in surface area. A test diffusion bond was thus performed on some substrate foils which had been pressed from graphite exfoliated using the finalised procedure, so that it could have its surface area measured via adsorption isotherm.

Using approximately 0.4 g of the final exfoliated material, seven foils were pressed using the new pellet die, where each foil was between 0.05g and 0.065g in mass, with an average thickness of 215 μm. Because the low temperature exfoliated foils had a tendency to partially disintegrate when subjected to heat treatment, it was decided that these foils would not be outgassed. Instead, they were placed straight into the adsorption cell, and subjected to prolonged evacuation in an attempt to clean the surfaces. A krypton isotherm was then performed on these foils, and the specific area was found to be 0.56 m^2/g, which is on the order of the intrinsic area of the Madagascan flake, though it was possible to see the krypton substep at 50 μbar.

The adsorption cell was then opened and the foils removed. Either during the isotherm, or during the cell opening three of the foils had disintegrated. Despite the disintegration and the apparent loss in surface area, we decided to proceed with the diffusion bond, as it was surmised that this process would also serve as a second heat treatment, and in the process open up any closed galleries exposing surface area that was lost when the foils were first compressed. The foils were therefore cut into 9×9 mm squares, which were then placed into the vice with the silver foils and subjected to the diffusion bonding process. Figure 4.27 shows the two successfully bonded sandwiches.

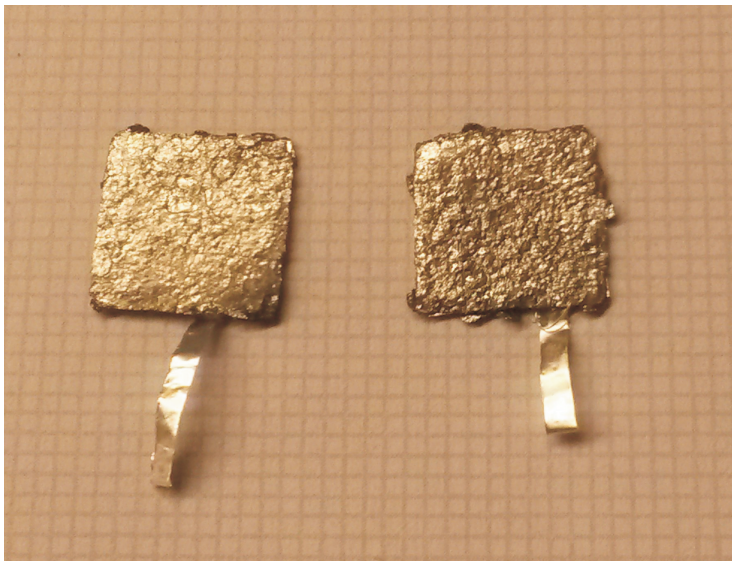

Figure 4.27: Photograph showing two successful silver bond sandwiches. Each bonded square is 9×9 mm. The total graphite mass in these bonded foils is 0.1097 g

These two sandwiches were then placed in the adsorption cell along with a specially made spacer which reduced the dead volume of the adsorption apparatus to 4.9 cm^3. Using the number of adsorbed atoms at the 50 μbar point in the isotherm, the total surface area of the two silver bonded sandwiches in the cell was found to be 0.107 m^2. Before the diffusion bonding process, both the square cut graphite foils and the the silver foils were carefully weighed. The mass of graphite in the diffusion bonded sandwiches is 0.1097 g which corresponds to a specific area of 0.98 $\pm$ 0.04 m^2/g, where the primary error arises in the resolution of data points around 50 μbar. Contrary to what occurs in other substrates, it appears that the diffusion bonding process has *increased* the surface area of this substrate. To confirm this surprising result we repeated the measurement by producing a further two foils, which were then diffusion bonded using the same procedure as before. Figure 4.28 shows the results of a krypton adsorption isotherm that was performed on the bonded sandwich.

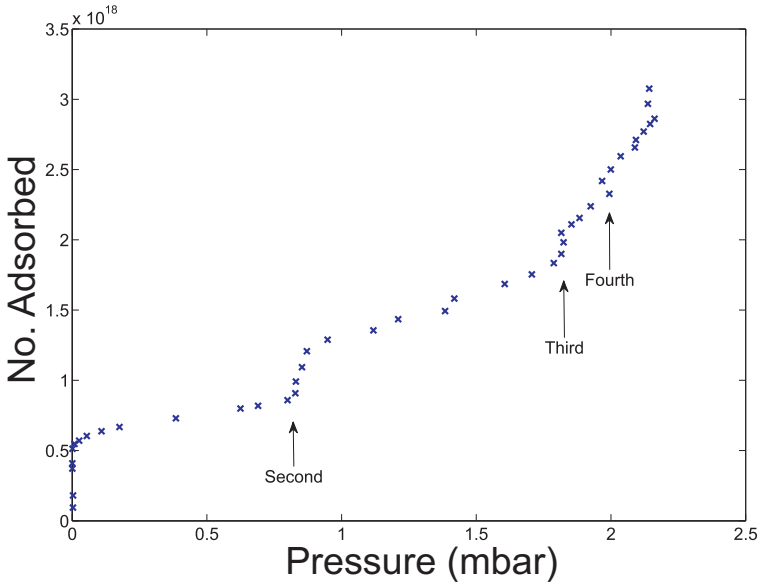

Figure 4.28: Krypton adsorption isotherm on the diffusion bonded sample showing formation of four layers. The total surface area in this measurement is 0.095 m^2

The mass of graphite presented in the bonded in sandwich was 0.096 g, which then gives the specific area as 0.99 $\pm$ 0.05 m^2/g, confirming the surface area measurement performed on the other foils. The isotherm shown above also clearly shows evidence of the formation of four distinct krypton monolayers, which in and of itself can be taken as qualitative evidence surface homogeneity. It was hoped that we would be able to observe the krypton substep at 50 μbar, however it was found that each shot of gas took a long time to equilibrate, with each point in figure 4.28 taking over an hour to obtain. This combined with the small total area in the adsorption cell meant that resolving this substep was impractical.

It is thought that the diffusion bonding process increases the surface are through the opening of previously closed galleries within the substrate foil. As is described in section 2.2, exfoliation is thought to occur as a result of increased mobility in the intercalant causing accumulation at defects and other sites. At these points

disk shaped agglomerations of intercalant can form, which due to the heat then vaporises, forming a bubble-like cavity within the graphite. If the expansion is great enough then these cavities can then rupture allowing the vaporised intercalant to escape, and in the process exposing the internal surfaces of the cavity as available areas for adsorption. If the exfoliation temperature is low, it is thought that the fissures connecting to these internal cavities can be closed off easily by compression, thus reducing the surface area available for adsorption. It is thought that during the compression, either gas or moisture is trapped in these closed galleries, which means that when the substrate foil is heated a second time, these gases escape causing the partial disintegration that was observed in the substrates exfoliated at low temperatures, but in the process they reopen the previously closed galleries and the surface area is somewhat partially restored. It is thought that this is what occurs during the diffusion bonding process, and that because compression is maintained throughout the heating, this serves to prevent the foil from disintegrating.

This is taken as evidence that the final substrate can be diffusion bonded and still display a surface area of 0.98 m^2/g, which is thought to be sufficiently close to the 1 m^2/g limit imposed by the calculations in section 3.5. We then proceeded to prepare the remaining exfoliated material; a further 32 substrate foils were pressed, cut into 9×9 mm squares and diffusion bonded onto silver. A further 16 sandwiches, similar to that shown in figure 4.26 have been produced, which now reside in a evacuated container awaiting installation into an ultra low temperature experimental cell. These sandwiches have not had their surface areas characterised, however based on the measurements described in this section it is expected that the cell will have a total surface area of 0.85 m^2.

Chapter 5

Nuclear Magnetic Resonance Measurements

The ultimate purpose this work is to create a new graphitic substrate suitable for use in study of adsorbed helium films. The results of the investigations presented in the previous chapter give good indication that the surface quality of the RHUL foils is better than that of Grafoil at least, though at the cost of reduced surface area. The trade off between surface quality and specific surface area had always been anticipated however. The surface area of the foils that were made were found to be in the 0.4 - 2 m^2/g range. ZYX historically is $2m^2/g$ and although it presents its own technical difficulties [72], it has been possible to perform most, if not all, of the same adsorption experiments on ZYX as have been performed on Grafoil and Papyex. It was decided that a preliminary SQUID NMR measurement using a prototype RHUL foil as the substrate. The measurement would focus on a well studied NMR feature of ^{3}He on graphite, namely, the cusp in T_2^* that coincides with monolayer completion.

5.1 Nuclear Magnetic Resonance

This section gives a brief introduction to the principles of NMR. For a more thorough exposition, the interested reader should consult the texts of Cowan [148] and Abragam [149].

All atomic nuclei can be characterised by the nuclear quantum spin number, I, which can be integer or half-integer in value. For any atomic nuclei with non-zero spin, there is an associated magnetic moment of

$$\boldsymbol{\mu_s} = \gamma \mathbf{L} \tag{5.1}$$

where γ is the gyromagnetic ratio, and is specific to each nuclear species, and $\mathbf{L}$ is the total nuclear angular momentum with a magnitude given by

$$L = \sqrt{I(I+1)}\hbar \tag{5.2}$$

If an external magnetic field, $\mathbf{B}$ is applied to a nuclei with with non zero spin, it will experience a torque, $\boldsymbol{\tau}$, given by

$$\boldsymbol{\tau} = \boldsymbol{\mu_s} \times \mathbf{B} = \hbar \dot{\boldsymbol{L}} \tag{5.3}$$

Substituting for $\mathbf{L}$ using equation equation 5.1 gives

$$\dot{\boldsymbol{\mu}}_{\boldsymbol{s}} = \gamma \boldsymbol{\mu_s} \times \mathbf{B} \tag{5.4}$$

For a static $\mathbf{B} = B\mathbf{z}$, the following solutions are found;

$$\mu_s^x(t) = \mu \sin(\theta)\cos(\gamma B t) \tag{5.5}$$

$$\mu_s^y(t) = -\mu \sin(\theta)\sin(\gamma B t) \tag{5.6}$$

$$\mu_s^z(t) = \mu \cos(\theta) \tag{5.7}$$

where θ is the angle of $\boldsymbol{\mu}$ with respect to the field. These solutions describe circular motion in the x-y plane and a constant magnetisation along the z-axis i.e. the magnetic moment precesses about the static field with a frequency, $\omega_0 = \gamma B$ which is known as the Larmor frequency.

In real systems composed of a large number of spins, individual magnetic moments can be replaced by the magnetisation, $\mathbf{M}$ of the system, which for low applied fields approximates as

$$M = \frac{N_v \gamma^2 \hbar^2 I(I+1)B}{3k_B T} \tag{5.8}$$

Where N_v is the volumetric number density and T is the temperature of the system. If the magnetic moment components $\mu_{x,y,z}$ are replaced with their corresponding magnetisation components $M_{x,y,z}$ in equations 5.5, an unrealistic scenario arises in which the magnetisation is seen to precess indefinitely about the magnetic field.

In reality however, if a spin system is disturbed, it is observed to return to equilibrium with some characteristic time. During this process, the transverse magnetisation components are seen to vanish, and the equilibrium magnetisation, given by equation 5.8 is restored. A phenomenological description of this relaxation was

first given by Bloch [150] in the equations that bear his name

$$\dot{M}_x = \gamma \left|\mathbf{M} \times \mathbf{B}\right|_x - \frac{M_x}{T_2^*} \tag{5.9}$$

$$\dot{M}_y = \gamma \left|\mathbf{M} \times \mathbf{B}\right|_y - \frac{M_y}{T_2^*} \tag{5.10}$$

$$\dot{M}_z = \gamma \left|\mathbf{M} \times \mathbf{B}\right|_z + \frac{M_0 - M_z}{T_1} \tag{5.11}$$

With solutions

$$M_x(t) = M_\infty \sin(\theta)\cos(\omega_0 t)\exp(-t/T_2^*) \tag{5.12}$$

$$M_y(t) = -M_\infty \sin(\theta)\sin(\omega_0 t)\exp(-t/T_2^*) \tag{5.13}$$

$$M_z(t) = M_\infty - M_\infty(1 - \cos(\theta))\exp(-t/T_1) \tag{5.14}$$

Where M_∞ is the equilibrium magnetisation at $t = \infty$ and can be calculated with equation 5.8, and the parameters T_1 and T_2^* are the *longitudinal* and *transverse* relaxations times respectively. Interpretation of both T_1 and T_2^* is involved and a thorough discussion can be found in the work by Cowan [148], however the essentials of both longitundal and transverse relaxation will now be described.

5.1.1 Longitudinal Relaxation

If an external field is suddenly applied in the z-direction to an otherwise unmagnetised system of spins, it will be observed that the magnetisation grows with time constant T_1 until reaches it equilibrium value, as given by equation 5.8. Essentially, this is an energy exchange process of the the spin system with its surroundings. For this reason T_1 is often also referred to as the *spin-lattice* relaxation time. T_1 times have not been measured in this work, and will only be discussed as it pertains to the maximum pulse rate in a practical NMR measurement.

5.1.2 Transverse Relaxation

For a disturbed system relaxing back to equilibrium there will be an transverse component which is observed as the magnetisation precesses about the applied field. This transverse component is seen to decay with time constant T_2^* due to the dephasing of spins, which arises due to the fact that each individual spin experiences a different magnetic field, and so each precesses at a different rate. This gradually leads to destructive interference between the spins and the transverse magnetisation is then lost.

This local field variation has two origins: the static magnet inhomogeneity , $\Delta B/B$ and the spin-spin dipole interaction. Each of these contributions to the transverse relaxation can be approximately separated through the following equation;

$$\frac{1}{T_2^*} = \frac{1}{T_2} + \omega_0 \frac{\Delta B}{B_0} \tag{5.15}$$

where T_2 is the relaxation intrinsic to the system, and can be determined if the magnet magnet inhomogeneity is known, or through the use of spin-echoes, which is a technique which has not been applied in this work.

Measurement of T_2^*, or T_2 times can be used to make inferences about the mobility of the spins in the system. For example, in a liquid sample the spins are able to move around to some extent and in essence they then all see a similar average field which results in a longer observed T_2^*. This is sometimes referred to as *motional averaging*. By contrast, if the spins are strongly localised as they would be in a solid lattice, then each spin experiences a unique local field resulting in a rapid dephasing, and thus much shorter observed T_2^*.

NMR is therefore a powerful technique that can be used to probe the local environment of spins in a system, as such it has been appllied with great success in the study of ^{3}He films adsorbed on graphite, where it has been used to make inferences

about the structure of the film at various coverages. Some previous experimental results are described in section 5.2. Some practical considerations of NMR are discussed in the next section.

5.1.3 Pulsed NMR

A necessary component of any NMR measurement is the application of a static $\mathbf{B}_0$ field in order to magnetise the system under investigation. By using a superconducting magnet such as described in section 5.3.7, highly stable fields can be realised. Once the system is magnetised it is then necessary to induce some disturbance away from equilibrium in order to observe the consequent relaxation. The method employed in this work is the so-called pulsed NMR, in which the magnetisation, $\mathbf{M}$ of the system can be tipped by some angle θ relative to the static $\mathbf{B}_0$ field. Having been tipped by some angle, the magnetisation relaxes back to equilibrium in accordance with the Bloch equations.

In the NMR assembly described in section 5.3.5, the receiver, transmitter and magnet coils are all mounted such their axes are all orthogonal to one another. By convention the magnetic field is taken to define the z-axis, and the receiver and transmitter can then be taken to define the x and y axes respectively. If an RF-pulse at the Larmor frequency is applied through the transmitter coil the field is then modified as;

$$\mathbf{B} = B_0\mathbf{z} + B_1\cos(\omega_0 t)\mathbf{x} \tag{5.16}$$

Where B_1 is the amplitude of the field produced by the transmitter. If a transformation is made into a frame of reference (x',y',z') rotating about the z-axis with frequency ω_0, the effective field, $\mathbf{B}_{eff}$ experienced by the spins in the rotating frame is then simply $B_1\mathbf{x'}$. Staying in this rotating frame, the magnetisation, $\mathbf{M}$ is then seen to precess around this effective field with frequency $\omega_1 = \gamma B_1$. In both the

rotating and stationary frame of reference this has the effect of tipping **M** away from the z-axis by angle, θ given by

$$\theta = \gamma B_1 \tau \tag{5.17}$$

where τ is the length of transmitter pulse. Once the pulse is completed, the field once again experienced by the spins is the original $\mathbf{B}_0$ field, and the receiver coil set then captures the M_x component of the precessing magnetisation as relaxes back to equilibrium.

5.2 NMR of ^{3}He on Graphite

The review article by Godfrin [69] gives a thorough account of theoretical and experimental investigations of ^{3}He adsorbed onto graphite, however for the purposes of this work, reference will primarily be made to the work of Owers-Bradley [8] who performed some of the earliest detailed NMR studies of ^{3}He adsorbed onto a graphite substrate, using the pulsed NMR technique. His key results are summarised in figure 5.1

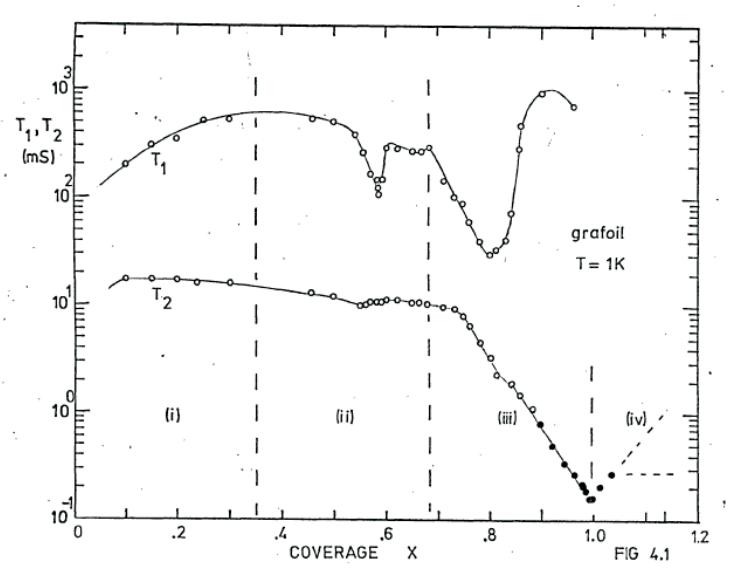

Figure 5.1: Plot taken from [8], showing the variation of T_1 and T_2 as a function of ^{3}He coverage on graphite. The data was obtained at 1 K and 1 MHz. The plot has been divided in four broad sections which are discussed in the text. The monolayer coverage scale is expressed in terms of point-B which is discussed in section 5.4. The open circles of the T_2 correspond to data obtained using spin-echoes. The filled circles correspond to T_2 estimated from the free induction decay.

Using NMR as a probe of the surface, inferences were made regarding the nature of the adsorbed film at various coverages, which at various regions, marked (i)-(iv) in the figure correspond to different film phases. In ascending order these are; the gas phase, dense fluid and registered solid, the solid phase and the multilayer phase. The most conspicuous feature of this graph is the large minimum in T_2 that occurs in region (iii) of the graph. This is attributed to the film forming a 2D solid of increasing density, where as the density increases, so the T_2 relaxation decreases to an absolute minimum which coincides approximately with monolayer completion. At this point promotion to the second layer occurs. This second layer is mobile and the T_2 is seen then to increase.

It is this prominent feature that we were hoping to replicate by performing a similar measurement using a new prototype graphitic substrate.

5.3 Experimental Apparatus

This section describes the equipment that was used to perform NMR measurements on a film of ^{3}He adsorbed onto a new prototype substrate. Included are descriptions of the low temperature platform used to reach and maintain low temperatures along with a detailed discussion of the NMR spectrometer.

5.3.1 Cryostat Overview

The cryostat is a simple design; the most salient features are shown in figure 5.2. The main vessel is a helium dewar from Cryogenic [151] which has a super-insulation vacuum jacket maintaining a helium bath with a typical boil of rate of 0.2 litres/hr. The temperature of the bath space can be monitored via a calibrated Rhodenium Iron (RhFe) thermometer at the bottom of the vessel. In this bath space sits the cryostat insert. The configuration within the Inner Vacuum Can (IVC) is shown in figure 5.3. Temperatures as low as 1.35 K can be reached inside using a continuous fill 1 K 'pot' of the type described by DeLong et al. [152]. With the addition of various heaters throughout the IVC it is possible to operate anywhere from 1.35 - 15 K.

Historically [102], this apparatus was capable of reaching temperatures as low as 1.3 K at the cell plate, however, during the previous run on this cryostat, the fill line impedance became blocked and a new one installed, which was capable of only reaching 1.8 K. In preparation for the NMR measurements presented in this work, this was replaced with an impedance made from 1.47 m of 0.14 mm internal diameter copper-nickel tubing. This length of tubing was determined empirically using a helium flow rate test at room temperature. As stated this new impedance allowed for temperatures as low as 1.35 K to be consistently reached. This apparatus was also used in the adsorption measurements at 74 K described in section 4.5.

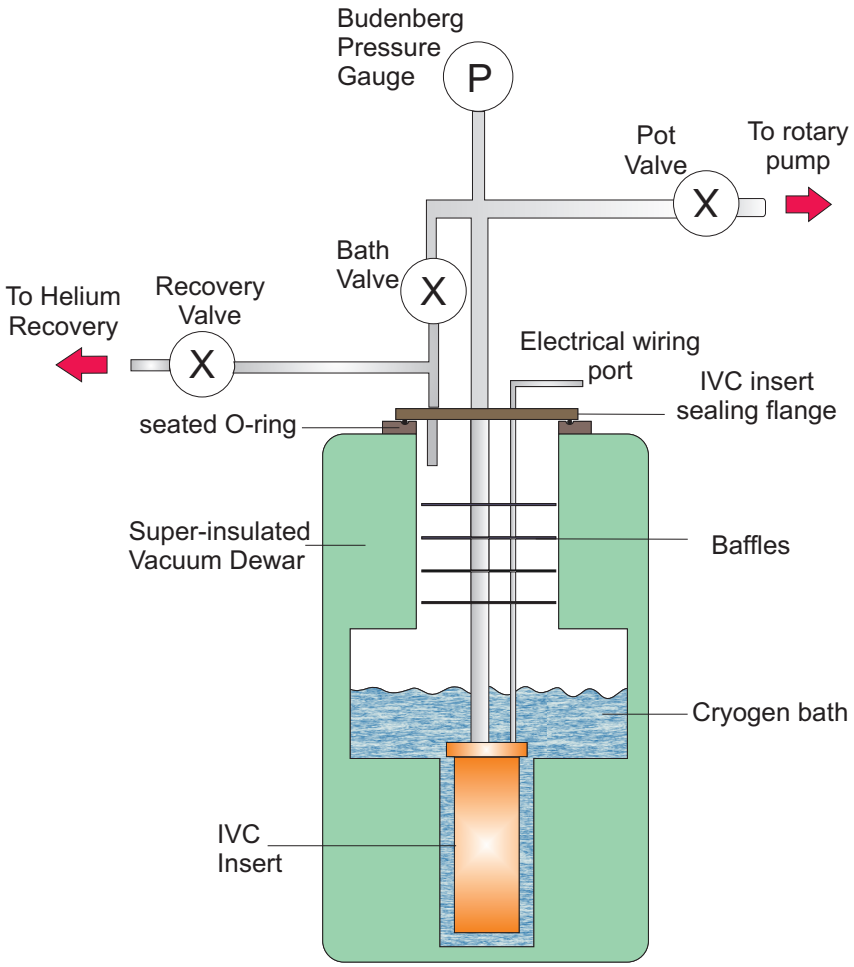

Figure 5.2: Cryostat overview, showing cryostat insert inside the main superinsulated vacuum jacket dewar. Also shown are the various valves controlling the gas links between the pot, bath and recovery gas lines. The stainless steel lines carrying the various electrical lines have been condensed for clarity. The diagram is not to scale.

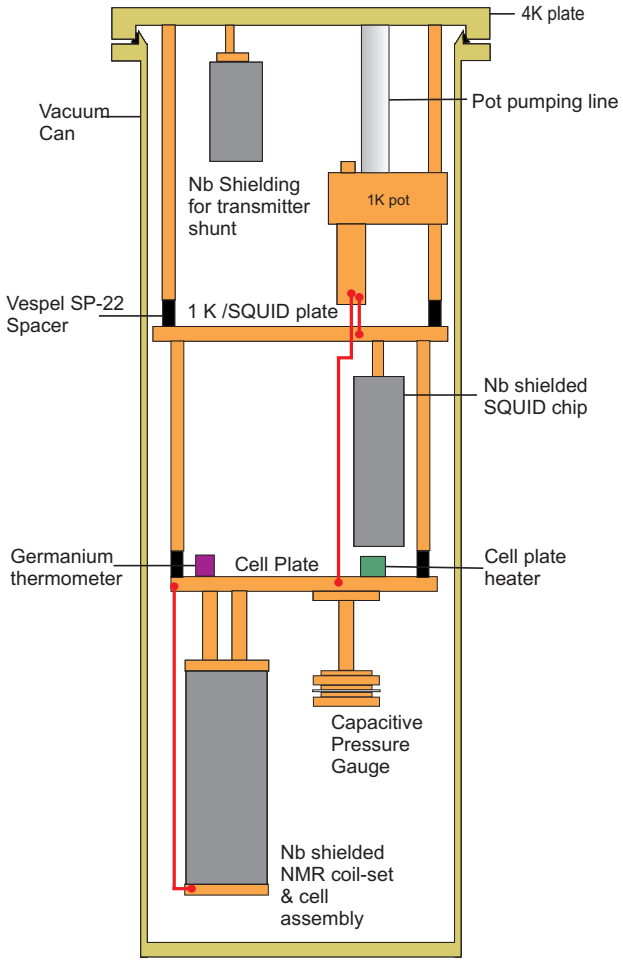

Figure 5.3: Schematic of the IVC insert to reach temperatures below 4 Kelvin. The diagram is not to scale. Thermal links are shown in red.

5.3.2 Thermometry and Control

There is a variety of secondary thermometers on every plate inside the IVC. The pot, SQUID plate and cell plate all had an Allen Bradley and Speer carbon which had been fitted for a previous experiment [102]. The main thermometer was a Lakeshore [153] (Model GR -200A -500 -CD1.4D) germanium resistance thermometer mounted on the cell plate. All the resistances were measured using a an 8-channel Picowatt

AVS-47B bridge, controlled by a LabVIEW program on the experiment computer. Although less accurate at higher temperatures, the Germanium thermometer is calibrated up to 100 K, and was used during the nitrogen adsorption experiments to provide measurement and control at liquid nitrogen temperatures.

The pot reliably reached a base temperature of 1.35 K, however it was decided that measurements would be made at 1.4 K. This was achieved via a standard Proportional-Integral-Derivative (PID) control scheme.

5.3.3 Gas Handling System

The diagram in figure 5.4 shows the basic layout of the gas handling system (GHS) at both room temperature and in the cryogenic environment. The gas handling is constructed of 0.76 mm internal diameter stainless tubing manufactured by HiP® [154], except in the cryogenic environment where 1.3 mm internal diameter Copper Nickel (CuNi) tubing is used. The Paroscientific [139] pressure gauge is capable of a resolution of approximately 2 μBar with averaging.

5.3.4 Capacitance Pressure Gauge

On the cell plate is mounted a Straty-Adams type [155] capacitive pressure gauge. The gauge was designed by Dr. Jan Nyeki and the construction is described in detail the thesis of Dr. Ben Yager [102]. The gauge works by measuring the capacitance between the copper body and a kapton film coated with a thin layer of gold which separates a reference vacuum from the experimental volume. The capacitance is measured by an Andeen-Hagerling (AH) 2550A capacitance bridge [156].

Ultimately, the gauge was not used in the measurement of vapour pressure isotherms. Its high sensitivity however was very useful in determining when equilibrium had been reached.

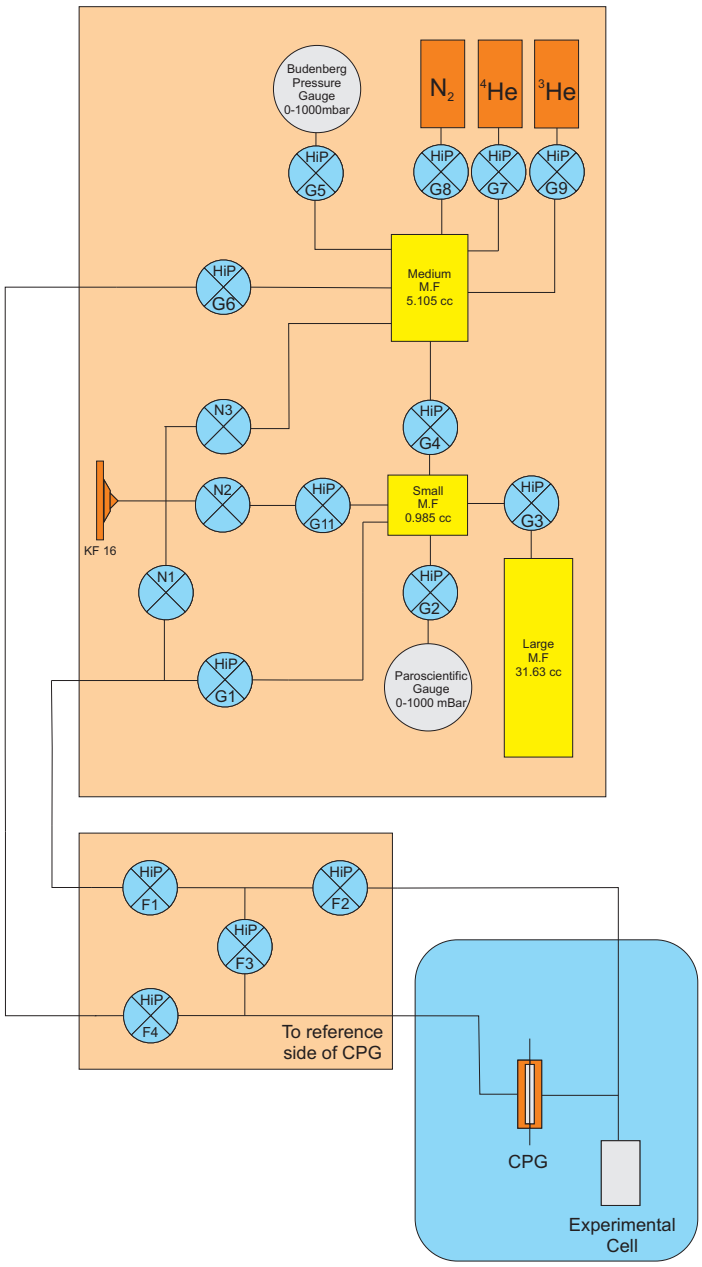

Figure 5.4: Schematic of the gas handling system . The blue region represents the portion of gas handling system in the cryogenic environment, and the the large and small orange regions represent the main and fridge-top gas handling systems respectively. The main gas handling system is a separate self contained module and is virtually identical to another gas handling system module used to perform adsorption isotherms. All valves are HiP® valves with the exception of valves N1,N2,N3 which are Swagelok® valves.

5.3.5 NMR Cell Assembly Overview

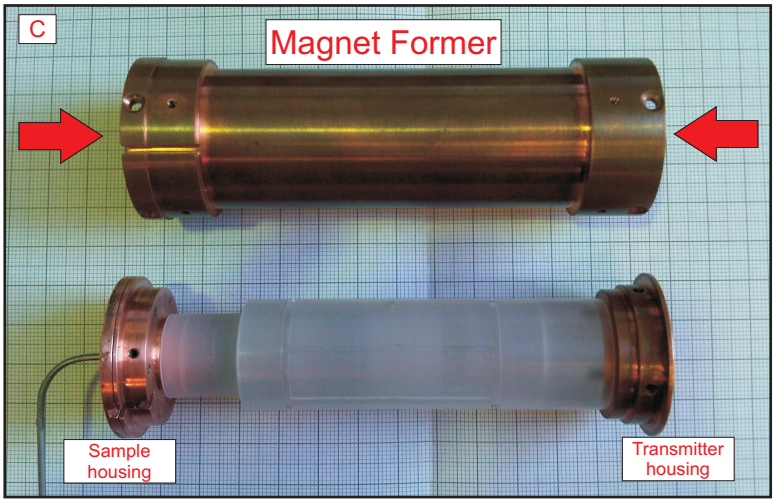

Figure 5.5: Photo of the main NMR cell components. Coil windings and shields are not shown.

The main cell assembly that was used to perform this measurement is a modified version of an existing cell that was used in the work of Dr. Ben Yager [102] to perform NMR measurements of ^{3}He adsorbed onto zeolite. An overview of the NMR cell assembly is shown in figure 5.6. Excluding the shielding, the cell is constructed from three main components; the magnet, the transmitter housing and the sample housing. As can be seen from the photo in figure 5.5, the sample and transmitter housings are inserted into either end of the magnet and then secured with grub screws. Within the magnet space, the transmitter former then partially overlaps with the sample housing. This design provides some degree of mechanical decoupling of the receiver from the transmitter which then serves to minimise magneto-acoustic resonances that occur during pulses. On insertion into magnet former, the receiver and transmitter coil pieces can be rotated such that the axes of the receiver, transmitter and magnet coil are all orthogonal to one another. The

transmitter and magnet are the original pieces used in Dr. Yagers work, whilst the sample housing was designed and assembled by Frank Arnold to interface with these existing components.

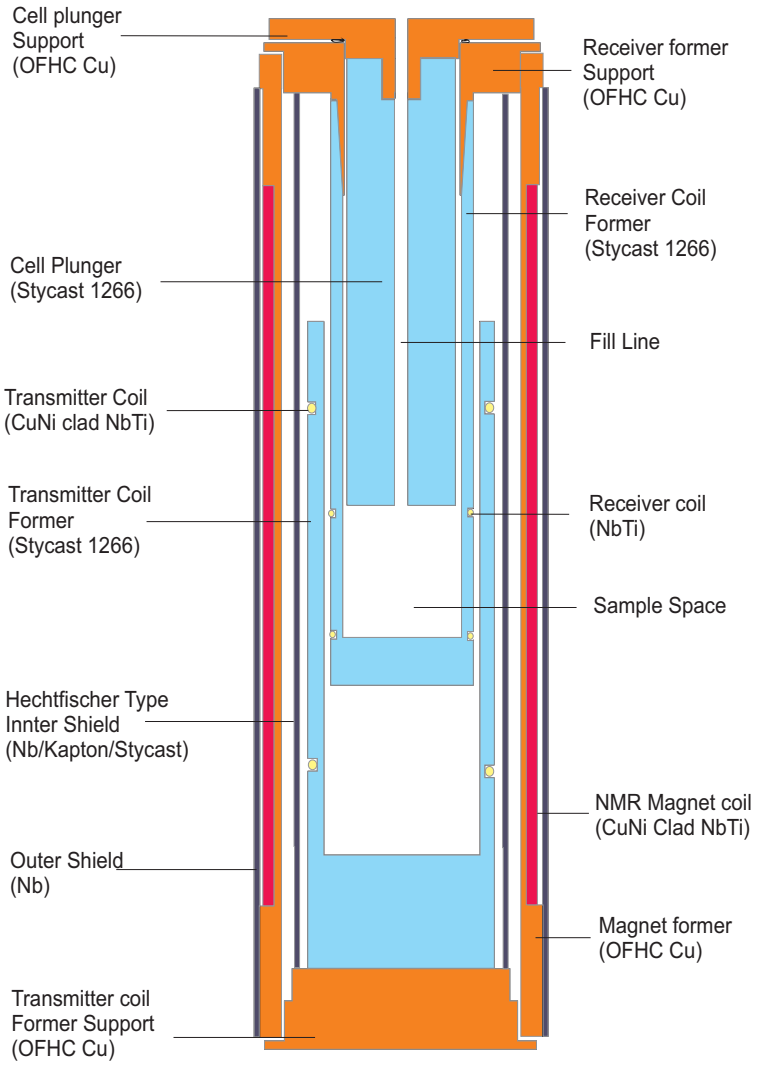

Figure 5.6: Cross-sectional diagram of the NMR assembly.

5.3.6 Shielding

The cell/magnet construction involves two cylindrical niobium shields. Both shields exploit the perfect diagmagnetism of the niobium in its superconducting state to isolate the experiment from external and induced fields. The outer shield consists of a sheet of niobium wrapped around the magnet former and shields the assembly from external magnetic fields, and environmental disturbances. The inner shield is an overlapping type, which is made by taking a sheet of Niobium with a kapton layer and rolling it up like a scroll around a former and set in stycast for stability [157]. This sits outside of the transmitter and inside the NMR magnet former, serving to prevent currents circulating in the Copper NMR magnet former after transmitter pulses. It also has the added benefit of improving the homogeneity of the static B_0 field.

Shielding is present elsewhere in the cryostat; all superconducting lines which carry current to the magnet are housed in Niobium capillary tubing as much as possible, as are the superconducting lines which convey the signal from the receiver coils to the SQUID chip, which itself is housed in a machined Niobium cylinder. The lines of the transmitter coil outside of the cell are housed in CuNi capillary tubing up to the shunt resistor, which is also housed in a Niobium shield cylinder.

5.3.7 The NMR Magnet

One of the key requirements of NMR is that of a constant and stable external magnetic field to polarise the spin system under investigation. In SQUID NMR with broadband detection a stable field is best realised using a shielded superconducting circuit, operated in persistent current mode.

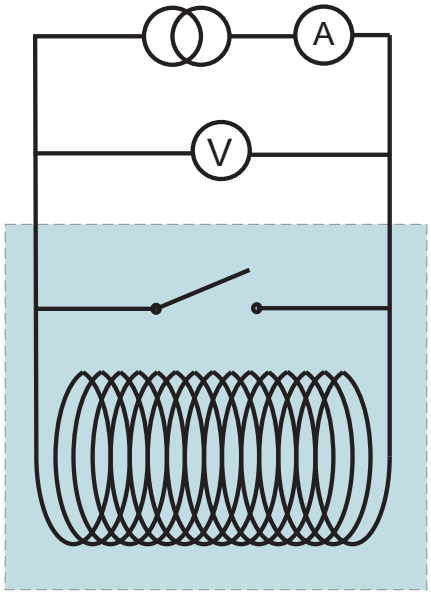

Figure 5.7: Diagram of the circuit to persist the superconducting magnet. The blue region represents the part of the circuit that is inside the IVC. The switch symbol is the persistent switch and is described in the text.

The circuit diagram in figure 5.7 shows the layout of the magnet circuit. The persistent switch is made by coiling superconducting wire around a 470 Ω resistor. The persistent switch is then connected to the magnet via spot welds and thermally anchored directly to the 1 K pot. By applying a voltage across the persistent switch resistor, the superconducting wire coiled around it can be made to go normal allowing current to be put through the NMR magnet. Current is supplied by an Oxford Instruments MK3 stabilised power supply [158], with a voltage trip set to 4 V in case of magnet quenches. The current and voltage across the magnet windings are measured by separate Keithley [159] 2000 multi-meters.

The magnet itself is made from superconducting NbTi wire with CuNi cladding and Formvar insulation from SuperCon inc [160]. The total wire diameter is 106 μm, and the NbTi core diameter is 71 μm. This is then wound in two layers, with 724 turns in each layer, onto the copper magnet former which is also shown in figure

5.6.

The field current ratio and the homogeneity for this a magnet was previously computed by Dr. Ben Yager [102] and found to be 4.62 mT A^{-1} and 400 ppm respectively. However, when the cell is fully assembled, the niobium shields and the graphite sample shift these values from the theoretical calculations. The fully-assembled field current ratio of the magnet is determined empirically by plotting the Larmor frequency of the adsorbed ^{3}He as a function of current in the magnet. Furthermore by plotting the measured T_2^* as a function of frequency, equation 5.15 can then be used to determine the magnet homogeneity. A field ratio of 3.804 mT A^{-1} and a $\Delta B/B_0$ of 315 ppm for the magnet was found.

5.3.8 Transmitter

The cell assembly is made from four distinct pieces; the magnet former, the transmitter, the receiver and the cell plunger. The transmitter slides inside the magnet former, whilst sliding over the receiver coil/sample space assembly. This provides some degree of mechanical decoupling of the receiver from the transmitter, to minimise magneto-acoustic resonances.

The transmitter is wound in a saddle coil configuration, with dimensions to give optimum field homogeneity for such a geometry[161]. To reduce the noise injected via transmitter coil, the transmitter includes a shunt resistor of 100 Ω is connected in parallel to provide a high frequency cut-off at 450 KHz (-3dB point).

5.3.9 Sample Space/Receiver Coil Assembly

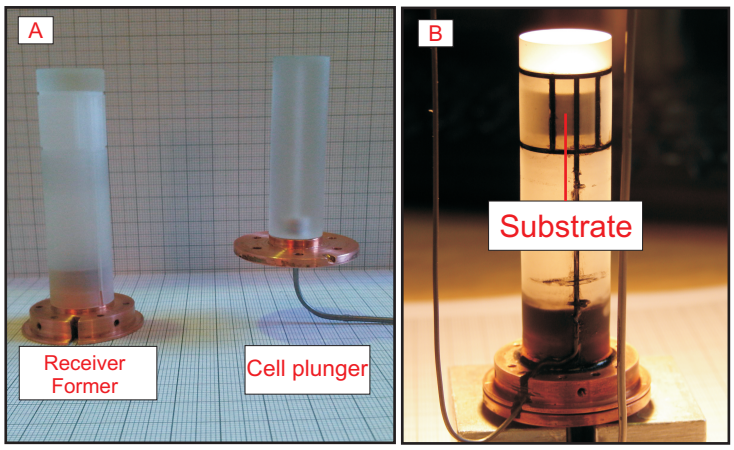

Figure 5.8: Photos of the sample housing components

As can be seen from figure 5.8, the sample housing is made from two separate copper and stycast components; the cell plunger with fill line, and the receiver coil former. Both of these components are constructed from machined stycast 1266 and copper pieces, and form a male-female pair. The adsorption substrate that is loaded into the sample space was an early prototype intended as a test to see if a ^{3}He NMR signal could be observed using this new material. The general method of substrate manufacture is described in chapter 3, where specific details regarding the batch 11-(NMR) substrate manufacture are also given in section 3.6. The substrate consisted of 25 disks or 'foils', each approximately 300 μm in thickness. Before loading, these foils were subjected to further heat treatment of 24 hours at 1000°C under vacuum, to ensure clean adsorbing surfaces. Once the foils were loaded, the sample housing was assembled by inserting the plunger into the receiver coil former, in such a way that the foils are compressed slightly, serving to secure the substrate foils and preventing them from moving due to vibrations. An indium gasket is used

to seal the space where the copper surfaces of the cell plunger and the receiver former meet. The total surface area of the cell as measured by nitrogen isotherm (section 4.2) was found to be 2.80 m^2.

The receiver is wound in a similar saddle geometry as the transmitter, in order to couple to the sample space as best as possible while minimising the deleterious effect of field inhomogeneity over the sample. As with the transmitter its dimensions are optimised as outlined in reference [161]. The windings are NbTi with only a Formvar cladding, as a normal CuNi layer will act as a Johnson noise source.

The receiver forms part of a full superconducting circuit with the input coil of the SQUID. A twisted pair, shielded by Nb tubing leads into the Nb SQUID housing. Connection is made to the SQUID via niobium terminals. A circuit diagram for this along with the SQUID electronics is shown in figure 5.9.

5.3.10 DC SQUID system

Detection of NMR signals is achieved using a sensitive Flux Locked Loop (FLL) two-stage DC SQUID system, which is outlined in figure 5.9 and consists of a SQUID chip manufactured by Physikalisch - Technische Bundesustalt (PTB) used in conjunction with a Magnicon [162] FLL electronics control box. Signals generated in the receiver coil are coupled onto the SQUID by means of a superconducting flux transformer which is routed through a separate STAR-Cryoelectronics [163] Q-spoiler current limiter chip. The Q-spoiler consists of a series array of hysteretic SQUIDs, which is resistive for high currents and superconducting for low currents. This serves to limit high input currents which occur due to cross coupling during a transmitter pulse and helps to improve the spectrometer recovery time after a pulse. The PTB SQUID chip includes an integrated Q-spoiler, however we chose to route through an external Q-spoiler in an attempt to improve recovery times.

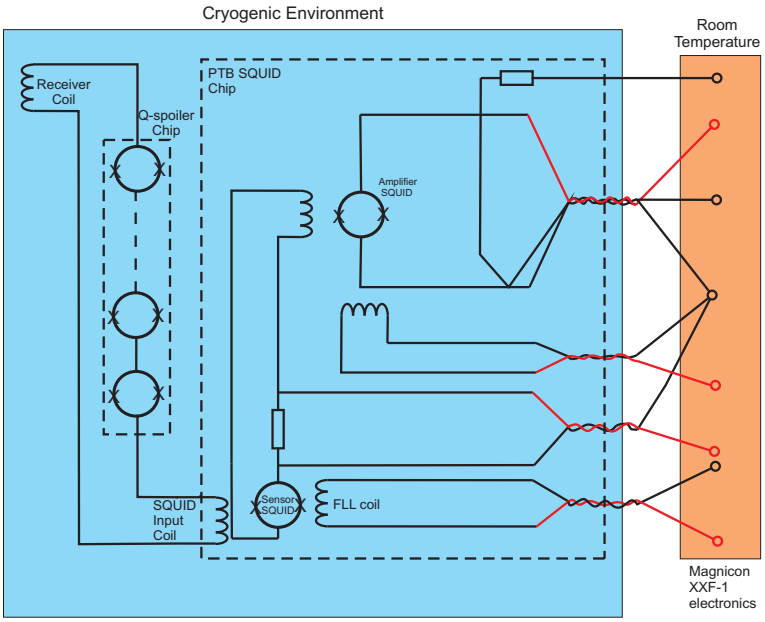

Figure 5.9: Simplified circuit diagram of the NMR detection circuit.

5.3.11 NMR Sequencing and Readout

Pulses though the transmitter were created by means of two Agilent 33220A 20 MHz function/arbitrary waveform generators, and amplified through an Acoustic Research (AR) 75A250 power amplifier. Each of the Agilent waveform generators were triggered by Transistor Transistor Logic (TTL) pulses created by a Stanford Research Systems (SRS) Model DG535 4 channel delay/pulse generator. The SRS delay generator was also used to trigger the FLL electronics of the SQUID and the scope which was receiving the signal from the SQUID electronics. The scope was a National Instruments PXI 5922 digitiser, which was also used to directly record the transmitter pulse. A detailed description of the NMR sequence scheme is given in the next section.

5.4 Procedure

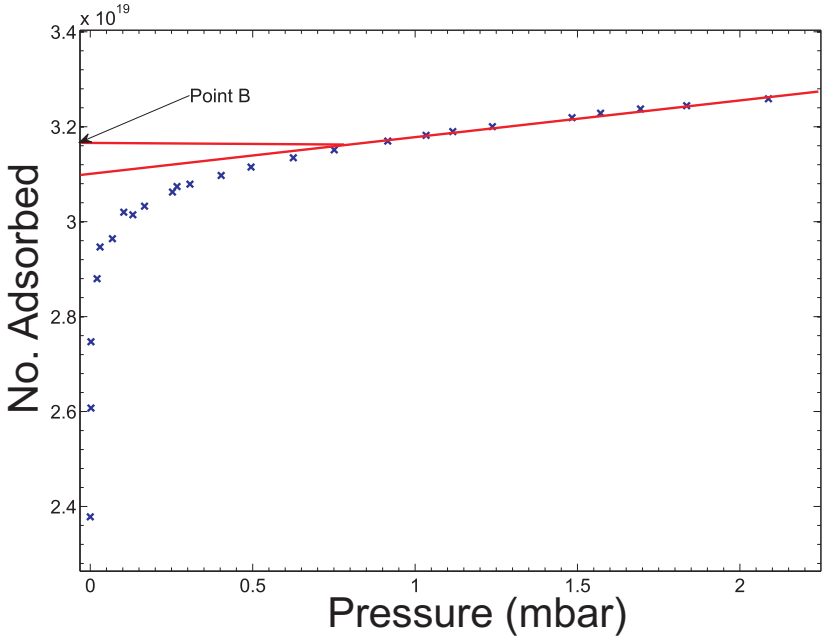

Figure 5.10: ^{3}He adsorption isotherm performed on the sample cell. The 'point-B' indicated on the isotherm is the point at which the isotherm deviates from linearity and is taken to coincide with monolayer completion. The effective dead volume in this measurement was determined to be 169 cm^3. At point B, there are 10.8 atoms per nm^2

After the nitrogen adsorption measurements of section 4.5, it was necessary to evacuate the cell thoroughly to remove any remnant nitrogen any other surface contaminants. After this was completed, the sample cell was cooled down to 4.2 K by filling the main bath of the cryostat with liquid helium. The sample cell can then be dosed with ^{3}He, which will adsorb onto the substrate surface. At this point it should be noted that as the ^{3}He film is grown on the graphite surface, it can form a commensurate $\sqrt{3} \times \sqrt{3}$ solid on the graphite surface. Unlike krypton and nitrogen however, no sub-step is observed marking the completion of the first monolayer and adsorption isotherms of ^{3}He do not display stepwise features in the vapour pressure, instead, once the monolayer is completed the pressure will then

begin to increase linearly, as is shown in figure 5.10. The standard method for determining the point of ^{3}He monolayer completion is to use the so-called 'point-B' of the isotherm, which demarcates the point at which the isotherm diverges from this linearity. In performing a ^{3}He isotherm on the sample cell, we have determined that monolayer completion occurs when 3.16×10^{19} atoms have been adsorbed onto the substrate surface.

On the completion of this isotherm, the cell can now be cooled further and stabilised at 1.4 K. On cooling, all of the ^{3}He that was in the vapour phase during the 4.2 K isotherm, is now adsorbed onto the substrate where it forms as a second monolayer on the graphite surface. At this point, using point-B to define the coverage scale, there is now 1.4 monolayers adsorbed onto the graphite surface. The NMR measurement can now be performed on the adsorbed ^{3}He film.

To begin, current is slowly ramped into the magnet. For the measurements presented here we have chosen to operate at 270 kHz, which corresponds to a magnet current of 2.214 A. As mentioned in section 5.3.11, all aspects of the NMR pulse and measurement sequence is controlled by the SRS delay generator. A diagram of the control scheme is shown in figure 5.11

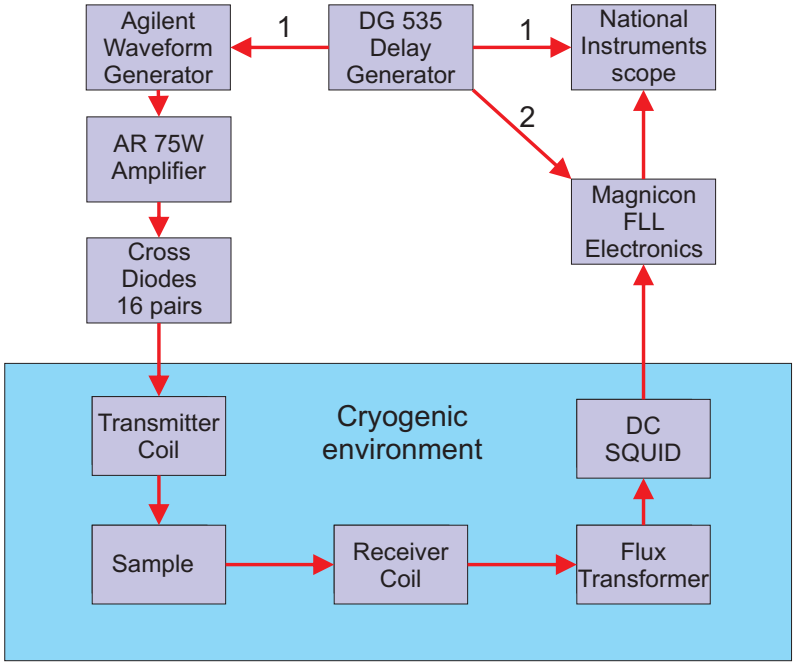

Figure 5.11: Triggering and readout control scheme for the NMR spectrometer. The entire sequence is controlled by the SRS DG535 delay generator; the scope and waveform generator are both simultanously triggered first, and then after a delay of approximately 100 μs, the Magnicon electronics are triggered.

In a single sequence cycle the delay generator triggers the waveform generator and scope simultaneously using TTL pulses. The pulses that were produced by the waveform generator consisted of 10 cycles at 270 kHz, with an amplitude corresponding to a 90° tipping pulse.

For the duration of the NMR pulse, the FLL electronics remain inactive to prevent them from saturating. After the pulse has ended, the delay generator then triggers the FLL electronics to reset, allowing the NMR signal from the sample to captured by the scope. The *recovery time* of the spectrometer is the time delay between the start of the pulse sequence and the FLL reset, where it is preferable to have as short recovery times as possible. The recovery times in these measurements were on the order of 100μs.

This pulse/capture sequence is repeated many times so that the captured signal from the FLL electronics can be averaged to improve the signal to noise ratio. If the pulse rate is too high i.e. the time between pulses is $<5T_1$, then this can manifest as lost signal as the system has not had sufficient time to relax back to equilibrium. Additionally, high pulse rates can cause unwanted sample heating. The pulse repetition rate set by the delay generator was 0.5 Hz, which was chosen as it allowed a large number of averages to be accrued in a short amount of time, with no evidence of lost signal or sample heating.

Using the procedure outlined here, it is possible to capture and record the signal from a large number of pulse sequences. These can then be brought together to produced an averaged time domain signal such as the one shown in figure 5.12, which is the result of averaging some 20000 individual measurements.

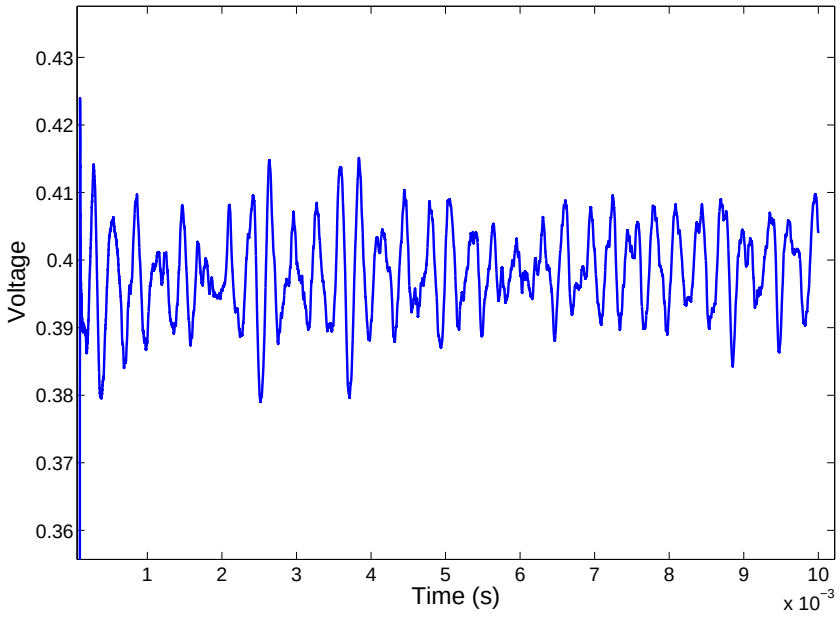

Figure 5.12: Time domain signal, which is the result of some 20000 individual pulse/capture sequences.

In order to extract the ^{3}He NMR signal from this data it is necessary to remove the effect of magneto-acoustic resonances occurring at the Larmor frequency, which serve to obscure the ^{3}He signal. Fortuitously, the size of these resonances has been observed to scale in proportion to B_0^2, which allows for a background subtraction to be performed. This is performed as follows; first the on-resonance time domain signal is obtained which contains the ^{3}He NMR signal. The same pulse sequence is then performed with the NMR field de-tuned to an off-resonance frequency corresponding to the first minimum in pulse power spectrum, which in our case was at 296 kHz. This signal is then scaled by $(B_{on}/B_{off})^2$, before directly subtracting it from the on-resonance time domain signal. This background subtracted signal is then digitally processed using a Savitsky-Golay filter which serves to remove low frequency noise below 25 kHz. This background subtraction and digital filtering results in an observable Free Inudction Decay (FID) similar to that shown in figure 5.13. It is important to note that when performing background measurements, these backgrounds only remain valid for a short time; typically on the order of 24 hours. This meant that off-resonance background measurements were required for every FID obtained.

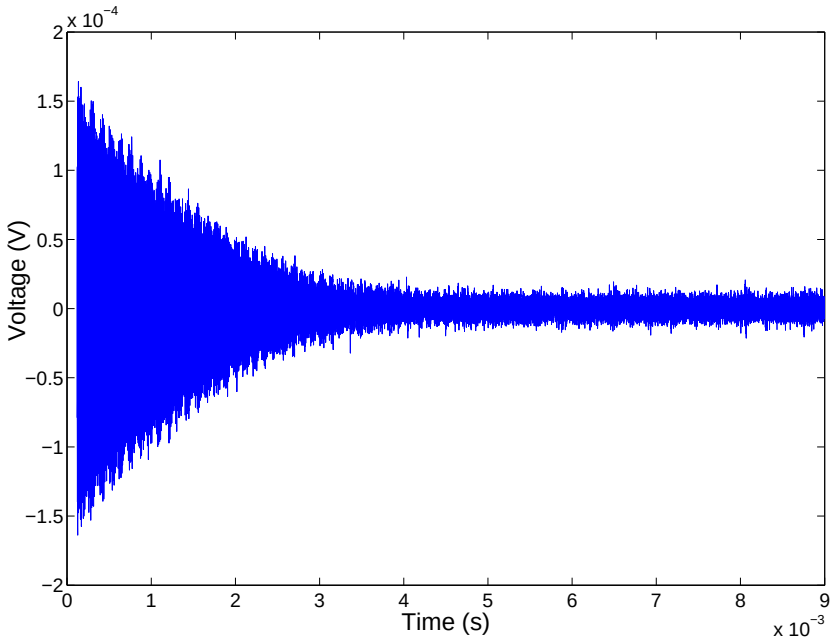

Figure 5.13: Free Induction Decay obtained from figure 5.12 after performing background subtraction and filtering.

Analysis of this FID signal is performed in the frequency domain taking the Fast Fourier Transform of this data. As is discussed in section 5.1.3, the receiver coil captures only M_x component of magnetisation as it precesses, which according to the Bloch equations should result in a signal of the form [150];

$$f(t) = A\cos(\omega_0 t + \phi)\exp(-t/T_2^* \tag{5.18}$$

where ϕ is a phase associated with the recovery time of the measurement. The Fourier transform of this function for $t > 0$ is given by

$$F(\omega) = \frac{\frac{1}{2}AT_2^*\exp(i\phi)}{1 + i(\omega - \omega_0)T_2^*} \tag{5.19}$$

Which in the frequency domain, f is written as

$$F(f) = \frac{\frac{1}{2}AT_2^* \exp(i\phi)}{1 + 2\pi i(f - f_0)T_2^*} \tag{5.20}$$

Using a fitting program written in MATLAB by Frank Arnold, the real and imaginary components of equation 5.20 are fitted using a least squares fittings routine to the FFT of the captured FID, using A, T_2^*, f_0 and ϕ as adjustable parameters. Details of this fitting program can be found in the work of Arnold [164]. Figure 5.14 shows as example of this fitting to the FFT of figure 5.13.

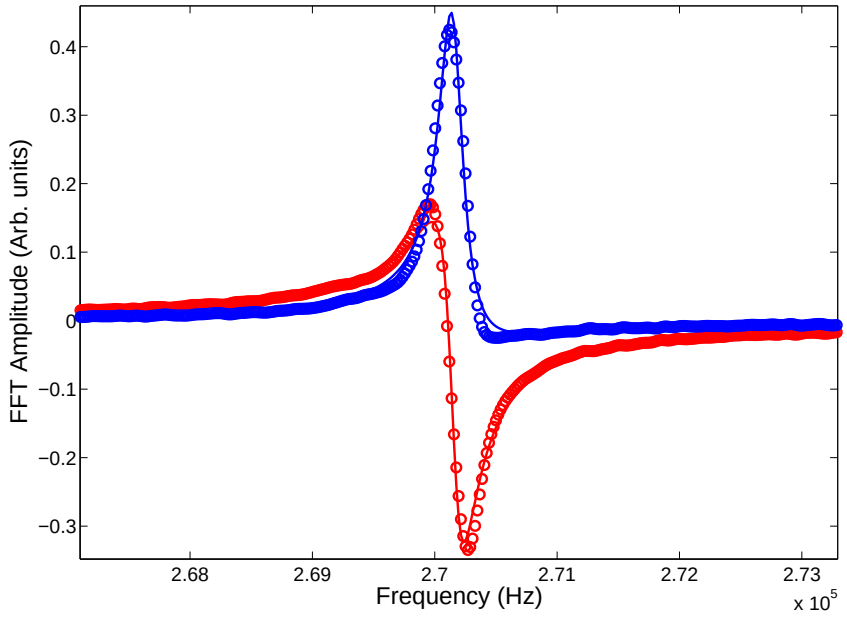

Figure 5.14: Fits to the imaginary (red) and real (blue) components of the FFT of the FID in figure 5.13. The T_2^* parameter of this fit is 1.31 ms.

This procedure to obtain the T_2^* was performed for a range of coverages. As has been stated, the coverage range was varied from 1.4 to 0.65 monolayers. In order to change coverage in this manner, the cell was heated to desorb a portion of the ^{3}He

film. Referring to the gas handling system schematic in figure 5.4, this desorbed gas was allowed to expand into the large volume adjacent to the dosing manifold (small M.F. in the diagram). Once the desired pressure had been reached, the cell was closed off and the contents of the large volume evacuated via turbo-pump. Once this evacuation is complete, the large volume is closed off and the cell allowed to expand into the dosing manifold so that the ^{3}He vapour pressure can be monitored. If necessary heating to the cell is increased so that the observed pressure is greater than 1 mbar. This is a standard protocol at RHUL used to anneal adsorbed films; the pressure is held above 1 mbar for two hours, before slowly cooling down to base temperature to grow the film. T_2^* was measured for a total of 17 coverages. The results of these measurements are presented in the next section.

5.5 Results and Discussion

As can be seen from the top panel of figure 5.15, the observed relaxation times and behaviour are broadly similar to those shown in figure 5.1. This shows that our substrate preparation technique does not significantly effect the magnetic field profile observed by the spins. We have observed that a multilayer ^{3}He film can be grown on this substrate surface with no unusual behaviour; no evidence of bulk formation due to capillaration or other effects can be seen in the isotherm or NMR data.

Technical issues with the spectrometer, combined with multiple subsystems with different relaxation times has resulted in an inability to observe the absolute minimum of the T_2^* cusp. In previous work, T_2^* [8] has been observed to be as short as 100 μs, which is of the same order as the recovery times in this measurement. As can be seen from the lower panel of figure 5.15, in which the magnetisation per particle is plotted as a function of coverage, a large minimum can be seen near monolayer

completion. This minimum arises due to the fact that a large fraction of the signal has decayed before the recovery time of the spectrometer has ended. This lost signal is consistent with the expected T_2^* of 100 μs, and strongly implies that the incomplete T_2^* minimum shown in the top panel is a limitation of the spectrometer and not the substrate.

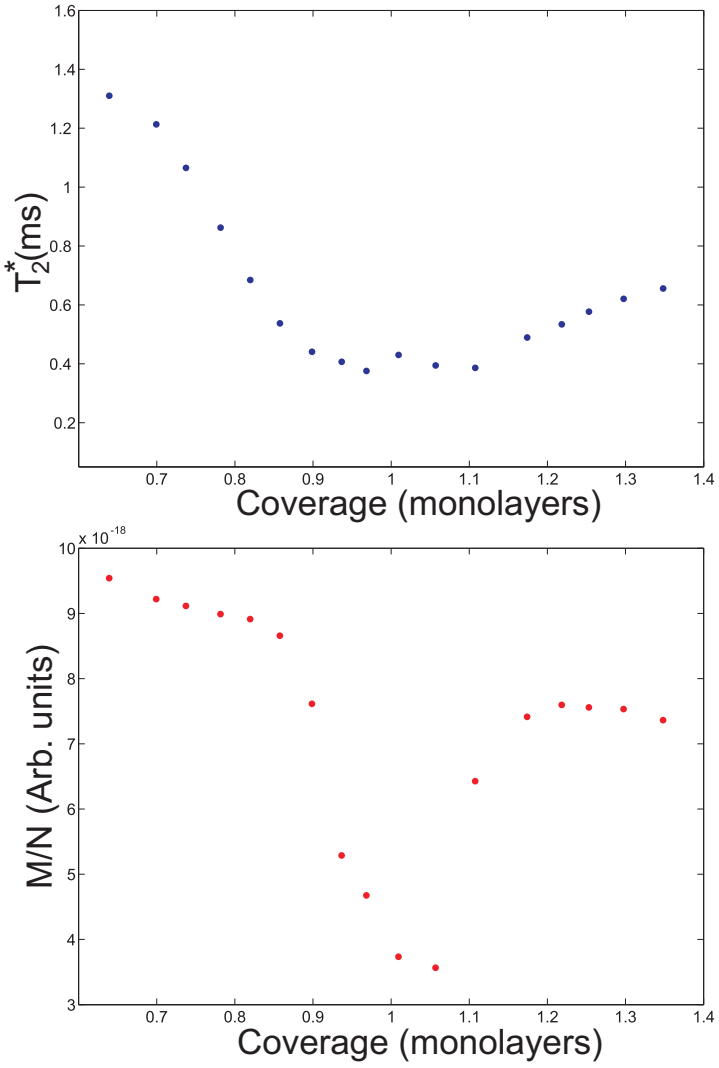

Figure 5.15: Plots showing T_2^* as a function of coverage (top), and average magnetisation per particle, M/N as a function of coverage (bottom).

Chapter 6

Summary and Future Work

The work presented in this thesis has detailed the efforts to make a new, highly homogeneous graphitic substrate. The source material is a Madagascan natural flake graphite, which is measured to be more crystalline than HOPG from optical micrographs and from X-ray diffraction. This material is intercalated with potassium and ammonia and then subjected to relatively low temperatures in an attempt to produce small amounts of exfoliation. Excess intercalant can be driven off without causing further exfoliation if the heating is ramped up slowly. Purity analysis shows that heating at 700°C under vacuum is sufficient to remove most of the intercalant, whilst heat treatment at 1000°C is able to remove all intercalant residues, and in the process further purify the graphite to a point where observed impurities are at a lower concentration than in Grafoil.

The resultant exfoliated material can be pressed into foils using a standard pellet die, and these foils have been characterised primarily using diffraction and volumetric adsorption techniques. Based on the fact that the observed (110) widths of many of our substrates are found to be narrower than those observed from ZYX or Grafoil, it is thought that our prototype substrates are significantly more crystalline than either ZYX or Grafoil. Throughout this project, the substrate crystallinity has been

assumed to be an indicator of surface coherence lengths. Unfortunately, monolayer scattering remains the only effective way of estimating the typical surface coherence lengths of a substrate. Given that this technique has not been applied in this project, we cannot give an estimate as to the surface coherence lengths of our sample.

Adsorption isotherms have been used to accurately characterise the surface areas of relatively small amounts of substrates, where typically the total surface areas have been on the order of 0.1 m^2, with some samples having areas as small as 0.02 m^2. A somewhat novel analysis technique has been applied to nitrogen isotherms performed at 74 K. By using the isotherm to calculate the adsorption potential distribution, it has been possible to make a semi-quantitative comparison of the surface homogeneities of Grafoil and the batch 11 NMR substrate.

Two NMR substrates now exist; the batch 11 NMR substrate, which was exfoliated at 350 °C, and has a specific area of 1.5 m^2/g; and the batch 17 substrate which was exfoliated at a temperature of 230°C, which after successful diffusion bonding to silver foils now has a specific area of 0.95 - 1 m^2/g. The results of chapter 5 show that SQUID-NMR can be successfully performed on an adsorbed ^{3}He film without any indication that the substrate adversely affects the measurement, other than the smaller signal due to reduced surface area. It is expected that the new diffusion bonded substrate, which comprises some 16 bond sandwiches, will have a total surface area of 0.85 m^2

As an estimate of whether an NMR signal can be observed from a such a small total surface area, reference is made to the data in figure 6.1, which is taken from an NMR experiment that is currently in progress on the Nuclear Demagnetisation (ND1) refrigerator at RHUL. The cell being used contains 36 bonded sandwiches similar to those shown in figure 4.27, where Grafoil has been used as the adsorption substrate and has a total cell surface area of 12 m^2. Given that the cell construction for the batch 17 substrate will be identical to the one currently being used, it is

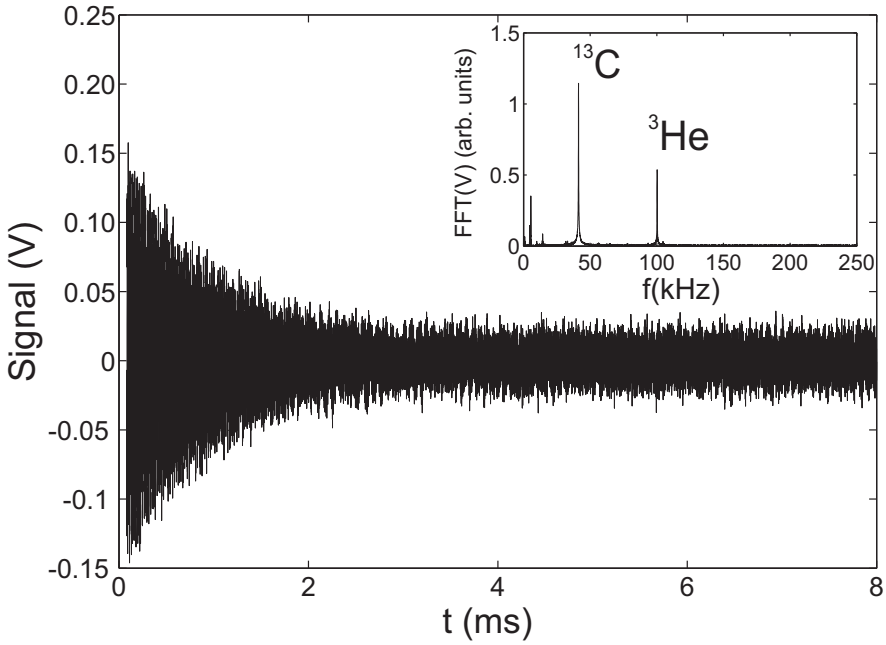

Figure 6.1: FID from the current ULT experiment which is described in detail in [164]. Aspects of this plot are discussed in the text.

reasonable to expect a factor 14 reduction in the signal to noise ratio (12 m^2/0.85 m^2).

The data shown in the figure is pertinent as it represents the smallest signal obtained under normal experimental conditions; the tip angle is 7°, the temperature is 300 mK and the ^{3}He film is at a low coverage of 1.95 atoms nm^{-2}. In addition the FID shown here is composed of only 1000 averages. Despite the unfavourable parameters, the signal to noise ratio of the ^{3}He peak at 100 kHz is found to be 46. Thus it is anticipated, for the exact same measurement performed using the batch 17 substrate, that a signal to noise of 3 will be obtained, which is easily within the measurement criterion established in section 3.5.

There is a wide range of measurements that could be done on the new batch 17 substrate. Naturally, the priority will be to investigate the physics where finite

size effects play an important role. An obvious choice would be to explore the ferromagnetic phase of ^{3}He adsorbed onto graphite [165], as size effects are thought to play a fundamental role. It may also be possible to use NMR measurements to obtain information about the substrate homogeneity; work performed by both Kent [166] and Morhard [167] showed that NMR data on ^{3}He at very low coverages on graphite can be reasonably assumed to be strongly localised, behaving as if it was bound tightly bound at heterogeneities in the graphite substrate. This fact can be used to estimate the number of alternate binding sites on a substrate. In Grafoil, the percentage of alternate binding sites is thought to be on the order of 5 %. Estimating this number for the new batch 17 substrate would be informative.

Appendix A

Transpiration Correction

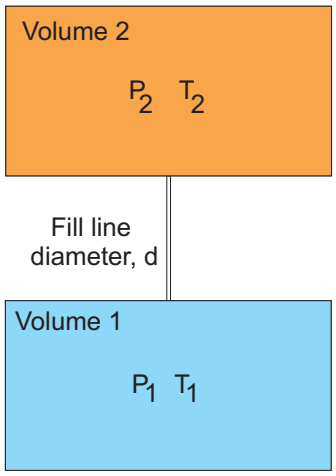

Figure A.1: Schematic of two volumes connected by a thin tube of diameter, d. If the temperatures of the volume is such that $T_2 > T_1$, the observed pressure in volume 2 will slightly larger.

If two volumes, both at some temperature $T_2 = T = T_1$, are connected via a thin tube and filled with gas at a low pressure as in figure A.1, the pressures recorded in

each volume will be the same. If however, the temperature in volume 2 is such that $T_2 > T_1$ then it can be observed that the pressure in volume 2 will be slightly higher. This effect is called transpiration and occurs only at low pressures when the mean free path of the gas molecules in the higher temperature volume is several times that of the tube diameter.

As is described in section 4.2.1, this scenario occurs during an adsorption isotherm measurement where the cell containing the substrate is at 77.3 K, and the pressure gauge is connected to the dosing manifold which is at 300 K. In order to obtain an accurate adsorption isotherm it is therefore necessary to correct for this effect. We have chosen to apply the equation of Takaishi and Sensui [140];

$$\frac{(P_1/P_2) - 1}{\sqrt{T_1/T_2} - 1} = \frac{1}{AX^2 + BX + C\sqrt{X} + 1} \tag{A.1}$$

Where P_1,T_1 and P_2,T_2 are the pressures and temperatures in the cell and dosing manifold respectively. X is equal to $2P_2d/(T_1 + T_2)$ with d, the diameter in mm of the connecting fill line. This expression is valid for $T_2 > T_1$. The factors A,B and C are gas specific constants, where some relevant values can be found in table A.1. To use this equation all pressures should be converted to mm Hg.

Gas	A	B	C	T Range (K)
N_2	12×10^5	10×10^2	15	77 - 195
Kr	14.5×10^5	15.0×10^2	13.7	77 - 673
He	1.5×10^5	1.2×10^2	19	4.2 - 90

Table A.1: Transpiration correction constants for equation A.1 for nitrogen, krytpon and helium gas from Takaishi and Sensui [140]

Appendix B

(110) Fit Parameters

In section 4.1, a method has been described to estimate the crystallinity of manufactured substrates to allow for comparison with the previous substrates, Grafoil and ZYX using the broadening of the (110) diffraction peak. A key step in the analysis of this line broadening is to fit two Voigt functions, one to each peak of the diffracted K_α doublet. The larger $K_{\alpha 1}$ peak is used for analysis, after the instrument broadening contribution has been unfolded from the peak through the use of a standard. The standard measurement that is used to correct for instrument broadening in the (110) line is shown in figure 4.5 and the necessary width parameters from the $K_{\alpha 1}$ fit given in table 4.2. The width parameters from the Voigt fits to the $K_{\alpha 1}$ are presented here. The Gaussian (f_g^m), Lorentzian (f_l^m) and full Voigt (f_v^m) width parameters of the fit to the measured profile are presented alongside their corresponding deconvolved width components (f_g^s,f_l^s,f_v^s). A crystallite size estimate L has been calculated using the Scherrer equation, and the f_v^s value as the observed width. This calculation neglects any strain contributions.

Sample	T_E(°C)	f_g^m	f_l^m	f_v^m	f_g^s	f_g^s	f_g^s	L (Å)
Grafoil	-	0.1201	0.097	0.1580	0.1174	0.0681	0.1580	672
-	-	0.1404	0.0551	0.1722	0.1381	0.026	0.1526	697
-	-	0.1273	0.09289	0.18406	0.1247	0.0638	0.1623	655
-	-	0.1273	0.09289	0.18406	0.1247	0.0638	0.1623	655
-	-	0.01	0.1168	0.1762	0.0967	0.0877	0.1518	700
-	-	0.1307	0.0811	0.1794	0.1282	0.052	0.1583	671
-	-	0.1449	0.0889	0.1983	0.1427	0.0598	0.1774	599
-	-	0.1729	0.0337	0.1917	0.1711	0.0046	0.1736	612
-	-	0.1368	0.062	0.173	0.1345	0.0329	0.1529	695
ZYX	-	0.1323	0.03376	0.1513	0.1299	0.0047	0.1324	803
-	-	0.129	0.0295	0.1455	0.1265	0.0004	0.12669	839
-	-	0.1333	0.0352	0.1531	0.1309	0.0061	0.1342	792
HOPG	-	0.0819	0.0336	0.10138	0.0779	0.0046	0.0803	1323
-	-	0.0761	0.0303	0.0936	0.0718	0.0012	0.0724	1468
-	-	0.0542	0.0448	0.082	0.0478	0.0158	0.0568	1871
4H	700	0.1692	0.048	0.1964	0.1673	0.019	0.1777	598
-	-	0.1602	0.049	0.1881	0.1581	0.0202	0.1692	628
5E	400	0.0728	0.0313	0.0910	0.0682	0.0023	0.069412	1532
-	-	0.0631	0.04116	0.0879	0.0577	0.0121	0.0644	1650
-	-	0.06012	0.0417	0.0855	0.0545	0.0126	0.0616	1727
6A	400	0.1434	0.0386	0.1651	0.1411	0.0095	0.14627	727
-	-	0.14337	0.04	0.166	0.1411	0.011	0.1471	723
6C	350	0.1312	0.0326	0.1496	0.1288	0.0036	0.13066	813
-	-	0.1274	0.0372	0.1485	0.1249	0.0081	0.1293	822
-	-	0.128	0.0302	0.1457	0.1262	0.0011	0.1268	838
6D	250	0.0967	0.0300	0.1137	0.0933	0.001	0.0937	1134
-	-	0.075	0.0638	0.1148	0.0706	0.0347	0.0910	1169

Table B.1: Fit parameters part I. All widths are in degrees.

Sample	T_E(°C)	f_g^m	f_l^m	f_v^m	f_g^s	f_g^s	f_g^s	L (Å)
8A	250	0.03115	0.0815	0.0927	0.018	0.0525	0.0584	1820
-	-	0.04424	0.0723	0.0942	0.0362	0.0433	0.0645	1647
8B	225	0.0695	0.0554	0.1037	0.0646	0.0263	0.0799	1331
8C	220	0.1139	0.0523	0.1444	0.111	0.0232	0.124	858
8D	200	0.1284	0.0479	0.1559	0.1259	0.0188	0.1369	780
8E	225	0.0973	0.0251	0.1139	0.0939	0.0039	0.0918	1158
-	-	0.0606	0.0595	0.0984	0.055	0.0304	0.0730	1456
9A	200	0.1256	0.0361	0.1460	0.123	0.007	0.1269	838
-	-	0.1289	0.0340	0.1482	0.1264	0.0049	0.1290	824
-	-	0.11	0.0334	0.1290	0.107	0.0043	0.10938	972
9B	190	0.0896	0.0336	0.1103	0.0849	0.0068	0.0886	1199
-	-	0.0720	0.0502	0.1026	0.0661	0.0213	0.0782	1359
-	-	0.0870	0.0410	0.1110	0.0822	0.0121	0.088	1197
11-(NMR)	350	0.1144	0.03114	0.1319	0.1115	0.0021	0.1126	944
-	-	0.1197	0.0296	0.1364	0.1171	0.0005	0.1173	906
-	-	0.1023	0.047	0.1297	0.0991	0.0181	0.1091	974
-	-	0.1290	0.0302	0.1467	0.1272	0.0012	0.1279	831
14A	200	0.1237	0.0376	0.1450	0.1203	0.0087	0.1250	850
-	-	0.1189	0.0361	0.1394	0.1154	0.0071	0.1193	870

Table B.2: Fit parameters part II

Bibliography

[1] R.E. Peierls. In: *Ann. Inst. Henri Poincare* 5 (1935), pp. 177–222.

[2] N.D. Mermin and H. Wagner. "Absence of Ferromagnetism or Antiferromagnetism in One- or Two-Dimensional Isotropic Heisenberg Models". In: *Phys. Rev. Lett.* 17.2 (1966), pp. 1133–1136.

[3] V.L. Berezinskii. "Destruction of Long-Range order in One-Dimensional and Two-Dimensional Systems having a Continuous Symmetry Group I. Classical systems". In: *Sov. Phys. JETP* 32.3 (1970), pp. 493–500.

[4] J.M. Kosterlitz and D.J. Thouless. "Ordering, Metastability and Phase Transitions in Two-Dimensional Systems". In: *J. Phys. C.: Sol. State. Phys.* 6 (1973), pp. 1181–1203.

[5] D.J. Bishop and J.D. Reppy. "Study of the Superfluid Transition in Two-Dimensional ^{4}He Films". In: *Phys. Rev. Lett.* 40 (26 1978), pp. 1727–1730.

[6] R.J. Birgeneau, P.A. Heiney, and J.P. Pelz. "High resolution X-ray studies of monolayer krypton on varied forms of graphite". In: *Physica B+C* 109-110, Part 3.0 (1982), pp. 1785 –1795.

[7] R.J. Birgeneau and P.M. Horn. "Two-Dimensional Rare Gas Solids". In: *Science* 232 (1986), pp. 329–336.

[8] J. R. Owers-Bradley. "The Properties of Helium Adsorbed on Graphite: An NMR Study". PhD thesis. University of Sussex, 1978.

[9] O.K. Farha et al. "Metal-Organic Framework Materials with Ultrahigh Surface Areas: Is the Sky the Limit?" In: *J. Am. Chem. Soc.* 134 (36 2012), pp. 15016–15021.

[10] K. S. W. Sing et al. "Reporting physisorption data for gas/solid systems with special reference to the determination of surface area and porosity". In: *Pure Appl. Chem* 57.4 (1985), pp. 603–619.

[11] S. Brunauer et al. "On a Theory of the van der Waals Adsorption of Gases". In: *J. Am. Chem. Soc.* 62.7 (1940), pp. 1723–1732.

[12] R.H. Fowler and E.A. Guggenheim. *Statistical Thermodynamics*. Cambridge University Press, 1939.

[13] G. Halsey. "Physical Adsorption on Non-Uniform Surfaces". In: *J. Chem. Phys.* 16 (1948), p. 931.

[14] T.L. Hill. "Statistical Mechanics of Multimolecular Adsorption. III. Introductory Treatment of Horizontal Interactions. Capillary Condensation and Hysteresis". In: *J. Chem. Phys.* 15 (11 1947), p. 767.

[15] Development of Stepwise Isotherms on Carbon Black Surfaces. "M.H. Polley, W.D. Schaeffer and W.R. Smith". In: *J. Phys. Chem.* 57.4 (1953), pp. 469–471.

[16] S. Ross and H. Clark. "On Physical Adsorption. VI. Two-Dimensional Critical Phenomena of Xenon, Methane and Ethane Adsorbed Separately on Sodium Chloride". In: *J. Am. Chem. Soc.* 76.17 (1954), pp. 4291–4297.

[17] M. Matecki, A. Thomy, and X. Duval. In: *C.R. Acad. Sci. Paris* 274 (1972), p. 15.

[18] Y. Larher. "Bidimensional Condensation in Adsorbed Layers". In: *J. Phys. Chem.* 72.5 (1968), pp. 1847–1848.

[19] X. Duval and A. Thomy. In: *C.R. Acad. Sci. Paris* 259 (1964), p. 4007.

[20] A. Thomy, X. Duval, and J. Regnier. "Two-Dimensional Phase Transitions as Displayed by Adsorption Isotherms on Graphite and Other Lamellar Solids". In: *Surf. Sci. Rep.* 1.1 (1981), pp. 1–38.

[21] J. G. Dash. "Between Two and Three Dimensions". In: *Endeavour* 6.1 (1982), pp. 15–22.

[22] Grafoil is a product of GrafTech International Advanced Electronics Technology, 11709 Madison Ave. Lakewood, OH 44107 United States, formerly UCAR - http://www.graftech.com.

[23] Papyex is a product of Mersen S.A., Immeuble La Fayette, 2 place des Vosges, Courbevoie La Defense 5, Paris, 92400, France - Formerly Le Carbone Lorraine.

[24] J.K. Kjems et al. "Neutron Scattering from Nitrogen Adsorbed on Basal-Plane-Oriented Graphite". In: *Phys. Rev. Lett.* 32.13 (1974), pp. 724–728.

[25] J.K. Kjems et al. "Neutron Scattering from Nitrogen Adsorbed on Basal-Plane-Oriented Graphite". In: *Phys. Rev. B* 13.4 (1976), pp. 1446–1462.

[26] P. Vora, S.K. Sinha, and R.K. Crawford. "Neutron-Diffraction Study of Phases of CD_4 Monolyaer films on Graphite". In: *Phys. Rev. Lett.* 43.10 (1979), pp. 704–708.

[27] S.E. Nagler et al. "Orientational order in Xenon Fluid Monolayers on Single Crystals of Exfoliated Graphite". In: *Phys. Rev. B* 32.11 (1985).

[28] D.R. Nelson and B.I. Halperin. "Dislocation-Mediated Melting in Two Dimension". In: *Phys. Rev. B* 19.5 (1978), pp. 2457–2484.

[29] E.A. Wood. "Vocabulary of Surface Crystallography". In: *J. Appl. Phys.* 35.4 (1964), pp. 1306–1312.

[30] R.I. Masel. *Principles of Adsorption and Reaction on Solid Surfaces*. John Wiley and Sons, 1996.

[31] H.P.R. Frederikse. "On the Specific Heats of Adsorbed Helium". In: *Physica* 15.10 (1949), pp. 860–862.

[32] M. Bretz. "Heat Capacity of Multilayer ^{4}He on Graphite". In: *Phys. Rev. Lett.* 31.24 (1973), pp. 1447–1450.

[33] P. A. Crowell and J. D. Reppy. "Superfluidity and film structure in 4He adsorbed on graphite". In: *Phys. Rev. B* 53.5 (1996), pp. 2701–2718.

[34] J. Nyeki et al. "Superfluidity of Atomically Layered ^{4}He Films". In: *Phys. Rev. Lett.* 81.1 (1998), pp. 152–155.

[35] D.D. Osheroff, W.J. Gullyand R.C. Richardson, and D.M. Lee. "New Magnetic Phenomena in Liquid ^{3}He below 3 mK". In: 29.14 (1972), pp. 920–923.

[36] J. Xu and B.C. Crooker. "Very Thin Films of ^{3}He: A New Phase". In: *Phys. Rev. Lett.* 65.24 (1990), pp. 3005–3008.

[37] L. V. Levitin et al. "Phase Diagram of the Topological Superfluid ^{3}He Confined in a Nanoscale Slab Geometry". In: *Science* 340.6134 (2013), pp. 841–844.

[38] R.G. Bennett et al. "Superfluid ^{3}He Confined to a Single 0.6 Micron Slab Stability and Properties of the A-Like Phase Near the Weak Coupling Limit". In: *J. Low. Temp. Phys.* 158 (2010), pp. 163–169.

[39] M. J. Lea, D. S. Spencer, and P. Fozooni. "Healing Lengths Near T_λ in Liquid Helium". In: *Jpn. J. Appl. Phys.* 26 (1987), p. 53.

[40] J.J. Metois, J.C. Heyraud, and Y. Takeda. "Experimental Conditions to Obtain Clean Graphite Surfaces". In: *Thin Solid Films* 51 (1978), pp. 105–117.

[41] G.E. Bacon. "The interlayer spacing of graphite". In: *Acta Crystallographica* 4 (6 1951), pp. 558–561.

[42] K.S. Novoselov et al. "Electric Field Effect in Atomically Thin Carbon Films". In: *Science* 306.5696 (2004), pp. 666–669.

[43] M.E. Huster et al. "Structure of high stage potassium intercalated graphite". In: *Phys. Rev. B* 35 (1987), pp. 3311–3326.

[44] M.S. Dresselhaus and G. Dresselhaus. "Intercalation compounds of graphite". In: *Advances in Physics* 30.2 (1981), pp. 139–326.

[45] W. Ruedorff and E. Schultze. In: *Z. Anorg. Allg. Chem.* 277 (3-4 1954), pp. 156–171.

[46] J. Purewal et al. "Hydrogen Diffusion in Potassium Intercalated GRaphite Studied by Quasielastic Neutron Scattering". In: *J. Chem. Phys.* 137.224704 (2012).

[47] D.E. Nixon and G.S. Parry. "Formation and Structure of the Potassium Graphites". In: *J. Phys. D: Appl. Phys.* 1.3 (1968), p. 291.

[48] A. Lovell. "Tuneable Graphite Intercalates for Hydrogen Storage". PhD thesis. University College London, University of London, 2005.

[49] T. Maluangnont, M.M. Lerner, and K. Gotoh. "Synthesis of Ternary and Quaternary Graphite Intercalation Compounds Containing Alkali Metal Cations and Diamines". In: *Inorg. Chem* 50.22 (2011), pp. 11676 –11682.

[50] D.D.L. Chung, G. Dresselhaus, and M.S. Dresselhaus. "Intralayer Crystal Structure and Order-Disorder Transformations of Graphite Intercalation Compounds using Electron Diffraction Techniques". In: *Mater. Sci. Eng.* 31.= (1977), pp. 107–114.

[51] M.B. Hannay et al. "Superconductivity in Graphitic Compounds". In: *Phys. Rev. Lett.* 14 (1965), pp. 225–226.

[52] T.E. Weller et al. "Superconductivity in the Intercalated Graphite Compounds C_6Yb and C_6Ca". In: *Nat. Phys.* 1 (2005), pp. 39–41.

[53] G.M.T. Foley et al. "Room Temperature Electrical Conductivity of a Highly Two Dimensional Synthetic Metal: AsF_5-Graphite". In: *Solid state Comm.* 24.5 (1977), pp. 371–375.

[54] A. Catheline et al. "Graphene solutions". In: *Chem. Comms.* 47.19 (2011), pp. 5470–5472.

[55] E.M. Milner et al. "Structure and Morphology of Charged Graphene Platelets in Solution by Small-Angle Neutron Scattering". In: *J. Am. Chem. Soc.* 134.20 (2012), pp. 8302–8305.

[56] T. Enoki. *Graphite Intercalation Compounds and Applications*. Oxford University Press, 2003.

[57] C.Mazieres et al. "Mobility of Bromine in its Graphite and Pyrocarbon Residue Compounds". In: *Carbon* 13.4 (1975), pp. 289–292.

[58] R. Clarke et al. "A new adsorption substrate: Single crystal exfoliated graphite". In: *J. Appl. Phys.* 55 (4 1984), pp. 1231–1233.

[59] D.D.L. Chung. "Intercalate Vaporization During the Exfoliation of Graphite Intercalated with Bromine". In: *Carbon* 25.3 (1987), pp. 361–365.

[60] S. Kim and L.T. Drzal. "High Latent heat storage and high thermal conductive phase change materials using exfoliated graphite". In: *Sol. Energ. Mat. Sol. Cells* 93 (2009), pp. 136–142.

[61] J.W. Aylesworth US patent 1 191383 (1916).

[62] W.H. Martin and J.E. Brocklehurst. "The Thermal Expansion Behaviour of Pyrolytic GRaphite-Bromine Residue Compounds". In: *Carbon* 1 (1964), pp. 133–141.

[63] S.H. Anderson and D.D.L. Chung. "Exfoliation of Intercalated Graphite". In: *Carbon* 22.3 (1984), pp. 253–263.

[64] J.G. Hooley. "A Sealed-Edge Theory of Graphite Compounds". In: *Nature* 190 (1961), pp. 529–530.

[65] D.D.L. Chung. "Exfoliation of graphite". In: *J. Mat. Sci.* 22.12 (1987), pp. 4190–4198.

[66] M. Inagaki, F. Kang, and M. Toyoda. "Exfoliation of Graphite Via Intercalation Compounds". In: *Chemistry and Physics of Carbon Vol. 29*. Ed. by L.R. Radovic. Marcel Dekker, 2004.

[67] B.E. Warren. "X-ray Diffraction in Random Layer Lattices". In: *Phys. Rev.* 59.9 (1941), pp. 693–698.

[68] S.E. Nagler et al. "Observation of a Metastable State in Monolayers of Carbon Tetrafluoride on Graphite". In: *Phys. Rev. B* 39.4 (1989), pp. 2826–2829.

[69] H. Godfrin and H.J. Lauter. In: *Prog. Low Temp. Phys.* 14 (4 1995), pp. 213–320.

[70] C. Bockel, J.P. Coulomb, and N. Dupont-Pavlovsky. "Comparison of the Adsorptive Properties of Papyex and Uncompressed Exfoliated Graphite". In: *Surf. Sci.* 116.2 (1982), pp. 369–379.

[71] M.B. Dowell. "A New Substrate for Surface Studies". In: *Extended Abstracts and Program-Biennial Conference on Carbon vol. 13* (1977).

[72] B.I. Barker. "Spin Dynamics of Superfluid ^{3}He in Aerogel". PhD thesis. Stanford University, 1999.

[73] Y. Niimi et al. "Characterization of ZYX Exfoliated Graphite for Studies of Monolayer ^{3}He Below 1 mK". In: *Rev. Sci. Inst.* 74.10 (2003), pp. 4448–4452.

[74] E.P. Gilbert, P. A. Reynolds, and J. W. White. "Characterisation of a basal-plane-oriented graphite". In: *J. Chem. Soc., Faraday Trans.* 94.13 (1998), pp. 1861–1868.

[75] Y. Kuga et al. "Laser-Assisted Exfoliation of Potassium-Ammonia-Graphite Intercalation Compounds". In: *Carbon* 31 (1993), pp. 201–204.

[76] B. R. York and S. A. Solin. "Effect of composition on charge exchange, lattice expansion and staging in potassium-ammonia graphite intercalated compounds". In: *Phys. Rev. B* 31.12 (1985), pp. 8206–8220.

[77] Nanotech innovations, Department of Physics, Michigan Technological University, 1400 Townsend Drive, Houghton, Michigan, 49931-1295.

[78] S. Liu and C.R. Loper. "Kish a source of crystalline graphite". In: *Carbon* 29 (8 1991), pp. 1119–1124.

[79] S. Liu and C.R. Loper. "The formation of Kish Graphite". In: *Carbon* 29 (4 1991), pp. 547–555.

[80] Y. Hishiyama and A. Ono. "Low Temperature Anomalies in Thermolelectricity of Highly Oriented Graphite in Relation to Sample Quality". In: *Carbon* 23.4 (1985), pp. 445–448.

[81] A. Yoshida and Y. Hishiyama. "Electron Channeling Effect on Highly Oriented Graphites - Size Evaluation and Oriented Mapping of Crystals". In: *J. Mater. REs.* 7.6 (1992), pp. 1400–1405.

[82] M. Morishita. "Surface Observation and Magnetization Measurements of Grafoil Substrate". In: *J. Low Temp. Phys.* 162.1 (2011), pp. 638–644.

[83] J. Hubbard. "The Magnetism of Iron". In: *Phys. Rev. B* 19.5 (1979), pp. 2626–2636.

[84] L.I. Abou-El-Nasr. "NMR Study of ^{3}He Adsorbed on Exfoliated Graphite". PhD thesis. Royal Holloway, University of London, 1989.

[85] Y. Iye, L.E. McNeil, and G. Dresselhaus. "Effect of Impurities on the Electronic Phase Transition in Graphite in the Magnetic Quantum Limit". In: *Phys. Rev. B* 30.12 (1984), pp. 7009–7015.

[86] The Condensed Matter and Material Physics group at University College London under the supervision of Neal Skipper.

[87] D.V. Kosynkin et al. "Longitudinal unzipping of carbon nanotubes to form graphene nanoribbons". In: *Nature* 458 (2009), pp. 872–876.

[88] J.L. Li et al. "Oxygen-Driven Unzipping of Graphitic Materials". In: *Phys. Rev. Lett.* 96 (2006), pp. 176101–.

[89] Y. Shin et al. "The oxidation mechanism of highly ordered pyrolytic graphite in a nitric acid/sulfuric acid mixture". In: *Carbon* 52 (2013), pp. 493–498.

[90] X.W. Qian, D.R. Stump, and S.A. Solin. "Structural Properties of Potassium-Ammonia Liquids in Graphite". In: *Phys. Rev. B* 33.8 (1986), pp. 5756–5769.

[91] J.K. Walter, N.T. Skipper, and A.K. Soper. "The interlayer structure of a graphite-potassium-ammonia intercalation compound by neutron diffraction". In: *Chem. Phys. Lett.* 300 (1999), pp. 444–450.

[92] M.Braun Inertgas-Systeme GMBH, Dieselstr. 31, D-85748 Garching, Germany - http://http://www.mbraun.com.

[93] Schott Uk Ltd., Drummond Road, Stafford, ST16 3EL United Kingdom - http://www.schott.com.

[94] S.K. Hark, B.R. York, and S.A. Solin. In: *Synthetic Metals* 7 (3-4 1983), pp. 257–262.

[95] A. Herold. "Recherches sur les composes d'insertion du graphite". In: *Bull. Soc. Chim. Fr.* 187 (1955), pp. 999–1004.

[96] S. Hendricks and E. Teller. "X-ray Interference in Partially Ordered Layer Lattices". In: *J. Chem. Phys.* 10.3 (1942), pp. 147–167.

[97] T. Ida and K. Kimura. "Effect of sample transparency in powder diffractometry with Bragg–Brentano geometry as a convolution". In: *J. Appl. Cryst.* 32.5 (1999), pp. 982–991.

[98] G. Furdin. "Exfoliation Process and Elaboration of New Carbonaceous Materials". In: *Fuel* 77.6 (1998), pp. 479–485.

[99] M. Klatt et al. "Etude de l'exfoliation des composes d'insertion graphite-trioxide de soufre". In: *Carbon* 24.6 (1986), pp. 731–735.

[100] W.J. Nuttall et al. "A Synchrotron X-ray Diffraction Study of the Structural Phase Behaviour of Multilayer Xenon on Single-Crystal Graphite". In: *J. Phys. Condens. Matter* 5 (1993), pp. 8159–.

[101] E.D. Specht et al. "Phase Diagram and Phase Transistions of Krypton on Graphite in the Extended Monolayer Regime". In: *EPJ B* 69.2-3 (1987), pp. 347–377.

[102] B. Yager. "A Pulsed NMR Study of ^{3}He Adsorbed on Bare and ^{4}He Preplated MCM-41 using DC SQUID Detection". PhD thesis. Royal Holloway, University of London, 2010.

[103] A.J. Casey. "Two Dimensional ^{3}He Adsorbed on Grafoil Plated with a Bilayer of HD". PhD thesis. 2001.

[104] A. Shibahara. "Low Field DC SQUID NMR on Room Temperature Samples and Single Crystal UPt_3". PhD thesis. Royal Holloway, University of London, 2010.

[105] C. Lusher - Private Communication.

[106] Physikalisch - Technische Bundesustalt http://www.ptb.de/indexen.html.

[107] L. Gou. "Magnetization Study of Two Dimensional Helium Three". PhD thesis. University of Southern California, 2010.

[108] http://www.panalytical.com.

[109] W. Soller. "A New Precision X-ray Spectrometer". In: *Phys. Rev.* 24 (1924), pp. 158–167.

[110] R.E. Dinnebier. *Powder Diffraction: Theory and Practise*. Royal Society of Chemistry, 2088.

[111] P. Scherrer. "The interlayer spacing of graphite". In: *Goettinger Nachrichten Gesellschaft* 2 (98 1918).

[112] H.P. Klug and L.E. Alexander. *X-ray Diffraction Procedures for Polycrystalline and Amorphous Materials*. Wiley, 1974.

[113] B.E. Warren. *X-ray Diffraction*. Dover Science, 1990.

[114] A.R. Stokes and A.J.C. Wilson. "The Diffraction of X-rays by Distorted Crystal Aggregates -I". In: *Proc. Phys. Soc.* 56.3 (1944), pp. 174–.

[115] G.K. Williamson and W.H. Hall. "X-ray Line Broadening From Filed Aluminium and Wolfram". In: *Acta Metall.* 1.4 (1953), pp. 22–31.

[116] D. Balzar and H. Ledbetter. "Voigt-function modeling in Fourier analysis of size- and strain-broardened x-ray diffraction peaks". In: *J. Appl. Cryst.* 26 (1993), pp. 97–103.

[117] B.E. Warren and B.L. Averbach. "The Effect of Cold-Work Distortion on X-Ray Patterns". In: *J. Appl. Phys.* 21 (1950), pp. 595–.

[118] E.J. Mittemeijer and P. Scardi. In: *Diffraction Analysis of The Microsctructure of Materials*. Springer Series in Material Science. Springer science, 2003, pp. –.

[119] R.L. Snyder, J. Fiala, and H.J. Bunge. In: *Defect and Microstructure Analysis by Diffraction*. Oxford University Press, 2000.

[120] T. Ida. "Model Peak Profile Functions For Powder Diffractometry as Convolutions With Instrumental Functions". In: *Rigaku Journal* 19.1 (2002), pp. 47–56.

[121] T. Ida, H. Hibino, and H. Toraya. "Deconvolution of Instrumental Aberrations for Synchrtron Powder X-ray Diffractometry". In: *J. Appl. Cryst.* 36.2 (2003), pp. 181–187.

[122] T. Ida and H. Toraya. "Deconvolution of the Instrumental Functions in Powder X-ray Diffractometry". In: *J. Appl. Cryst.* 35.1 (2002), pp. 58–68.

[123] A.R. Stokes. "A Numerical Fourier Analysis Method for the Correction of Widths and Shapes of Lines on X-ray Powder Photographs". In: *Proc. Phys. Soc.* 61 (1948), pp. 382–.

[124] R.A. Young and D.B. Wiles. "Profile Shape Functions in Rietveld Refinements". In: *J. Appl. Cryst.* 15.4 (1982), pp. 430–438.

[125] D. Balzar, P.W. Stephens, and H. Ledbetter. "Diffraction Line-Profile Shape by Synchrotron and Laboratory X-ray Source". In: *Advances in X-ray Analysis* 40 (1996).

[126] D. Louer and N. Audebrand. "Profile Fitting and Diffraction Line-Broadening Analysis". In: *Advances in X-ray Analysis.* 41 (1997), pp. –.

[127] D. Balzar. "Voigt Function Model in Diffraction Line-Broadening Analysis". In: *Microstructure Analysis from Diffraction*. Ed. by R.L Snyder. International Union of Crystallography, 1999.

[128] J.I. Langford. "A rapid method for analysing the breadths of diffraction and spectral lines using the Voigt function". In: *J. Appl. Cryst.* 11 (1978), pp. 10–14.

[129] J. van Berkum. "Strain Fields in Crystalline Materials; Methods of Analysis Based on X-ray Diffraction-Line Broadening". PhD thesis. Delft University, 1999.

[130] The Mfit package was written for MATLAB by D.F. McMorrow and H.M. Ronnow.

[131] J.J. Olivero and R.L. Longbothum. "Empirical Fits to the Voigt Line Width: A Brief Review". In: *J. Quant. Spectrosc. Radiat. Transfer* 17.2 (1977), pp. 233–236.

[132] W. Kraus and G. Nolze. "POWDER CELL - A Program for the Representation and Manipulation of Crystal Structures and Calculation of the Resulting X-ray Powder Patterns". In: *J. Appl. Cryst.* 29 (1996), pp. 301–303.

[133] O.J. Guentert. "X-ray Study of Pyrolytic Graphites". In: *J. Chem. Physics.* 37 (1962), p. 884.

[134] T. Hirai. "Routine Method of Crystallite Size L_a Determination of Pyrolytic Graphite". In: *J. Mater. Sci.* 4.7 (1969), pp. 644–646.

[135] R.A. Morant. "The Crystallite Size of Pyrolytic Graphite". In: *J. Phys. D. Appl. Phys.* 3.9 (1970), pp. 1367–.

[136] A.J.C. Wilson. "Tangential Contribution to Centroid Displacement and Variance of powder Diffraction Profiles". In: *J. Phys. D: Appl. Phys.* 3 (1970), pp. 1403–.

[137] S. Brunauer, P. H. Emmett, and E. Teller. "Adsorption of Gases in Multimolecular Layers". In: *J. Am. Chem. Soc.* 60.2 (1938), pp. 309–319.

[138] D. S. Greywall. "Heat capacity of multilayers of ^{3}He adsorbed on graphite at low millikelvin temperatures". In: *Phys. Rev. B* 41 (4 1990), pp. 1842–1862.

[139] Paroscientific, 4500 148th Ave., N.E. Redmond, WA, 98052, United States - http://www.paroscientific.com.

[140] T. Takaishi and Y. Sensui. "Thermal transpiration effect of hydrogen, rare gases and methane". In: *Trans. Faraday Soc.* 59 (1963), pp. 2503–2514.

[141] M. Bretz. "Ordered Helium Films on Highly Uniform Graphite- Finite-Size Effects, Critical Parameters, and the Three-State Potts Model". In: *Phys. Rev. Lett.* 38.9 (1977), pp. 501–505.

[142] R. E. Ecke, J. G. Dash, and R. D. Puff. "Effects of energy heterogeneity on phase transitions in a model monolayer system". In: *Phys. Rev. B* 26.3 (1982), p. 1288.

[143] K.D. Miner, M.H.W. Chan, and A.D. Migone. "Vapor-Pressure-Isotherm Study of N_2 on Graphite Near the Tricritical Point". In: *Phys. Rev. Lett.* 51.16 (1983), pp. 1465–1468.

[144] T.T. Chung and J.G. Dash. "N_2 Monolayers on Graphite: Specific Heat and Vapour Pressure Measurements - Thermodynamics of Size Effects and Steric Factors". In: *Surf. Sci.* 66.2 (1977), pp. 559–580.

[145] R.M. Suter, N.J. Colella, and R. Gangwar. "Location of the Tricritical Point for the Melting of Commensurate Solid Krypton on ZYX Graphite". In: *Phys. Rev. B* 31.1 (1985), pp. 627–630.

[146] M. Kruk et al. "Nitrogen Adsorption Study of Surface Properties of Graphitized Carbon Blacks". In: *Langmuir* 15.4 (1999), pp. 1435–1441.

[147] J. G. Dash and R. D. Puff. "Phase transitions in heterogeneous films". In: *Phys. Rev. B* 24.1 (1981), p. 295.

[148] B. P. Cowan. *Nuclear Magnetic Resonance and Relaxation*. Cambridge University Press, 1997.

[149] A. Abragam. *Principles of Nuclear Magnetism*. Oxford University Press, USA, 1983.

[150] F. Bloch. "Nuclear Induction". In: *Phys. Rev.* 70.7 (1946), pp. 460–475.

[151] Cryogenic Ltd. Unit 30, Acton Park Industrial Estate, The Vale, London, W3 7QE, UK - http://cryogenic.co.uk.

[152] L.E. DeLong, O.G. Symko, and J.C. Wheatley. "Continuously Operating ^{4}He Evaporation Refrigerator". In: *REv. Sci. Instr.* 147-150.1 (1971), p. 1288.

[153] Lake Shore Cryogenics, 575 McCorkle Blvd., Westerville, OH, 43082, United States - http://http://www.lakeshore.com/.

[154] High Pressure Equipment Company, P.O. Box 8248, 1222 Linden, Erie, Pennsylvania 16505, United States - http://www.highpressure.com.

[155] G. C. Straty and E. D. Adams. "Highly sensitive capacitive pressure gauge". In: *Rev. Sci. Inst.* 40 (1969), p. 1393.

[156] Andeen-Hagerling, 31200 Bainbridge Road , Cleveland, Ohio 44139-2231 U.S.A. - www.andeen-hagerling.com/ah2550a.htm.

[157] D. Hechtfischer. "Generation of homogeneous magnetic fields within closed superconductive shields". In: *Cryogenics* 27.9 (1987), pp. 503–504.

[158] Oxford Instruments, Tubney Woods, Abingdon, Oxfordshire, OX13 5QX - http://www.Oxford-instruments.com.

[159] Keithley Instruments, Ground Floor West Suite Building A, One Thames Valley, Wokingham Road, Bracknell, RG4 1NG - Http://www.Keithley.co.uk.

[160] Supercon Inc, 830 Boston Turnpike, Shrewsbury, MA 01545 United States - http://www.supercon-wire.com.

[161] D. I. Hoult and R. E. Richards. "The signal-to-noise ratio of the nuclear magnetic resonance experiment". In: *J. Magn. Reson.* 24.1 (1976), pp. 71–85.

[162] Magnicon GmbH, Lemsahler Landstr. 171, 22397 Hamburg, Germany.

[163] STAR Cryoelectronics,25-A Bisbee Court, Santa Fe, NM, 87508-1412, United States - http://www.starcryo.com.

[164] F. Arnold. "Experimental Study of Strongly Correlated Fermion Systems under Extreme Conditions: Two-dimensional ^{3}He at Ultra-Low Temperatures and Graphite in the Magnetic Ultra-Quantum Limit". PhD thesis. Royal Holloway, University of London, 2015.

[165] A. Casey et al. "Two Dimensional Ferromagnetism of a ^{3}He Film: Influence of Weak Frustration". In: *Phys. Rev. Lett* 111.3 (2013), p. 125302.

[166] A.J. Kent. "An NMR Study of Adsorbed Helium-3 Films". PhD thesis. Bedford College, 1985.

[167] K.D. Morhard, J. Bossy, and H. Godfrin. "NMR Measurements on ^3He Adsorbed on Grafoil at Submonolayer Coverages and Millikelvin Temperatures". In: *Phys. Rev. B* 51.1 (1995), pp. 446–453.